

ISSN 0377-9416



[www.pmai.in](http://www.pmai.in)

# **TRANSACTIONS OF POWDER METALLURGY ASSOCIATION OF INDIA**

**Vol. 44 No.1, June 2018**

Chief Editor - P. Ramakrishnan



ISSN 0377-9416



[www.pmai.in](http://www.pmai.in)

**TRANSACTIONS OF  
POWDER METALLURGY  
ASSOCIATION OF INDIA**

**Vol. 44 No.1, June 2018**

Chief Editor - P. Ramakrishnan



## **Powder Metallurgy Association of India**

### **Office Bearers**

#### **President**

Shri N. Gopinath

#### **Vice President**

Shri Aniket Gore

Shri Deepak Grover

Prof. Narendra Dhokey

Shri Rajendra Sethiya

#### **General Secretary**

Dr. Deep Prakash

#### **Treasurer**

Dr. Murli Gopal Krishnamoorty

#### **Joint Secretary**

Shri Sidharth Singhal

Shri Deepak Pattanayak



### Chief Editor

Prof. Ramakrishnan P.

### Editorial Advisory Board

Dr. Ashok S.

Mr. Chandrachud N.L.

Dr. Rama Mohan T. R.

### Editorial Board

Dr. Appa Rao G.

Dr. Bhargava Parag

Dr. Dabhade Vikram

Dr. Deep Prakash

Dr. Dhokey N.B.

Dr. Kumar Y.V.S.

Dr. Malobika Karanjai

Dr. Murli Gopal K.

Dr. Panigrahi B.B.

Dr. Sastry I.S.R.

Dr. Tarasankar Mahata

Published by :

### Powder Metallurgy Association of India (PMAI)

1002, B-Wing, Kingston, High Street, Hiranandani Complex, Powai, Mumbai - 4000076.

Tel. : +9122 25704588

E-mail : info@pmai.in

Neither the Powder Metallurgy Association of India nor the editor assumes responsibility of opinions expressed by the authors of the papers published in this transaction.

# Editorial



Selected papers from the successful International Conference, PM-18, held at CIDCO Exhibition centre, Navi-Mumbai are featuring in the Trans. PMAI, Vol. 44 (1), 2018. Status of PM industry in India is the lead article by President N.Gopinath. This is followed by a paper on the analysis of metal powder size and shape characterization using digital dynamic image analysis and its comparison with conventional size analysis

techniques like sieving and laser light scattering. Next paper is dealing with the O/U ratio of Uranium oxide particle size and shape distribution of resultant metal powder produced by calcio-thermic reduction, which is critical for various application of the metal powder. The best student award winning paper is an investigation correlating the the effect of configurational entropy of BCC and FCC bases high entropy alloys produced by mechanical alloying and studying their sintering behavior. Factors influencing carbon diffusion in Iron-Copper<sub>20</sub>, self lubricating bearings are dealt with in the next paper, since graphite is a solid lubricant as well as strengthens the iron rich phase. The next paper is dealing with the preliminary process prototyping trials for production scale sinter (bainite) hardening PM parts by gas quenching. The Tendolkar award winning paper is an analysis of residual thermal stresses in MoSi<sub>2</sub> based particulate composites. The processing and microstructural details of HIP+Forged and fully heat treated nickel base superalloys are discussed in the next paper. This is followed by a paper on the coating of calcium phosphate ceramics over duplex stainless steel and its characterization by scanning electron microscope coupled with spectroscopy. The next paper is on the processing of Ti<sub>29</sub>Nb<sub>13</sub>Ta<sub>4,6</sub>Zr nano crystalline alloy powders by high energy ball milling followed by sintering for biomedical applications. The study of sintering characteristics and electrical conductivity of Ytria stabilized Zirconia ceramics synthesized by co precipitation route for oxide fuel cells are dealt with in the next article. The final paper is dealing with how new ideas, processes and materials are enabling the current limited resources to a situation where by providing unlimited capabilities.

**P. Ramakrishnan**

TRANSACTIONS OF  
POWDER METALLURGY ASSOCIATION OF INDIA

Vol. 44 No.1, June 2018

CONTENTS

- |          |   |              |
|----------|---|--------------|
| <b>1</b> | <b>Status of the PM Industry in India</b><br><i>N. Gopinath</i><br><i>President, Powder Metallurgy Association of India</i>   | <b>1-3</b>   |
| <b>2</b> | <b>Particle Shape &amp; Size Characterization of Metal Powders using Digital Dynamic Image Analysis &amp; its Comparison with Conventional Size Analysis Techniques</b><br>Joerg Westermann<br>Product Manager - Retsch Technology GmbH   | <b>4-8</b>   |
| <b>3</b> | <b>Effect of O/U of Uranium Oxide on the Particle Size and Size Distribution of Resultant Uranium Metal Powder Produced by Calciothermic Reduction of its Oxide</b><br>Sonal Gupta*, Raj Kumar, Shital Thakur and S.K. Satpati<br>Uranium Extraction Division, Bhabha Atomic Research Centre, Trombay, Mumbai, India  | <b>9-14</b>  |
| <b>4</b> | <b>Effect of Configurational Entropy on Sintering Behavior of High Entropy Alloy Powders</b><br>Rahul B. Mane, Sahil Rohila and Bharat B. Panigrahi*<br>Department of Materials Science and Metallurgical Engineering, Indian Institute of Technology Hyderabad, Kandi, Sangareddy, Telangana, India  | <b>15-21</b> |
| <b>5</b> | <b>Factors Influencing Carbon Diffusion in Iron-Based Self-Lubricating Bearings</b><br>Matteo Zanon, Ilaria Rampin, Francesco Bortolotti, Alessandro Breda, Enrico Tomaello*<br>Pometon S.p.A., via Circonvallazione 62, I-30030 Maerne -Venice – Italy<br>*University of Padova, via Gradenigo, 6/a, Padova, I-35131 Italy.                                  | <b>22-27</b> |
| <b>6</b> | <b>Preliminary Process Prototyping Trails For Production Scale Sinter (Bainite) Hardening of PM Parts By Gas Quenching</b><br>N. Gopinath, V. Raghunathan<br>Fluidtherm Technology, India   | <b>28-30</b> |
| <b>7</b> | <b>Analysis of Residual Thermal Stresses in MoSi<sub>2</sub> Based Particulate Composites</b><br>Manoj Kumar Jain, Jiten Das, S Deb, J Subrahmanyam and S Ray <sup>a</sup><br>Defence Metallurgical Research Laboratory, Kanchari Bagh, Hyderabad, India<br><sup>a</sup> Visiting Distinguished Professor, Indian Institute of Technology Mandi, Mandi, India | <b>31-41</b> |
| <b>8</b> | <b>Microstructural Investigations on Hot Isostatically Processed PM Nickel Base Superalloy</b><br>B. Sreenu*, Subhradeep Chatterjee <sup>1</sup> and G. Appa Rao<br>Defence Metallurgical Research Laboratory, Kanchari Bagh, Hyderabad 500058, India<br><sup>1</sup> Dept. of Materials Science & Metallurgical Engineering, IIT, Hyderabad 502285, India    | <b>42-50</b> |

- 9 Coating of Calcium Phosphate Ceramics over Duplex Stainless Steel (S2205) and its Characterization** **51-55**  
Adhitya K, Kavitha M  
Department of Metallurgical Engineering, PSG College of Technology, Coimbatore
- 
- 10 Fabrication of Beta Ti29Nb13Ta4.6Zr Alloy through Powder Metallurgy Route for Biomedical Applications** **56-61**  
Harendra Kumar, Rajamallu K, Rameez R. Tamboli and Suhash R. Dey  
Department of Materials Science and Metallurgical Engineering, Indian Institute of Technology, Hyderabad, India
- 
- 11 A Study on Sintering Characteristics and Electrical Conductivity of Ytria Stabilized Zirconia Ceramics Synthesized by Co-Precipitation Route** **62-70**  
Amruta Vairagade, Kaustubh Kambale\*, Umesh Kedar, Sandeep Butee  
Department of Metallurgy and Materials Science, College of Engineering Pune (An Autonomous Institute of Government of Maharashtra), Wellesley Road, Shivaji Nagar, Pune - 411005
- 
- 12 Limited Resources at Unlimited Capabilities -new ideas, Processes & Materials will Allow a Good and can Provide a Brilliant Future-** **71-79**  
T. Zoz<sup>1</sup>, H. Zoz<sup>1-3</sup>  
<sup>1</sup>Zoz GmbH, D-57482 Wenden, Germany  
<sup>2</sup>CIITEC-IPN, Instituto Politecnico Nacional, Mexico City, C.P. 02250 México, D.F  
<sup>3</sup>Ritsumeikan University, Kusatsu, Shiga 525-8577, Japan
-

# STATUS OF THE PM INDUSTRY IN INDIA

N. Gopinath

President, Powder Metallurgy Association of India

## Introduction:

Powder Metallurgy Industry is directly linked to automotive industry, particularly in Indian context, as 80% of the parts produced by P/M belong to automotive parts. Therefore, it would not be wrong to state that growth of automotive industry also drives similar growth in the P/M sector.

## Automotive Industry:

Automotive industry contributes 7.1% of Indian GDP, and it is estimated that by year 2026, this contribution would grow to 12%. This would be likely due to tremendous growth estimated in vehicular production in India. Overall, auto Industry contributes ~40% of total manufacturing sector. Fig.1 shows growth in this sector, though initial slump following demonetization and stock liquidation in 2016 has been recovered. These figures are inclusive of passenger, commercial, two-wheeler and three-wheeler vehicles. Year 2013-14 witnessed sale of 2,15,00,165 units which amounted to growth of 4.13% from the last year. In consequent years, these figures were 2,33,58,047 units (8.64%), 2,40,16,068 units (2.82%), 2,53,14,460 units (5.41%) in 2014-15, 2015-16 and 2016-17, respectively. Up to Q3 of year 2017-18, the units produced were 2,14,15,719 thus projecting a 9-12% growth by the end of financial year.

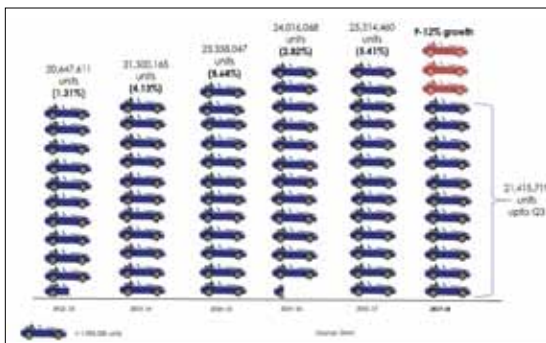


Fig.1: Automobile Production in India

On the other hand, domestic sales grew by 8.14% as compared to last year, though sector-wise distribution remained unchanged from the last year, dominated by two-wheelers (~80%), followed by passenger vehicles (~12%). Exports showed overall growth of 13%, with increase in the share of passenger vehicles (~15% from 13.9%) and three-wheelers (9.01% from 2.3%).

By the end of 2017, India became 4th largest auto market, overtaking Germany. Currently, India is counted among the top vehicle producers in the world. It is the

- Largest Tractor manufacturer
- Largest Two-wheeler manufacturer
- Largest Three-wheeler manufacturer
- 6th largest Car manufacturer
- 7th largest Commercial Vehicle manufacturer

As mentioned earlier, P/M finds directly linked to automobile sector. In this context, it is notable to view the market of sintered auto components which stands as Rs. 1006 Crore (~USD 154.8 bn), as shown in Fig.2. As expected, two-wheelers and passenger vehicles are major drivers of the demand.



Fig.2: Market of Sintered Automobile components in India



## STATUS OF THE PM INDUSTRY IN INDIA

### Emerging Opportunities for the PM Industry:

Further increase in the volume of PM industry in India can be expected due to a number of factors. One of them is growing ecological concerns and avenues to address them, such as making more fuel efficient cars as well as reducing the emissions. These require fully dense PM gears with good mechanical properties and surface finishes comparable with cut gears, which will be increasing in demand. Also, as the emission norms will be more and more strict, various components used for those purposes will be needed and hence boost the PM production. Fig.6 shows various PM components developed for BS VI emission norms.



Fig.6: New PM parts developed for BS VI

Apart from conventional automobiles, electrical/hybrid vehicles are also emerging and their share in the market is expected to increase in future. This class of vehicles, two-wheelers as well as four-wheelers also contains many parts produced by P/M. Apart from mechanical parts such as automatic gear transmission system, there is a demand for various electromagnetic controls which could be produced using P/M. Fig.7 shows some of these components to be used in electric vehicles. A fully electric vehicle requires soft magnetic sintered cores for electric motors and inverters. In addition, near net shape manufacturing of complex and compact components of electric motors, alternators and cooling system will be processed by P/M route. Despite the emerging market of electric vehicles in India, there are a set of challenges viz. high price, limited mileage, lack of charging

infrastructure, low life of batteries etc., whereas dead batteries pose environmental threat. Hopefully, difficulties put forth by these will be surmounted by technological solutions, and P/M will play a major role in it.



Fig.7: P/M parts for electric vehicles

### Summary:

There lies a huge untapped potential in various sectors such as Aerospace, Defence, Electronics and consumer goods. This includes heavy alloys such as tungsten based components. There can be applications for Metal Injection Molding (MIM) in dental, orthopedic and medical equipments. Also, Additive Manufacturing (AM) may be applied to various bio-implants. Home appliance industry has significant growth potential and PM components has a vast potential in it.

In summary, it can be said that growing automobile industry in India is expected to create opportunity for Indian PM industry. Besides conventional powders and their components, there is a vast scope to venture into newer areas such as tungsten-based materials and newer technologies such as MIM and AM.

# PARTICLE SHAPE & SIZE CHARACTERIZATION OF METAL POWDERS USING DIGITAL DYNAMIC IMAGE ANALYSIS & ITS COMPARISON WITH CONVENTIONAL SIZE ANALYSIS TECHNIQUES

Joerg Westermann

Product Manager - Retsch Technology GmbH

**Abstract** - Production capacities for specialized Metal Powders (MP) are increasing worldwide. Advances in production technologies generate a demand for tailored and tightly controlled powders with distinctive properties in terms of chemical composition, particle size distribution, and particle morphology. The size and shape of the metal particles influence process parameters as well as properties of the final products for applications such as Additive Manufacturing (AM) like Selective Laser Sintering or Electron Beam Melting processes, Metal Injection Moulding (MIM), or even solder powders. The control of the particle size distribution, as well as the particle shape, is an important step in the QC process of metal powder producers, parts manufacturers, and research facilities. A fast and comprehensive powder analysis not only allows minimizing metal powder production cost by enabling optimized process parameters, it also provides understanding of powder flowability, packing density, or surface roughness of the final parts. In this article we present analysis of metal powder size & shape characterization using modern Digital Dynamic Image Analysis & its comparison with conventional size analysis techniques like sieving & laser light scattering. The advantages and shortcomings of the different methods are demonstrated on typical metal powder samples such as steel powders, Ti64, Al, Ni, Cr and W alloys.

Traditionally, mechanical sieve analysis is the most common method for particle sizing. For metal powders, ISO 4497 and ASTM B214 describe the most relevant procedures.

Unfortunately, the smallest practically usable mesh size is 20  $\mu\text{m}$ , which is well above the average particle size of many samples for AM or MIM.

As a consequence, sieving is often used for detecting the amount of oversized particles at one sieve size only, for example 45  $\mu\text{m}$  or 63  $\mu\text{m}$ , but does not allow a fast, precise and reliable analysis of the whole size distribution.

So, especially for fine Metal powders below 100  $\mu\text{m}$  particle size, alternative methods are required. Very common is the use of a laser particle sizer (Static light scattering), as described for example in ISO 13320.

Laser Particle sizers are easy to operate and fast, however, the method is based on an indirect

measurement. The particle size is calculated from the scattering angle and light intensity of a laser light beam interacting with the sample.

Sophisticated software algorithms are employed to calculate the particle size distribution, which include assumptions and approximations to find the solution for this complex mathematical problem.

One assumption is for example that all particles are spheres. As a consequence, any deviation of the true particle shape from the theoretical spherical shape causes discrepancies in the calculated particle size distribution.

On the other hand, this simply prevents the analysis of the particle shape.

Thus the comparison of samples with different morphology may lead to surprising results, especially also when comparing different particle sizing instruments and software versions.

# PARTICLE SHAPE & SIZE CHARACTERIZATION OF METAL POWDERS USING DIGITAL DYNAMIC IMAGE ANALYSIS & ITS COMPARISON WITH CONVENTIONAL SIZE ANALYSIS TECHNIQUES

Compared to Laser light scattering, optical microscopy offers a more direct approach to particle size analysis. The basic idea is simple: "What you see is what you get". The size and morphology of particles is analysed by automatic software algorithms based on pictures of individual particles. Particle length and particle width can be measured independently, as well as parameters related to the particle shape like the aspect ratio, roundness, angularity or surface roughness.

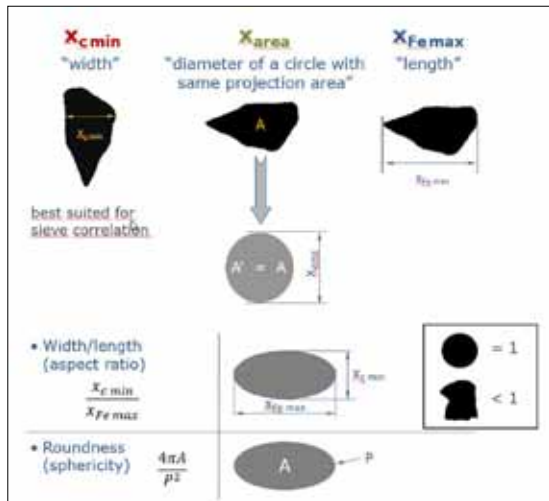


**Fig. 1 Selection of basic size and shape parameters used in image analysis.**

Two imaging methods are available, Static and Dynamic Image Analysis (SIA and DIA).

The well known SIA (=optical microscopy) analyses particles on a microscope slide. SIA is commonly used to get a qualitative impression about the shape of the particles. The insufficient dispersion of the particles on the microscope slide and the small amount of material which can be analysed prevent a quantitative analysis.

In Dynamic Image Analysis, particles in a size range from typically 1  $\mu\text{m}$  to several mm move with respect to the camera, either in a liquid cell, or as an air jet beam. This allows to analyse several millions of particles, that means a representative

amount of sample material, for example 20g, within one minute. In a simplified way, the DIA may be described as an optical microscope combined with the sample dispersion of a Laser particle sizer.

DIA allows to measure particle size distribution and quantitative particle shape (percentage of round versus irregular shaped particles, satellites, agglomerates etc.). Smallest amounts of oversized, undersized or irregular shaped particles can be detected, even below 0.01%. Thus DIA allows to gather a comprehensive overview and understanding of size and morphology related sample properties.

### Digital Dynamic Image Analysis Technique:

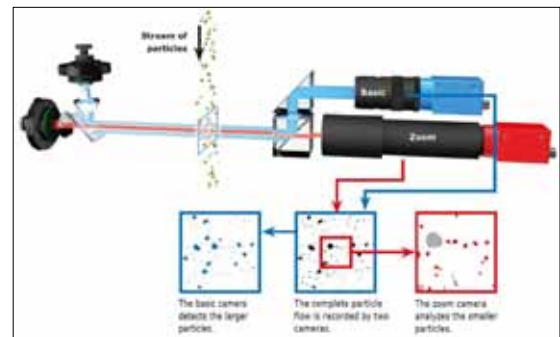


**Fig. 2 Digital Dynamic Image Analysis Technique Schematic**

The graphics shows the principal set-up of the optics for Dynamic Image Analysis. The sample moves as a particle flow through the measuring field. A light source illuminates the particles from one direction while a camera takes their picture from the opposite side. The projections of the particles are evaluated by the software to determine the size distribution of the sample in a very short time. A few hundred particles per picture are evaluated in real time. Advanced DIA systems, such as Retsch Technology's CAMSIZER X2 use two cameras with different magnifications to cover a wide measuring range: one camera with high magnification is optimized for the analysis of small particles, a second camera with a lower

# PARTICLE SHAPE & SIZE CHARACTERIZATION OF METAL POWDERS USING DIGITAL DYNAMIC IMAGE ANALYSIS & ITS COMPARISON WITH CONVENTIONAL SIZE ANALYSIS TECHNIQUES

magnification but wide field of view allows to simultaneously analyze the larger particles with high detection efficiency. The CAMSIZER X2 system records more than 300 pictures per second. Thus Dynamic Image Analysis allows for measuring statistically relevant amounts of a few million particles in a short time.

## Wide range of alloys, particle sizes and particle shapes

Fig. 3 compares results of 10 metal powder samples. Irrespective of the differences in chemistry, density, size, and shape, all samples can be analysed with one instrument setup, and the quantitative results can be visualized and understood with the help of the recorded particle images. Even for samples with average particle size of about 10  $\mu\text{m}$  a detailed shape analysis is possible thanks to recent advances in image resolution.

In this example, the Iron powder (Fe) is the coarsest, whereas the steel powder (316) is the finest. The shape diagram shows that the Ti powder is most compact, whereas the Iron powder particles are most elongated. The insert shows typical images of steel particles with different shape (satellites, elliptical droplets), and the respective calculated roundness (SPHT) and elongation (b/l).

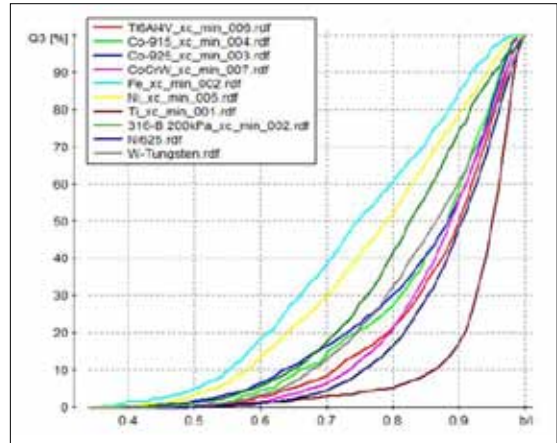
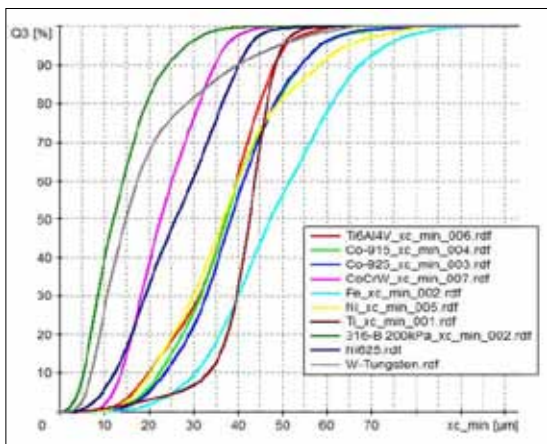
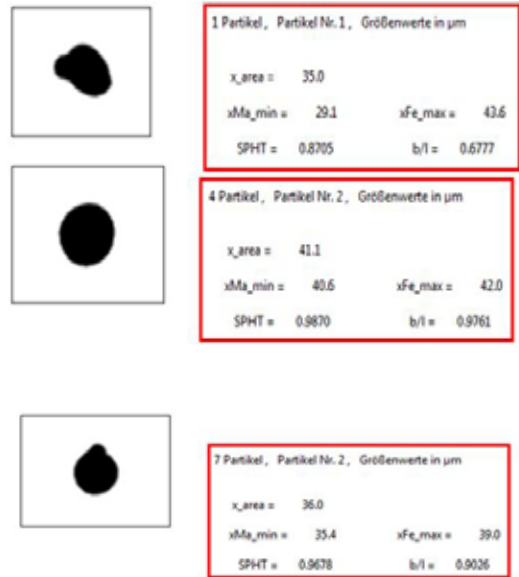


Fig. 3 Analysis of particle size and particle shape of 10 different metal powders with Dynamic Image Analysis (CAMSIZER X2). Besides the quantitative results, the recorded images allow an intuitive understanding of morphology and size differences.

## Legenden anpassen, xmin.rdf wegmachen.



# PARTICLE SHAPE & SIZE CHARACTERIZATION OF METAL POWDERS USING DIGITAL DYNAMIC IMAGE ANALYSIS & ITS COMPARISON WITH CONVENTIONAL SIZE ANALYSIS TECHNIQUES

## Comparison of laser size analysis, sieve analysis and DIA

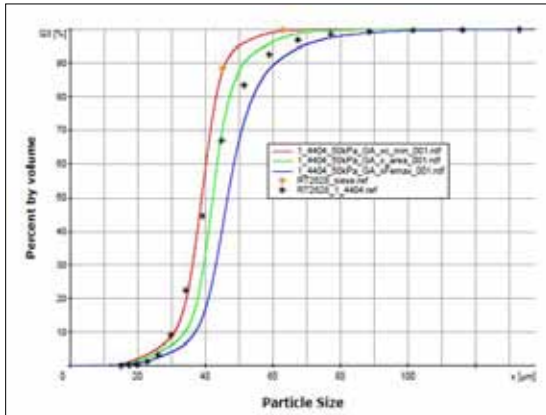


Fig. 4 Same steel powder, different size analysis methods: The results provided by sieve analysis, laser particle sizer and DIA show systematic differences.

Different analytical methods provide different size distribution curves for the same sample material. In Fig. 4 a comparison of sieve analysis, Laser particle sizer and DIA is shown for a typical steel powder with well rounded particles.

The systematic differences between the methods have been observed also for many other samples, and they become more obvious the more irregular shaped the particles are.

The results of the particle width measurement by DIA (red, CAMSIZER X2) agree perfectly with the results of the sieving (orange). DIA allows to provide exactly the same size distribution as the sieving method, thus it is possible to replace the time consuming sieving with the faster DIA, but keep the same values for product specifications etc.

The results of the laser particle sizer (black) agree well with the “width” definition of the DIA for small particles, but for large particles the agreement is better with the “particle length”. The laser particle sizer can not differentiate length and width of particles. For irregular shaped particles, the result of the measurement

includes both the length and width mixed into one graph.

Therefore, the laser particle sizer results can not match the sieve data, which are identical to the “width” measurement.

Another problem of Laser particle sizers is the detection of small amounts of outliers. Laser particle sizers are not capable of detecting small amounts (up to 2%) of oversized and undersized material reliably, as these small amounts provide not enough scattering signal. With DIA it is not only possible to detect smallest amounts of oversized particles well below 0.01%, furthermore it is also possible to take pictures of these particles and decide if these are agglomerates of several individual particles or single particles (for example elongated needles).

## Conclusion:

Several methods are available for the particle characterisation of metal powders.

The traditional methods of sieve analysis and Laser particle size analysis are nowadays replaced or complemented by Dynamic Image Analysis, which provides a more accurate and detailed sample characterisation of not only a simple size analysis but also quantitative shape analysis. This leads to a better understanding of powder properties like flowability, powder bed density and energy input required to melt the grains. Furthermore, a tighter quantitative control of QC and process parameters such as average particle size, amount of over- and undersized material and particle morphology (average roundness, percentage of satellites and other irregular shaped particles) is possible.

Besides, the analysis of the average particle size (D50), properties such as the amount of oversized material (agglomerates), undersized material (dust), and the general particle shape (roundness) are of key interest for the powder characterization. The different methods are characterized with respect to their ability to answer these questions.

## **PARTICLE SHAPE & SIZE CHARACTERIZATION OF METAL POWDERS USING DIGITAL DYNAMIC IMAGE ANALYSIS & ITS COMPARISON WITH CONVENTIONAL SIZE ANALYSIS TECHNIQUES**

---

For the analysis of most metal powders, the small particle size poses a big problem for the sieve analysis. In a conventional sieving, that means 3D sieving or tap sieving, the small particles stick in the sieve mesh and will not pass through the small holes easily, as the gravitational force is not sufficient to overcome the friction. As a result, small particles may remain on top of the sieve, although they should have passed the sieve mesh, and the sieve result becomes inaccurate.

As an alternative an air jet sieving is recommended. In the air jet sieving an airstream pushes the particles through the mesh. The disadvantage of this method is that only one particle size can be checked at a time, so it is time consuming to measure a particle size distribution consisting of several sieve sizes.

# EFFECT OF O/U OF URANIUM OXIDE ON THE PARTICLE SIZE AND SIZE DISTRIBUTION OF RESULTANT URANIUM METAL POWDER PRODUCED BY CALCIOTHERMIC REDUCTION OF ITS OXIDE

Sonal Gupta\*, Raj Kumar, Shital Thakur and S.K. Satpati

Uranium Extraction Division, Bhabha Atomic Research Centre, Trombay, Mumbai 400085, India

**Abstract** - Uranium metal powder is required for synthesis of various alloys and intermetallic compounds of uranium viz.  $UAl_3$  &  $U_3Si_2$  by powder metallurgy route; for use in dispersion type fuels. Metallothermic reduction of uranium di-oxide is one of the prominent routes for the production of uranium metal powder. In this study, uranium metal powder was prepared by metallothermic reduction of uranium di-oxide by using calcium as the reducing agent, followed by leaching with acetic acid for the removal of calcium oxide slag. Various process parameters have significant effect on the particle size and size distribution of the uranium metal powder produced, which in turn affect the recovery as well as suitability of the uranium powder for various applications; O/U ratio of uranium di-oxide is one of them. Uranium di-oxide exhibits variable O/U ratio. Literature studies have reported that increase in O/U ratio leads to a drop in the reaction initiation temperature and hence the final temperature attained, causing a decrease in the particle size. However, with higher O/U, the effect of higher enthalpy of the calciothermic reduction reaction dominates, which raises the final temperature of the reaction products, causing an increase in the particle size of the uranium powder produced. The freshly prepared uranium di-oxide gets oxidised in air with time causing the O/U ratio to increase. The aim of the investigation is to find out the exact effect of the O/U of the uranium oxide on said characteristics of the powder. Experiments of calciothermic reduction followed by leaching were done with uranium di-oxide with varying O/U ratio. The uranium powder so obtained was characterised for particle size and size distribution with laser diffraction based particle size analyser. It was observed that increase in O/U ratio of the uranium di-oxide initially caused a decrease in particle size, but with higher O/U, higher particle size was observed.

**Keywords:** dispersion fuels, powder metallurgy, calciothermic reduction, O/U ratio of oxide, particle size distribution

## Introduction

Uranium is undoubtedly the most important resource for the production and utilisation of atomic energy. Metallic uranium is by far the most suitable candidate for nuclear reactor fuel; because it has the highest breeding ratio (when compared with oxide and carbide fuels) and hence reactor doubling time [1] is the least for it. But there are certain problems that render metallic fuel unsuitable. Metallic uranium is prone to swelling, and hence clad compatibility is poor and undergoes phase change, hence lack of dimensional stability. The advantages of metallic fuel can be realised only if the metallic fuel can

be dispersed in some non-fissile matrix, which would impart structural & dimensional stability and better compatibility with the clad; because failure of one fuel particle would then not affect the integrity of the fuel. Fuel residence time in the reactor can be more than that of a conventional fuel, and lesser refueling will be needed. Ductile metal matrix also increases irradiation stability. Such dispersion fuels have become an important arena of frontier research in the field of atomic energy, especially with a view to develop highly proliferation-resistant fuels. As the enrichment was limited to less than 20% after the RERTR mandate [2] in the late 1970s, fuel (uranium)

# EFFECT OF O/U OF URANIUM OXIDE ON THE PARTICLE SIZE AND SIZE DISTRIBUTION OF RESULTANT URANIUM METAL POWDER PRODUCED BY CALCIOTHERMIC REDUCTION OF ITS OXIDE

loading had to be increased. This was done to restrict the diversion of highly enriched uranium for non-peaceful purposes. Fuel loading could be increased in two ways; one was to increase the volume fraction of the fuel meat, which is limited to 55 vol%, as per the plate fuel geometry. The other method is to increase the uranium loading in the fuel itself, by using high uranium density alloys like  $UAl_3$  &  $U_3Si_2$  as dispersoids in the fuel. These fuels are being used in some high flux research and test reactors [3-5].

One of the starting materials for the synthesis of these dispersoids by powder metallurgy [6-8] is uranium powder, which has been manufactured by various routes like atomization, hydride-dehydride (HDH) process, mechanical grinding. Atomization [9, 10] is the most common technique to produce metal/alloy powders, but it is highly energy-intensive because the metal has to be brought to molten state in the first place. Moreover, control over particle size is difficult. HDH [11] process involves converting metal to its hydride, which is brittle and turns into powder on dehydriding due to the volume change occurring during hydriding. It yields very fine powders; which poses handling issues for uranium powder due to its pyrophoricity. All of the three methods involve more number of processing steps and require bulk metal (of which the powder is desired) in the first place.

Metallothermic reduction of oxides can also be used to produce some metals in powder form [12]. If the heat generated during the reaction is sufficient to raise the temperatures of both the slag and the metal to values beyond their melting points and if they remain molten for a sufficient length of time, slag – metal separation occurs due to density difference ending up in bulk metal. When the heat of the reaction is insufficient to result in an all-liquid reaction mixture, other forms of the metal are obtained. If the reaction occurs but the slag does not melt, the metal is formed as a powder dispersed in a slag matrix [12]. In this case, the slag is leached away to separate the metal powder. Uranium powder

can be produced by metallothermic reduction of uranium dioxide, because the heat of reaction is sufficient to melt uranium (melting point 1132°C) but not the calcium oxide slag (melting point 2572°C). This method yields uranium directly in powder form, and hence lesser number of process steps are involved compared to the aforementioned processes; and forms the line of study in this paper. Uranium oxide exhibits variable O/U ratio, it is because of the different oxidation states of uranium metal, the most important are +4 and +6, hexavalent being the most stable oxidation state of uranium. Hence, freshly prepared uranium di-oxide easily gets oxidised

in air with time causing the O/U ratio to increase. In this study, metallothermic reduction of uranium dioxide samples of varying O/U ratio was carried out using calcium as the reductant, followed by leaching of the calcium oxide slag with acetic acid to recover uranium in powder form and the effect of O/U of oxide on the particle size of final powder was studied.

## Experiment

Samples of uranium dioxide ( $UO_{2+x}$ ) with varying O/U ratio were taken for the analysis, and their calciothermic reduction (CTR) was carried out, followed by leaching (to recover metallic values), drying and packing. O/U ratio analysis was done at Quality Control Section (QCS Lab), UED, BARC. O/U ratio was determined by gravimetric method, where  $UO_2$  sample was converted into stable uranium oxide  $U_3O_8$  at 800°C and uranium content in the sample was calculated. Tap density was determined as per ASTM B-527, 1976.

**Table 1: Input  $UO_2$  characteristics**

Sr. No. / Batch no.	$UO_2$ Characteristics		
	O/U	Tap density (in g/cc)	Mean Particle Size (in $\mu m$ )
N_ $UO_2$ _I	2.08	2.78	16.36
N_ $UO_2$ _II	2.18	2.78	16.36
N_ $UO_2$ _III	2.63	2.78	16.36

## EFFECT OF O/U OF URANIUM OXIDE ON THE PARTICLE SIZE AND SIZE DISTRIBUTION OF RESULTANT URANIUM METAL POWDER PRODUCED BY CALCIOTHERMIC REDUCTION OF ITS OXIDE

Fig. 1 shows schematic of the experimental setup for calciothermic reduction. 50 g  $\text{UO}_2$  sample was taken and mixed thoroughly with reductant Ca. This charge was fed into a yttria-lined graphite crucible. The remaining crucible space was capped with pre-calcined CaO. CaO was chosen as capping material, as it is one of the by-products of the reaction itself, so that there is no contamination from other material. The crucible was put into a retort which had three connections, one for the K type thermocouple (Chromel-Alumel), one for argon inlet and other for argon outlet. This retort was introduced into a resistive type pit furnace. The chamber was evacuated and back flushed with argon three times and thereafter argon was purged continuously to maintain an inert atmosphere. The charge was heated up to  $1200^\circ\text{C}$  in a pre defined heating schedule. After a sufficient amount of preheating, the heat content of the charge is sufficient to fire the exothermic reaction and make it self-sustaining:  $\text{UO}_2 + 4\text{Ca} \rightarrow \text{U} + 2\text{CaO} + 2\text{Ca}$ . The set value of furnace temperature was fixed at  $1200^\circ\text{C}$ . The charge was soaked at temperature of  $1200^\circ\text{C}$  for one hour. The furnace temperature and crucible temperature were monitored. This external heating is done to minimise the loss of reaction heat as well as to maintain the uranium in molten form for sufficient time for coalescence of particles to form bigger particles.

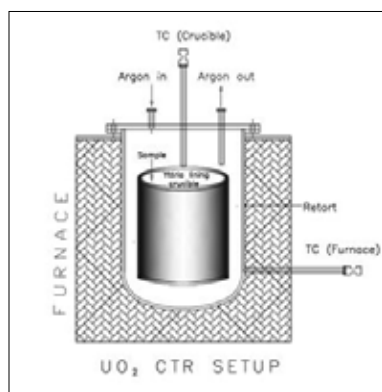


*Fig. 1: Schematic of the experimental setup for calciothermic reduction.*

The reduced mass obtained after CTR was subjected to leaching with 6N acetic acid in an agitated glass beaker. As the reaction  $\text{CaO} + 2\text{CH}_3\text{COOH} \rightarrow (\text{CH}_3\text{COO})_2\text{Ca} + \text{H}_2\text{O}$  is highly exothermic, cooling of the beaker was done. During leaching, temperature must be maintained between  $20^\circ\text{C}$  and  $30^\circ\text{C}$ ; since below  $20^\circ\text{C}$ , leaching rate is too low, and above  $30^\circ\text{C}$  losses of uranium by solubilisation may increase. Uranium does not get dissolved and collects at bottom as a grey precipitate; CaO and excess Ca get leached away by acetic acid. The U precipitate was contacted with acetic acid; with intermittent settling and decantation; this was done to remove all the CaO from uranium. The precipitate was washed with acetone and vacuum dried, whereby it finally turned into a silvery grey U powder. Drying, packing and sealing were carried out under inert atmosphere inside glove box as U powder is pyrophoric. The presence of even a very small amount of air/oxygen can cause violent reaction of U and oxygen causing the powder to catch fire. After packing and sealing, particle size analysis of U powders by laser diffraction method was done with CILAS Particle Size Analyser 1090.

### Thermodynamic calculations.

Though the reaction  $\text{UO}_2 + 2\text{Ca} \rightarrow \text{U} + 2\text{CaO}$  is exothermic in nature, however the amount of energy released is not sufficient to cause the temperature of the products to rise above the melting point of uranium. We need uranium to be in the molten state, so that the droplets of uranium covered by solid calcium oxide will give rise to spherical powder particles of uranium, which is of interest for the present study. Through previous experience and literature, we can assume that a preheating of charge up to about  $500 - 650^\circ\text{C}$  will provide the necessary heat to fire the reaction and provide sufficient heat input for melting the reduced uranium. Also, we use 100% excess of the reductant Ca to ensure complete reduction of  $\text{UO}_2$  to uranium metal.



# EFFECT OF O/U OF URANIUM OXIDE ON THE PARTICLE SIZE AND SIZE DISTRIBUTION OF RESULTANT URANIUM METAL POWDER PRODUCED BY CALCIOTHERMIC REDUCTION OF ITS OXIDE

This temperature is decided by the combined effect of the reaction initiation temperature and the heat of reaction. Increase in the O/U of the oxide causes the reaction initiation temperature to decrease [13], however it has also been reported that it causes the increase in the enthalpy of the reaction (more heat is liberated) [12,13].

In the case of O/U 2.18, the effect of decrease in the reaction initiation temperature is more dominant, which causes particle size to decrease. The presence of  $\text{UO}_3 / \text{U}_3\text{O}_8$  in the case of O/U 2.63 causes the effect of enthalpy to be more dominant, which causes particle size to increase again. However, the mean particle size 11.56  $\mu\text{m}$  obtained in the case of O/U 2.63 is still less than that obtained in the case of O/U 2.08.

$\text{UO}_2 + 2\text{Ca} == \text{U} + 2\text{CaO}; \Delta H_{298}^\circ = -44.2 \text{ kcal/g. atom U};$   
 $\text{UO}_3 + 3\text{Ca} == \text{U} + 3\text{CaO}; \Delta H_{298}^\circ = -163.5 \text{ kcal/g. atom U}$  [13]

## Conclusions:

1. As O/U increases from 2.08 to 2.18, the initiation temperature and the reaction temperature drops down which causes the particle size of the final U powder to decrease from 21.47  $\mu\text{m}$  to 6.68  $\mu\text{m}$ . This has been mentioned above that due to presence of higher oxides, reaction temperature drops down, as has been already reported in literature [13].
2. However, at much higher O/U ratio of 2.63, the effect of higher enthalpy of reaction with oxides like  $\text{UO}_3$  dominates over the previous stated effect of higher oxides, and causes temperature to increase and hence particle size of final powder again increases to 11.56  $\mu\text{m}$ , but this increase is still less than the first case of O/U of 2.08.
3. The temperature increase causes coarsening of particles and hence larger particle size.

## Acknowledgements

The authors are thankful to Shri Pramendra Singh, Shri U.B. Naik and all other staff of the Specific

Metal Production Section of Uranium Extraction Division (UED) for their extended support in carrying out the calciothermic reduction and leaching experiments. The authors also thank Shri K.N. Hareendhran and Shri S.V. Kadam of Quality Control Section, UED in carrying out the O/U ratio and tap density analysis of uranium oxide samples; and particle size analysis of uranium oxide and uranium metal powders.

## References

1. Harvey L. Wyckoff, Paul Grebler, "Definitions of Breeding Ratio and Doubling Time", *Nucl. Tech.*, **21** (3), 158-164, (1974).
2. A. Travelli, "The U.S. Reduced Enrichment Research and Test Reactor (RERTR) program", *Proceedings of the 1978 International Meeting on REDUCED ENRICHMENT FOR RESEARCH AND TEST REACTORS*, Argonne, Illinois, November 9-10, 3-18, (1978).
3. D.D. Keiser, Jr., S.L. Hayes, M.K. Meyer, and C.R. Clark, "High-Density, Low-Enriched Uranium Fuel for Nuclear Research Reactors", *JOM*, **55** (9), (2003).
4. R. F. Domagala, T. C. Wiencek and H. R. Thresh, "U-Si and U-Si-Ai Dispersion Fuel Alloy Development for Research and Test Reactors", *Nucl. Tech.*, **62** (3), 353-360, (1983).
5. S. Van Den Berghe, P. Lemoine, "Review of 15 years of high-density low-enriched U-Mo dispersion fuel development for Research Reactors in Europe", *Nucl. Engg. Tech.*, **46** (2), 125-146, (2014).
6. W.D. Wilkinson, "Uranium Metallurgy", vol. 1, pp. 397-410, (Interscience Publishers, John Wiley & Sons, 1962).
7. J. Greenspan and T.R. Wright, "Powder Metallurgy Processing of Uranium Alloys," in "Physical Metallurgy of Uranium Alloys", Proceedings of the Third Army Materials Technology Conference, J.J. Burke et. al. (Eds), 83-108, (1974).
8. ASM Handbook, vol. 7, "Powder Metal Technologies and Applications", (ASM International, 1998).
9. A. Lawley, "Atomization: The production of Metal Powders", (MPIF, 1992)
10. J.T. Strauss, "Development of Uranium Atomization Process by the Use of a Surrogate Metal," *HJE Corporation Report*, (1998)

**EFFECT OF O/U OF URANIUM OXIDE ON THE PARTICLE SIZE  
AND SIZE DISTRIBUTION OF RESULTANT URANIUM METAL POWDER  
PRODUCED BY CALCIO THERMIC REDUCTION OF ITS OXIDE**

---

11. W.M. Mueller, J.P. Blackledge and G.G. Libowitz (Eds.), *"Metal Hydrides,"* (Academic Press, 1968).
12. Chiranjib K. Gupta, *"Chemical Metallurgy,"* pp. 383-384, (Wiley-VCH Verlag GmbH & Co. KGaA, Weinheim, 2003).
13. N.P. Galkin, B.N. Sudarikov; *"Technology of Uranium,"* pp. 374-382, (Israel Program for Scientific Translations Ltd., 1966).
14. David R. Gaskell, *"Introduction to the Thermodynamics of Materials,"* pp.130-149, (Taylor & Francis, 3rd Ed., 2002).
15. O. Kubaschewski and C.B. Alcock, *"Metallurgical Thermochemistry,"* pp. 267-360, (Pergamon Press, 5th Ed., 1979).

# EFFECT OF CONFIGURATIONAL ENTROPY ON SINTERING BEHAVIOR OF HIGH ENTROPY ALLOY POWDERS

Rahul B. Mane, Sahil Rohila and Bharat B. Panigrahi\*

Department of Materials Science and Metallurgical Engineering, Indian Institute of Technology Hyderabad, Kandi, Sangareddy, 502285, Telangana, India

**Abstract** - Powder metallurgy is one of the major routes for producing high entropy alloys; however, several fundamental issues yet to be fully understood, including sintering mechanisms and entropy effects etc. Present investigation correlates the effect of configurational entropy of alloys on their sintering behaviors. The different sets of mechanically alloyed powders were considered; where one set was FCC based alloys such as CoFeNi, CoCuNi, CoCrFeNi and CoCrFeNiMn alloys, and another set was BCC based alloys, such as TiCrFeNi, AlCoCrFeNi, AlCoCrFeNiMn and AlCoCrFeNiSi alloys. Dilatometric sintering reveals, shrinkage was found to be decreased with increasing alloying number. The estimated activation energies of sintering (non-isothermal sintering kinetics) indicate, increasing values with increasing alloying order, suggesting sluggish diffusion behavior. It was also noticed that activation energies of BCC phase based powders were relatively smaller than FCC phase based powders. This initial level of investigation clearly indicates, sintering of HEA powders are influenced significantly by the configurational entropy of the system.

## Introduction

The ability to form simple solid solution with excellent properties is reason for growing interest in HEA alloys [1-3]. While defining these alloys, four core effects have been believed to affect the alloy behavior, which are: high entropy, sluggish diffusion, severe lattice distortion and cocktail effect [1, 4]. Factors such as diffusion behavior and entropy are of particular interest in the present context. When numbers of elements are more in concentrated solid solution, diffusion becomes slow, because cooperative diffusion of different kinds of atoms is difficult [5, 13-16]. In very recent study on Ni tracer diffusivity in CoCrFeNi and CoCrFeNiMn HEAs, suggested that increase in number of elements, may not be the only reason for slow diffusion [16].

The configuration entropy of the alloy increases with increasing alloying components, which leads to the major disorderness in the system [1, 5-12]. The entropy has different contributions such as configurational, vibrational, magnetic dipole and electronic randomness [1-5]. The configurational entropy ( $\Delta S_{\text{conf}}$ ) usually

dominates over the others; which depends on the number of constituting elements of the alloy. Boltzmann's modified equation [17] has been used to estimate the  $\Delta S_{\text{conf}}$  as shown below:

$$\Delta S_{\text{conf}} = -R \sum_{i=1}^n X_i \times \ln X_i \quad (1)$$

Where, R is gas constant, 8.314 J/K/mol.  $X_i$  is mole fraction and n is number of element. The calculated  $\Delta S_{\text{conf}}$  for equiatomic alloys have been shown in Table 1.

*Table 1. The configurational entropies in term of R for equi-atomic alloys with elements up to 8*

Number of elements	1	2	3	4	5	6	7	8
$\Delta S_{\text{conf}}$	0	0.69	1.10	1.39	1.61	1.79	1.95	2.08

The increased entropy plays major role in formation of solid solution and microstructures. The effect of alloying components on microstructure evolution was observed during annealing of the rolled specimen; for example, the recrystallization temperature was found to be increased from 700°C (for CoFeNi alloy), to about 800°C (for CoCrFeNi alloy) and 900°C (for CoCrFeMnNi alloy) [18].

# EFFECT OF CONFIGURATIONAL ENTROPY ON SINTERING BEHAVIOR OF HIGH ENTROPY ALLOY POWDERS

It is fairly accepted that number of alloying elements dictates both diffusivity as well as configurational entropy. But whether the diffusivity can be affected by the entropy or not, is still an issue for investigation or debate. It is interesting to recall, much before the concept of high entropy alloy came into existence, the effect of entropy on diffusion behavior was already proposed in some materials by Adam and Gibbs [19] in 1965, and followed by others [20-22]. It was proposed that diffusion coefficient can decrease with increasing configurational entropy [19-22]. The relation between diffusivity ( $D$ ) and configurational entropy ( $\Delta S_{conf}$ ) was proposed by Adam and Gibbs, as:

$$D = D_0 \exp\left(-\frac{C}{T\Delta S_{conf}}\right) \quad (2)$$

where,  $D$  is diffusion coefficient,  $D_0$  is Frequency factor,  $C$  is constant, and  $T$  is Temperature. Further Rosenfeld derived expression [22] to explain relation between diffusion constant and entropy (3), as:

$$D = a \exp\left(\frac{bS_{ex}}{K_B}\right) \quad (3)$$

Where,  $S_{ex}$  is excess entropy (which is total entropy - Ideal gas entropy),  $a$  and  $b$  are empirical fitting parameters, and  $K_B$  is Boltzmann's constant.

Since the packing of atoms become more complicated in the high entropy alloys, it results in unequal atomic distances with different bond energies; as a result, particularly diffusion paths become more complex and sluggish [1-3, 13-14]. These factors now raise a new question, which is particularly relevant for high entropy alloys; that is, if the diffusion behavior changes with increasing alloying order or configurational entropy, the diffusion dependent processes, such as the sintering behavior of the alloy powder is also affected or not. However, there is hardly any study on sintering mechanisms of high entropy alloy powders, except few articles from the same authors [23-24]. While continuing the exploration, present investigation aims to focus on some of these fundamental sciences behind

the sintering of high entropy alloy powders:

- i) The effect of configurational entropy on non-isothermal sintering kinetics has been studied.
- ii) Efforts have also been made to see, whether the sintering kinetics, are dependent on crystal structure of the alloy or not; i.e. a comparative study on FCC (face centered cubic) based alloys versus BCC (body centered cubic) based alloys have also been carried out.

In the present study, alloying orders have been varied from 3 elements to 6 elements, to obtain alloys with different configurational entropies. Alloys were further grouped in two categories: FCC phase based and BCC phase based.

## Materials and methods

Elemental powders (-325 mesh) of Co, Fe, Ni, Cr, Mn, Cu, Si, Ti and Al of about 99.5% purity were mixed in an equimolar ratio for respective CoFeNi, CoCuNi, CoFeNiCr, TiCrFeNi, CoFeNiCrMn, AlCoCrFeNi, AlCoFeNiCrMn and AlCoCrFeNiMnSi alloys. These alloys have been designated as 3F1, 3F2, 4F1, 4B2, 5F1, 5B2, 6B1 and 6B2 respectively (where notation letter F refers to FCC phase or F-series and letter B refers to BCC phase or B-series). Powder mixtures were milled on a planetary ball mill (Fritsch P-5) using WC balls and vials with toluene media, for about 15 h at a speed of about 300 rpm; where ball to powder weight ratio was about 15:1. As-milled powders were characterized through Differential scanning calorimetry (Netzsch DSC 404 F<sub>3</sub>) to determine the melting point ( $T_m$ ) and phase conversion and stability. Small cylindrical pellets (with a relative green density of about 60%) of about 7 mm diameter were prepared at a uniaxial pressure of about 70 MPa for all powders. Green compacts were sintered non-isothermally, on a vertical dilatometer system (Theta Inc. USA) to record dimensional changes. Pellets were heated at a rate of about 10 °C/min up to about 1150 °C under purified Ar. Before feeding into the sample chamber, argon gas was passed

## EFFECT OF CONFIGURATIONAL ENTROPY ON SINTERING BEHAVIOR OF HIGH ENTROPY ALLOY POWDERS

through the heated titanium chips (heated at about 800 °C) to remove the traces of oxygen and moistures. Samples were characterized using X-ray diffraction (XRD, X'Pert PRO, PANalytical, with Cu  $\alpha$  radiation of wavelength 1.5405Å), scanning electron microscope (FESEM Supra 40, Carl-Zeiss) and transmission electron microscope (JEOL JEM 2100FX TEM).

### Result and Discussion

#### Phases and microstructural analysis

The XRD pattern of as-milled powders has been shown in Fig.1 (FCC systems) and Fig.2 (BCC systems). The peaks belong to mostly FCC phase could be seen on 3F1, 3F2, 4F1 and 5F1 alloys (Fig.1). The 3F2 alloy showed two FCC phase and it was confirmed with reported literature data [24]. The along with major FCC phase several small peaks were observed, which may be attributed to sigma phase and some meta-stable phases.

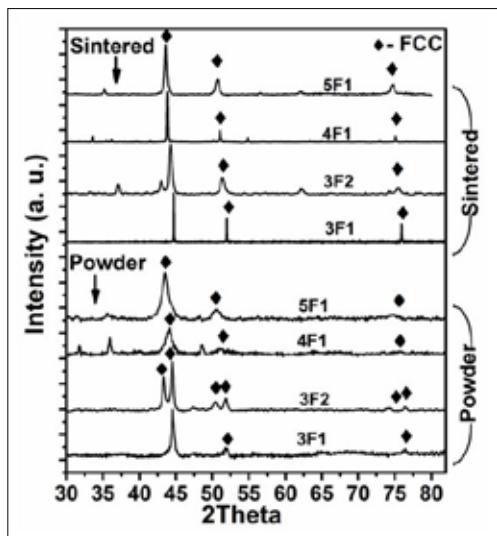


Fig. 1: XRD patterns of FCC based powders and sintered samples.

In the Fig.2, BCC phase could be seen as major phase on 4B2, 5B2, 6B1 and 6B2 powders. The 5B2, 6B1 and 6B2 systems also showed

few unidentified peaks which could be FCC, intermediate phase or sigma phase. One interesting thing was noticed that in Al based HEAs (5B2, 6B1 and 6B2), FCC was present as secondary phase. Addition of aluminum leads to dual phase alloy (as reported earlier also).

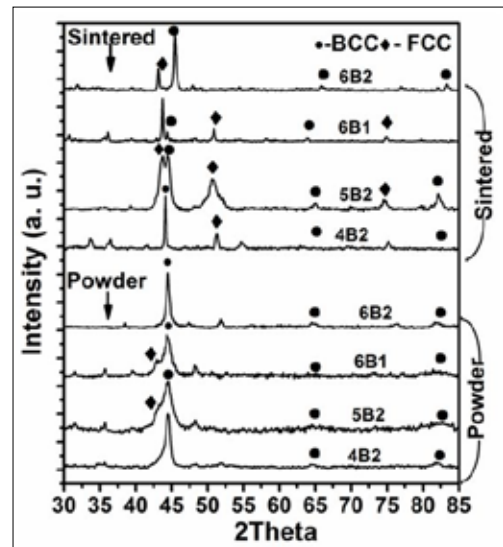
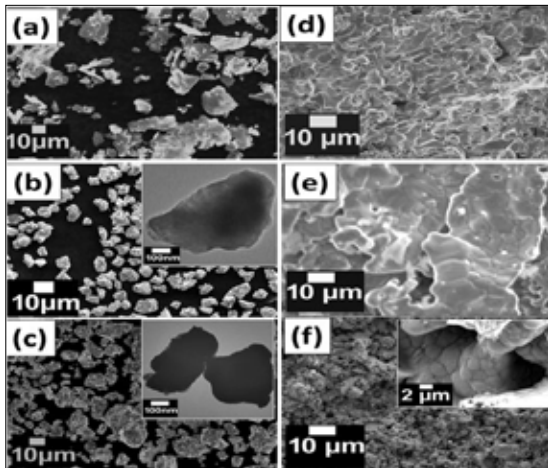


Fig. 2: XRD patterns of BCC based powders and sintered samples.

XRD patterns for sintered samples have also been shown in Fig. 1 (FCC alloys) and Fig. 2 (BCC alloys). Peaks on sintered samples were found to become sharper, as-compared to respective powder samples, which could be attributed to the release of internal strains and defects concentrations, increased chemical homogeneity and stabilization of phases at elevated temperatures, etc. FCC phase as emerged as a major phase after sintering in all F-series powders, whereas it was all duplex phases (BCC + FCC) in B-series powders, except AlCoCrFeNiMn alloy, which shows FCC as major phase. Peaks correspond to un-identified phases or meta-stable phases (in as-milled powders) were almost vanished during sintering in all the samples. The transformation of BCC to FCC and BCC phase after sintering was further confirmed with literature data [23-26].

## EFFECT OF CONFIGURATIONAL ENTROPY ON SINTERING BEHAVIOR OF HIGH ENTROPY ALLOY POWDERS

SEM micrographs of the milled powders as well as fractographs of corresponding sintered samples have been shown in Fig. 3 and Fig. 4 for F-series and B-series samples. Powders were found to be mostly in agglomerated forms, typically in the range of 10 to 15 microns. The TEM imaging of some of the powders reveals (Fig. 3 insets), the individual particles were typically sub-micron size (below 300 nm mostly). They were highly irregular in shape and varied sizes. The SEM micrographs of the sintered samples (Fig. 3 and 4), shows variation in the grain size with increasing alloying number. It could be clearly seen that grain size is much larger for 4 element alloys (Fig. 3e) compared to 5 element alloy (Fig. 3f). A high resolution image of one of the sintered sample (Fig. 3f inset) shows, fully recrystallized grains which are smaller than 2 microns, have formed large agglomerates. Similarly grain size was found to be decreased in B-series samples also with increasing alloying order (Fig. 4 (d, e, and f)). By looking at the microstructure one can easily make out that amounts of porosity in the sintered bodies, have gradually increased with increasing alloying elements in both type of alloys.



*Fig. 3: SEM micrographs of FCC alloys: a) 3F1, b) 4F1, c) 5F1 powders. Insets in Fig. (b) and (c) show the corresponding TEM images, where particles are in nanometric range. SEM micrographs of the fractured surface of respective sintered samples have been shown*

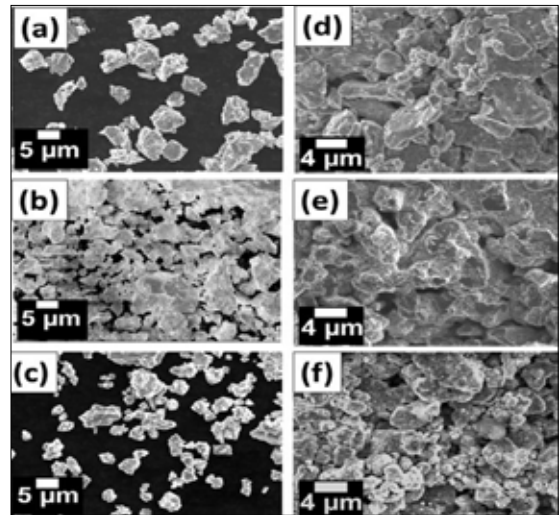


*Fig. 4: SEM micrographs of BCC alloys: a) 4B2, b) 5B2, c) 6B1 powders and SEM micrographs of the fractured surface of respective sintered samples have been shown in d), e), and f).*

### Sintering kinetics

Dimensional changes recorded during heating of green compacts as a function of homologous temperature ( $T/T_m$ ; where  $T$  is sintering temperature and  $T_m$  is the melting temperature of respective alloy) have been shown in Fig. 5a (FCC alloys) & Fig. 6b (BCC alloys). Melting points of the alloys were determined separately through differential scanning calorimetry. Dilatometer plots show different regions:

- i) sample expanded almost linearly during initial heating due to the thermal property of the material.
- ii) After an initial period, expansion was interrupted with little shrinkages in the temperature range of about  $0.3$  to  $0.5 T_m$ ; which could be attributed to particle rearrangements driven by the releases of residual strains and dislocations, and chemical homogenization as indicated through XRD patterns. Particle rotations, grain sliding and rearrangement had been proposed earlier [27-28] and observed in some other fine powders during early stage sintering [28-29].

## EFFECT OF CONFIGURATIONAL ENTROPY ON SINTERING BEHAVIOR OF HIGH ENTROPY ALLOY POWDERS

iii) After the transient shrinkage period, sample tends to expand again, which followed by a gradual shrinkage, which was continued until the set temperature.

Dilatometer curves of samples 3F1 and 3F2 were found to exhibit drastic change in the sample dimension, compared to other alloys (Fig. 5). Amount of dimensional change was found to be decreased gradually with increasing number of elements, in both F-series as well as B-series samples.

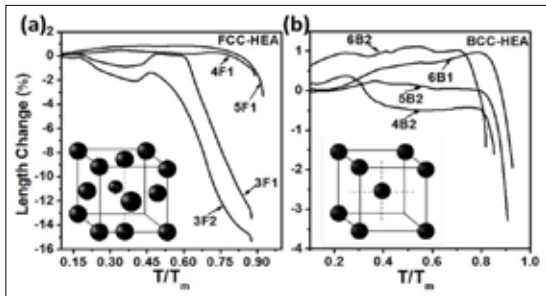


**Fig. 5:** Recorded Dilatometer plots during non-isothermal sintering of: a) FCC alloy powders and b) BCC alloy powders.

Actual shrinkage data from as-received dilatometric plots were extracted through usual method; which have been plotted in Fig. 6 (a and b), as a function of homologous temperature. It was found that the ternary CoFeNi and CoCuNi alloys showed very high axial shrinkage during heating. Shrinkage was found to be drastically decreased when alloying numbers have increased to 4 to 6. The 3F1 and 3F2 alloys showed high relative density (82% and 89% respectively), compared to 6B1 and 6B2 alloys (72% and 75% respectively).

There are various driving forces for sintering, such as diffusion mechanisms, chemical inhomogeneity, metastable phases, dislocations etc.; however, diffusion based mechanisms such as grain boundary diffusion (GBD) and/or volume diffusion (VD) processes often controls the densification in early stage. Hence the axial shrinkage data further analyzed using well known diffusion based nonisothermal sintering model [30].

$$\ln[T^p (dY/dT)] = \ln C - Q/[(n+1)RT] \quad (4)$$

Where, Y is  $\Delta L/L_0$ ,  $L_0$  is the initial length of the green compact,  $\Delta L$  is the change in length, T is the temperature, R is the universal gas constant, C is a constant depending on material parameters, n and P are constants. P has the value of 3/2 for VD and 5/3 for GBD, and the values of n are 1 and 2 for VD and GBD respectively [30]. Activation energies of sintering were estimated through the Arrhenius plots produced using Eq. (1), for both VD and GBD mechanisms, as shown in Fig. 6 (c to f). Further, in-order to correlated the activation energies of sintering with configurational entropies of the alloys, the calculated activation energies were plotted as a function of  $\Delta S_{conf}$  as shown in Fig. 7 (a and b) for GBD and VD mechanisms respectively. It could be clearly seen that activation energies of sintering gradually increased with increasing  $\Delta S_{conf}$  irrespective of whichever mechanism is considered. On the same figures (Fig. 7), it is interesting to see that for a given number of alloying elements, FCC phase based alloy powders show relatively larger activation energies compared to that of BCC phase based alloy powders. At the current level of study, this differential kinetics could be attributed to the more open structure of BCC phase compared to FCC lattice.

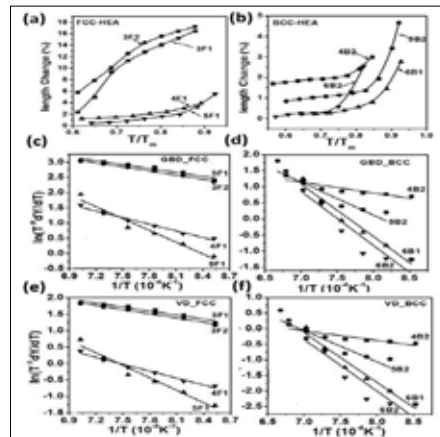


**Fig.6:** Measured axial shrinkages of homologous temperature, for: a) FCC alloys and b) BCC alloys. Arrhenius plots using Eq. (4) to estimate activation energies of sintering for GBD: c) FCC alloys and d) BCC alloys; and for VD: e) FCC alloys and f) BCC alloys.

# EFFECT OF CONFIGURATIONAL ENTROPY ON SINTERING BEHAVIOR OF HIGH ENTROPY ALLOY POWDERS

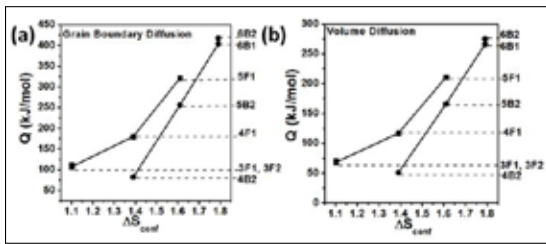


Fig. 7: Variation of activation energies as a function of configurational entropy, for both FCC and BCC alloys: a) grain boundary diffusion and b) volume diffusion mechanisms.

It should be noted that, it is difficult to obtain fully (100%) single phase alloy powder through mechanical alloying. Product often contains certain amount of impurity phases also; which was true in the current work too; which may affect the sintering behavior of the powders to some extent. In spite of these facts, the trend observed in the current results are worth considering and to look way forward. Further availability of very high purity powders and diffusivity data on HEAs in future, may help to have better understanding of the issue. This investigation also opens up many challenges, to be explored further.

## Conclusions

This work successfully demonstrates the dependence of sintering kinetics on configuration entropies of the multi-component high entropy alloy powders. Process was characterized with increasing activation energies, with increasing alloying order. It was also indicated that different crystal structures of solid solution alloys, exhibit different sintering kinetics. In the present case, FCC based alloy powders shows larger activation energies compared to BCC based alloy powders for the identical alloys (having same number of alloying elements).

## References

1. J. W. Yeh, S. K. Chen, S. J. Lin, J. Y. Gan, T. S. Chin, T. T. Shun, S. Y. Chang, "Nanostructured high-entropy alloys with multiple principal elements: novel alloy design concepts and outcome", *Adv. Eng. Mater.*, **6**, 299-303, (2004).

2. D. B. Miracle, O. N. Senkov, "A critical review of high entropy alloys and related concepts", *Acta Mater.* **122**, 448-511, (2017).
3. S. Ranganathan, "Alloyed pleasures: multimetallic cocktails", *Current science*, **85** (5), 1404-1406, (2003).
4. C. Y. Cheng, Y. C. Yang, Y. Z. Zhong, Y. Y. Chen, T. Hsu, J. W. Yeh, "Physical metallurgy of concentrated solid solutions from low-entropy to high-entropy alloys", *Curr. Opin. Solid State Mater. Sci.*, **21**, 299-311, (2017).
5. B. Gludovatz, A. Hohenwarter, D. Catoor, E. H. Chang, E. P. George, R. O. Ritchie, "A fracture-resistant high-entropy alloy for cryogenic applications", *Science*, **6201**, 1153-1158, (2014).
6. Y. Lu, Y. Dong, S. Guo, L. Jiang, H. Kang, T. Wang, B. Wen, Z. Wang, J. Jie, Z. Cao, H. Ruan, T. Li, "A promising new class of high-temperature alloys: eutectic high entropy alloys", *Sci. Rep.*, **4**, 1-56200, (2014).
7. Y. Zhang, T. Zuo, Y. Cheng, P.K. Liaw, High-entropy alloys with high saturation magnetization, electrical resistivity, and malleability, *Sci. Rep.*, **3** (2013).
8. N. Stepanov, M. Tikhonovsky, N. Yurchenko, D. Zybakin, M. Klimova, S. Zherebtsov, A. Efimov, G. Salishchev, "Effect of cryo-deformation on structure and properties of CoCrFeNiMn high-entropy alloy", *Intermetallics*, **59**, 8-17, (2015).
9. K. V. Thurston, B. Gludovatz, A. Hohenwarter, G. Laplanche, E.P. George, R.O. Ritchie, "Effect of temperature on the fatigue-crack growth behavior of the high-entropy alloy CrMnFeCoNi", *Intermetallics*, **88**, 65-72, (2017).
10. W. Huo, F. Fang, H. Zhou, Z. Xie, J. Shang, J. Jiang, "Remarkable strength of CoCrFeNi high-entropy alloy wires at cryogenic and elevated temperatures", *Script. Mater.*, **141**, 125-128, (2017).
11. P. Li, A. Wang, C. T. Liu, "A ductile high entropy alloy with attractive magnetic properties", *J. Alloys Compd.*, **694**, 55-60, (2017).
12. F. Tian, L. K. Varga, N. Chen, J. Shen, L. Vitos, "Empirical design of single phase high-entropy alloys with high hardness", *Intermetallics*, **58**, 1-6, (2015).
13. K.Y. Tsai, M. H. Tsai, J. W. Yeh, "Sluggish diffusion in CoCrFeMnNi high entropy alloys", *Acta Mater.*, **61**, 4887-4897, (2013).

## EFFECT OF CONFIGURATIONAL ENTROPY ON SINTERING BEHAVIOR OF HIGH ENTROPY ALLOY POWDERS

14. M. Vaidya, S. Trubel, B. S. Murty, G. Wilde, S. V. Divinski, "Ni tracer diffusion in CoCrFeNi CoCrFeMnNi high entropy alloys", *J. Alloys Compd.*, **688**, 994-1001, (2016).
15. D. L. Beke, G. Erdélyi, "On the diffusion in high-entropy alloys", *Mater. Lett.*, **164**, 111-113, (2016).
16. M. Vaidya, K. G. Pradeep, B. S. Murty, G. Wilde, S. V. Divinski, "Radioactive isotopes reveal a non-sluggish kinetics of grain boundary diffusion in high entropy alloys". *Sci. Rep.*, **7**(1), 12293, (2017).
17. B. S. Murty, J. W. Yeh, S. Ranganathan, "High-entropy alloys", (Butterworth-Heinemann, 2014).
18. B. R. Chen, A. C. Yeh, J. W. Yeh, "Effect of one-step recrystallization on the grain boundary evolution of CoCrFeMnNi high entropy alloy and its subsystems", *Sci. Rep.*, **6**, 22306, (2016).
19. G. Adam, J. H. Gibbs, "On the temperature dependence of cooperative relaxation properties in glass-forming liquids", *J. Chem. Phys.*, **43**, 139-146, (1965).
20. A. Scala, F. W. Starr, E. La. Nave, F. Sciortino, H. E. Stanley, "Configurational entropy and diffusivity of supercooled water", *Nature*, **406**, 166-169, (2000).
21. N. Giovambattista, S. V. Buldyrev, F. W. Starr, H. E. Stanley, "Connection between Adam-Gibbs theory and spatially heterogeneous dynamics", *Phys. Rev. Lett.*, **90**, 085506, (2003).
22. K. Seki, B. Bagchi, "Relationship between entropy and diffusion: A statistical mechanical derivation of Rosenfeld expression for a rugged energy landscape", *J. Chem. Phys.*, **143**, 194110, (2015).
23. R. B. Mane, B. B. Panigrahi, "Effect of alloying order on non-isothermal sintering kinetics of mechanically alloyed high entropy alloy powders". *Mater. Lett.*, **217C**, 131-134, (2018).
24. R. B. Mane, Rajkumar Y., B. B. Panigrahi, "Sintering mechanisms of CoCrFeNiMn high entropy alloy powders". *Powder Metallurgy* (2018). Doi:10.1080/00325899.2018.1433268.
25. S. Varalakshmi, M. Kamaraj, B. S. Murty, "Formation and stability of equiatomic and nonequiatomic nanocrystalline CuNiCoZnAlTi high-entropy alloys by mechanical alloying". *Met. Mater. Trans.A*, **41**(10), 2703-2709, (2010).
26. S. Praveen, B. S. Murty, R. S. Kottada, "Phase evolution and densification behavior of nanocrystalline multicomponent high entropy alloys during spark plasma sintering", *JOM*, **65**(12), 1797-1804, (2013).
27. L. Ding, R. L. Davidchack, J. Pan, "A molecular dynamics study of sintering between nanoparticles", *Comp. Mater. Sci.*, **45**, 247-256, (2009).
28. J. S. Lee, L. Klinger, E. Rabkin, "Particle rearrangement during sintering of heterogeneous powder mixtures: a combined experimental and theoretical study", *Acta Mater.*, **60**, 123-130, (2012).
29. B. B. Panigrahi, M. M. Godkhindi, K. Das, P. G. Mukunda, V. V. Dabhade, P. Ramakrishnan, "Sintering mechanisms of attrition milled titanium nano-powder", *J. Mater Res.*, **20**, 827-836, (2005).
30. J. Han, A. M. R. Senos, P. Q. Mantas, "Nonisothermal sintering of Mn doped ZnO", *J. Eur. Ceram. Soc.*, **19**, 1003-1006, (1999).

# FACTORS INFLUENCING CARBON DIFFUSION IN IRON-BASED SELF-LUBRICATING BEARINGS

Matteo Zanon, Ilaria Rampin, Francesco Bortolotti, Alessandro Breda, Enrico Tomaello\*

Pometon S.p.A., via Circonvallazione 62, I-30030 Maerne -Venice - Italy

\*University of Padova, via Gradenigo, 6/a, Padova, I-35131 Italy.

**Abstract** - Sintered self-lubricating bearings are a classic example of how the porosity of sintered components, normally considered one of their greatest weaknesses, can become a key functional requirement. Typically these products are based on sintered CuSn10 bronze alloys with graphite additions, but for less demanding applications iron-copper combinations are also well established materials. Graphite additions are required to act both as solid lubricant as well as to strengthen the iron-rich phase. The two requirements are clearly contrasting with each other, being opposite functions of the degree of carbon diffusion.

The present work tries to systematically investigate the influence of base Fe-Cu20 powder, sintering conditions and natural graphite granulometry on the dimensional and mechanical properties in both green and sintered state. Both existing and newly developed PM solutions are examined. A characterization of flow, compaction, dimensional, mechanical and microstructural behavior is given. Guidelines for an integrated material-graphite-process selection are finally presented.

## Introduction

Porous sintered self-lubricating bearings are a staple product of PM industry, with wide applications in the electrical motors of home appliances and other electric machines [1]. These components are mass-produced by cold pressing, sintering, sizing and oil impregnation; most performing material is bronze CuSn10, which guarantees the widest functioning range in terms of load-velocity combination (so called "Pv value"), but iron-copper and iron-bronze materials are also well established lower cost alternatives [2]. The simplest example of a plain bearing is a hole with a shaft rotating inside it; when the shaft starts turning, direct contact between the two surfaces causes attrition and wear. As the shaft gathers speed, hydrodynamic lubrication sets in, as oil is drawn by capillary action towards the bearing-shaft interface. [1]. The main oil reservoir is the bearing's porosity, which is typically around 15-25 %. This relatively high level of voids poses a stringent requirement on green strength of the pressed powder; being green density a fixed parameter, typically around 5,80 - 6,20 g/cm<sup>3</sup>, the particles must establish the highest possible number of contact

points in order to confer mechanical strength to the pressed component. This can be achieved by using irregular particles, which for iron-based materials typically means sponge iron. In previous works [3] the opportunity for water-atomized grades was illustrated.

Graphite additions are widely employed as solid lubricant for the initial dry friction phase. But while carbon has practically no solubility in copper, it dissolves easily in iron, with well known hardening and strengthening effects. This means that less free graphite will remain available for lubrication, and a higher wear on sizing dies. Carbon diffusion rate can be altered by choosing graphite type and granulometry, which in turn will interact with sintering conditions and also base material.

In this work, a full characterization of the filling, compaction, mechanical and microstructural properties of sintered bearings is given, produced using newly developed water atomized iron-based premixes as well as sponge-based materials and standard water atomized iron powders. Three different natural graphite granulometries were tried. Composition and green density were kept fixed, and correspond to widely

# FACTORS INFLUENCING CARBON DIFFUSION IN IRON-BASED SELF-LUBRICATING BEARINGS

used material DIN B 22. Two different sintering temperatures were tested, with fixed sintering time, to study the response to process conditions and in particular to the carbon diffusion rate. The complex interactions among base powder, graphite granulometry and processing conditions are presented and discussed. Guidelines for overall material – process optimization are finally given.

## Experimental

Nine different iron-based premixes were prepared in the laboratory using three different types of industrially produced iron powders. For one set, a sponge iron powder “Sponge I” was used; the other two sets are based on water atomized iron powders, newly developed grade “WA 1” [3] and standard “Fersint”. Copper was introduced into iron powder under homogeneous diffusion bonding conditions, in proportion of 20 w%. After milling, three different natural graphites were admixed to each base iron powder, 1,80 w%. Fine, medium-coarse and coarse grades with respective  $D_{90} = 25 - 90 - 150 \mu\text{m}$  were used. Powders were subsequently admixed and homogenized for 15 minutes in a Y-shaped rotating mixer, with 0,80 w% amide wax as lubricant. Apparent density and flow time were measured on Hall flowmeter with 2,5 mm hole (ISO 3923/1 and ISO 4490). For the evaluation of green properties, TRS bars 30x12x6 mm were compacted at a constant pressure of 600 MPa and subsequently broken on 3-points bending test (ISO 3995). Bushes with nominal 20 mm external and 15 mm internal diameters, 10 mm height were compacted at  $6,00 \pm 0,01 \text{ g/cm}^3$  density and crushed by applying a force along radial direction. Radial crushing strength is then calculated by applying the following formula (ISO 2739):

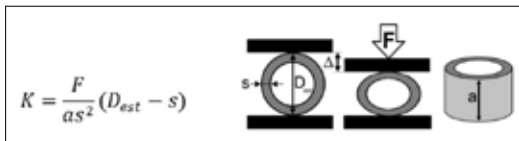


Fig. 1 - Calculation of green ( $K_v$ ) and sinter ( $K_s$ ) radial crushing strength

For sintering tests, bushes with 14 mm external and 9 mm internal diameter diameters, 10 mm height were compacted at a constant green density of  $6,00 \text{ g/cm}^3$ . Sintering was performed in a laboratory belt furnace at a temperature of  $880 / 1020 \text{ }^\circ\text{C}$  for 8 minutes, under a  $80\text{N}_2\text{-}20\text{H}_2$  atmosphere and normal cooling conditions (cooling rate around  $1,0 \text{ }^\circ\text{C/s}$  calculated between  $650$  and  $315 \text{ }^\circ\text{C}$ ). After sintering operations, dimensional change (D.C.) was calculated as percentage variation of final sintered external diameter with respect to die diameter; radial sintered crushing strength was evaluated through the formula described in Figure 1, while radial deformation “ $\Delta\%$ ” was taken as percentage ratio of radial deformation  $\Delta r$  to  $D_{\text{est}}$ . This parameter gives an indication of the maximum deformation that can be imposed during sizing; a higher value is desirable since it means that the material can accommodate larger radial deformation without failure. Metallographic cuts were examined, and Vickers micro-hardness with 25 g load was measured on iron particles.

## Results and discussion

Table I presents the results on the packing and green properties on each premix. Sponge I and WA 1 are all very close to each other, while Fersint, as expected, has the highest apparent density and slightly improved flow rate.  $25 \mu\text{m}$  graphite renders the mixes not free flowing, while coarser grades markedly improve this important processing property. This is related to both lower intrinsic flowability of fine powders and to their higher surface area, which creates a more widespread rheological interaction with base material.

Table I - Packing and green properties of experimental premixes FeCu20 + 1,80% graphite + 0,80% wax.

	Graphite	Packing properties		TRS bars @ 600 MPa		Bushes @ $6,00 \text{ g/cm}^3$	
		D90 [ $\mu\text{m}$ ]	Flow [s/50g]	App. Dens. [ $\text{g/cm}^3$ ]	Compressibility [ $\text{g/cm}^3$ ]	TRS [MPa]	Kv [MPa]
Sponge I	25	-	2,46	6,82	18,4	14,0	
	90	38,0	2,47	6,81	20,1	14,6	
	150	35,5	2,38	6,83	21,1	15,6	
WA 1	25	-	2,49	6,90	19,3	11,4	
	90	39,0	2,51	6,88	20,8	11,8	
	150	34,0	2,45	6,90	21,4	13,5	
Fersint	25	-	2,86	7,05	12,3	4,4	
	90	36,5	2,86	7,03	13,3	4,5	
	150	32,0	2,79	7,04	13,6	5,7	

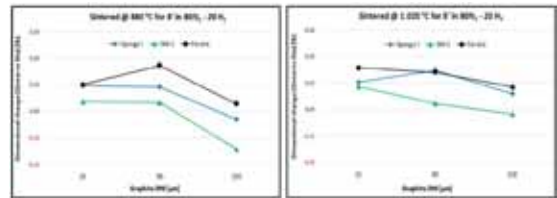
## FACTORS INFLUENCING CARBON DIFFUSION IN IRON-BASED SELF-LUBRICATING BEARINGS

Moving now to green properties, we see that water atomized powders as a group are more compressible than sponge counterparts. Highest value is attained by Fersint, followed by WA1. Graphite granulometry has hardly noticeable effects. Green strength at constant pressure is definitely lower for Fersint with respect to other products, which all feature similar values. Coarser graphites are slightly beneficial, by interposing on less iron particle contacts. In the production of bearings, Kv is a critical parameter, being green density fixed during pressing operation, typically around 5,80 - 6,20 g/cm<sup>3</sup>. A minimum value is required in order to be able to handle the compacts between pressing and sintering operations. There is no generally valid minimum value, which depends on wall thickness, component dimensions and manipulation process; from industrial practice, it seems that a minimum of 3 MPa is required to provide acceptable consistency. Sponge I gives highest values, followed by WA 1; Fersint performs rather poorly. Graphite effect is more evident for this green strength measure, especially for water atomized powders; the coarsest graphite grants a 30 % improvement over the finest one on Fersint-based premix. On sponge iron, the effect is only around 11 %.

Coming now to sintering results, charts will be presented showing properties against graphite type, for each base iron powder.

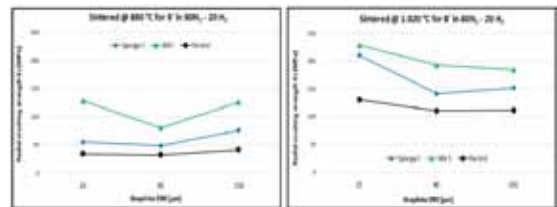
Dimensional change results depend first of all on base powder, with WA 1 always showing the least growth - or even shrinkage-. As documented in [4], the dimensional behavior in this temperature range is determined by the degree of carbon diffusion in austenite phase. The introduced lattice distortion causes an expansion, which is retained after cooling and more than compensates the natural tendency to densification driven by surface area reduction. Finer graphite granulometry favours deeper carbon diffusion, and it is generally related to higher growth. The 25  $\mu\text{m}$  and 90  $\mu\text{m}$  grades are not very dissimilar, while a noticeable effect

is observed with the 150  $\mu\text{m}$  at 880 °C. Higher temperature enhances both carbon diffusion but also surface free energy reduction (i.e. shrinkage), and its net effect is on average very small, around 0,05 % only. This means that these materials are dimensionally very stable against temperature fluctuations. The graphite effect is "smoothed out", with less variation especially when comparing the 150  $\mu\text{m}$  grade to the other two.



*Dimensional change against graphite granulometry for each iron powder. Left hand - Fig. 2: after sintering at 880 °C; right hand - Fig. 3: after sintering at 1.020 °C*

The mechanical properties are displayed in Fig. 4 and 5. Radial crushing strength, as measured by  $K_s$  factor, is maximum for WA 1, reaching an increase of 60 - 130 % against sponge I after 880 °C sintering. At higher sintering temperature, all mechanical properties increase substantially, benefitting from both stronger particles neck formation and microstructural strengthening due to carbon dissolution.



*Radial crushing strength factor  $K_s$  against graphite granulometry for each iron powder. Left hand - Fig. 4: after sintering at 880 °C; right hand - Fig. 5: after sintering at 1.020 °C*

Graphite particle size effect follows a complex pattern, depending on both sintering temperature and base powder. While at 880 °C a coarser size favours  $K_s$ , up to 40% for Sponge I, the reverse is

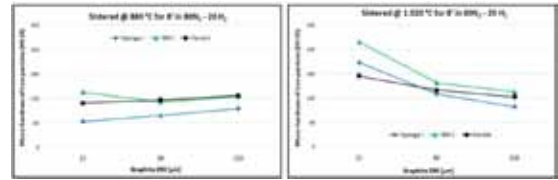
## FACTORS INFLUENCING CARBON DIFFUSION IN IRON-BASED SELF-LUBRICATING BEARINGS

true at 1.020 °C, up to -30% for Sponge I as well. The combination 90 µm graphite - 880 °C looks relatively unfavourable, especially for WA1; the trend was confirmed by other experiments, but it is of difficult explanation. Water atomized powders are less sensitive to graphite type in this respect.

Radial deformation at fracture “Δ%” follows a trend very similar to Ks, rising from an average of 1,4 % to 2,1 % going from lower to higher sintering temperature. WA1 enjoys the highest values, while Fersint falls last. This means that the new WA materials generally display higher strength and lower brittleness, which must be related to a higher sintering degree as reflected by lower dimensional change with respect to sponge-based ones.

A deeper understating of the observed macroscopic behavior can be acquired by considering micro-hardness measurements together with metallographic cuts. Comparing Fig. 6 with Fig. 7, it’s clear how higher sintering temperature translates into overall higher hardness, although the rate of increase is strongly related to graphite particle size. The finest grade shows an average increase of around 110 HV, the intermediate of 40 HV and the coarsest remains practically constant. This suggests that 150 µm grade is so little reactive that its diffusion into iron does not change much over this temperature range. At 880°C, low hardness variation is observed with graphite, with a surprising slight increase for coarse particles; at 1.020°, a much stronger variation takes place, with finest graphite yielding highest hardness, as expected by its enhanced diffusivity into iron. It is thought that, being atomic carbon diffusion into austenite still relatively slow at 880°C [4], the graphite particle size is not an important limiting factor. The hardness increase could be due to higher sintering degree, which is pointed out by lower expansion/shrinkage with coarser graphite. At 1.020°C instead, graphite particle size becomes important, and carbon dissolution the key hardness driver. Water atomized powders

turn out generally harder than sponge powder, especially at lower sintering temperature.



*Micro hardness measurements against graphite granulometry for each iron powder. Left hand - Fig. 6: after sintering at 880 °C; right hand - Fig. 7: after sintering at 1.020 °C*

These observations can be confirmed by looking at microstructures. Fig. 8 - 9 show the results after low temperature sintering (880°C) for 8 minutes, for the finest and coarsest graphites. Each material features the same ferritic microstructure, interspersed by copper, with no significative difference whatsoever. Some pearlite traces can be seen for WA1 and also Fersint, which account for the slightly higher hardness observed. Sponge iron particles show their characteristic internal porosity, which is also present on the WA 1 material, although with a somewhat different distribution. For Fersint almost only full particles are present.



*Fig. 8 - Microstructures after 880 °C sintering, with 25 µm graphite (Nital etched, 400X). 8.1 - Sponge I, 25 µm graphite; 8.2 - WA1, 25 µm graphite; 8.3 - Fersint, 25 µm graphite*

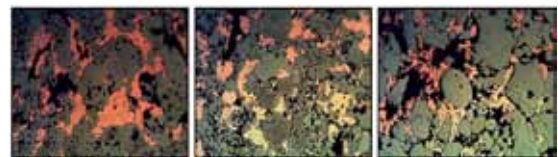


*Fig. 9 - Microstructures after 880 °C sintering, with 150 µm graphite (Nital etched, 400X). 9.1 - Sponge I, 150 µm graphite; 9.2 - WA1, 150 µm graphite; 9.3 - Fersint, 150 µm graphite*

## FACTORS INFLUENCING CARBON DIFFUSION IN IRON-BASED SELF-LUBRICATING BEARINGS

Going to higher sintering temperature, the differentiation among the graphites becomes much more pronounced. At 1020°C, carbon diffusion can take place much more actively, with higher hardness and ferritic/pearlitic microstructures as consequences. With 25 µm graphite extensive pearlite formation can be appreciated in all materials, especially in WA1. Ferrite instead largely prevails with 150 µm grade, confirming that carbon diffusion is greatly limited when using such a coarse source. Once again, WA1 presents the highest pearlite content and hardness. Sponge I looks instead almost 100% ferritic, with no change in hardness with respect to equivalent 880 °C sintering.



*Fig. 10 - Microstructures after 1.020 °C sintering, with 25 µm graphite (Nital etched, 400X). 10.1 - Sponge I, 25 µm graphite ; 10.2 - WA1, 25 µm graphite; 10.3 - Fersint, 25 µm graphite*

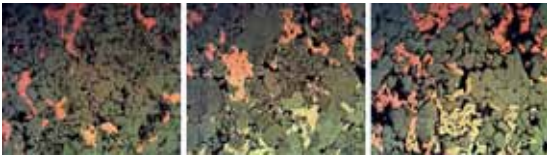


*Fig. 11 - Microstructures after 1.020 °C sintering, with 150 µm graphite (Nital etched, 400X). 11.1 - Sponge I, 25 µm graphite ; 11.2 - WA1, 25 µm graphite; 11.3 - Fersint, 25 µm graphite*

On average, a systematic  $\approx 40$  HV increment is reported for WA1 in comparison to sponge I. Also Fersint is generally harder, although with one exception. The reasons for this behaviour are not totally clear: it is thought anyhow that differences in the amount of silicon, an impurity typically present in sponge powder (around 0,60% in this case) and almost absent ( $<0,05\%$ ) in water atomized, could be the main factor. Silicon is well-known to substantially raise the chemical potential of carbon [5], thus reducing its gradient

and slowing its diffusion, and to suppress cementite formation [6,7]. Other considerations on physical properties lack consistency when overall experimentation is considered [3].

Figures 12-13 plot radial crushing strength  $K_s$  against iron particles hardness, for the two sintering conditions, with a line connecting the values referring to same material. From these charts it is possible to estimate the contribution to mechanical properties of iron particle shape, carbon diffusion and neck formation.  $K_s$ -HV slopes are in any case positive, giving a measure of carbon strengthening effect. Sintering temperature increase confers to each material around +100 MPa at fixed micro-hardness level, thanks to more extensive inter-particle connections. This is the single most important effect in numerical terms. At both temperatures, one can notice that the low apparent density materials (Sponge I, WA1) are positioned at a higher strength level than Fersint, for the same level of hardness. In other words, for sponge and special grade WA1, hardness can explain more or less their difference in  $K_s$ , while standard WA Fersint is less resistant at same hardness level. It has been already suggested [3] that low apparent density materials enjoy a higher number of inter-particle contacts already after pressing, and these become further consolidated during sintering. At these relatively low holding temperatures, that do not allow an extensive consolidation, the "starting condition" is expected to be influential. The more rounded shape of Fersint then would account for a  $K_s$  difference around -50 MPa with respect to a low density iron powder with the same hardness.

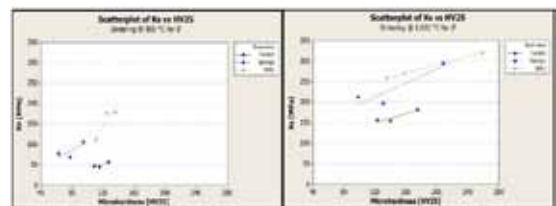


*Chart of  $K_s$  against iron micro-hardness  $K_v$  for the different materials. Left hand: Fig. 12 - Sintering at 880°C. Right hand: Fig. 13 - Sintering at 1.020°C.*

# FACTORS INFLUENCING CARBON DIFFUSION IN IRON-BASED SELF-LUBRICATING BEARINGS

## Conclusions

The filling, green and sintering properties of both water atomized and sponge iron-based Fe-Cu premixes for porous bearings were analysed, together with their interaction with graphite particle size.

- For optimal filling characteristics, coarser graphite is to be preferred; even if apparent density is marginally higher, free-flowing behaviour cannot be achieved when 25  $\mu\text{m}$  graphite grade is admixed. This already explains why coarser grades are typically preferred for such mixes. It is notable how special water atomized-based WA1 can give an apparent density very close to sponge.
- Water atomized grades offer better compressibility, especially if one is willing to sacrifice some green strength in exchange for it. Graphite influence is in this case moderate or negligible
- Sintering operations, performed at two temperatures, showed a rather complex, temperature-dependent relationship with graphite granulometry. A coarser graphite will lead to less growth, especially at 880°C, with better dimensional precision. At this sintering temperature it also yields better mechanical properties, while at 1.020°C a finer graphite improves carbon dissolution and thus strength. New WA1 enjoy a dimensional change close to 0%, the highest observed radial crushing strength  $K_s$  and deformation at failure  $\Delta\%$ .
- Micro-hardness and microstructure analysis highlighted substantially different rates of carbon diffusion, according to base iron, graphite granulometry and sintering temperature. While at low temperature the graphite particle size is of little significance, at higher temperature it controls the depth of carbon diffusion and thus final hardness.
- Different amounts of pearlite were observed, with highest amount for WA1 grade and lowest for Sponge I. Different amounts of

chemical impurities, in particular silicon, were proposed to be the main reason behind these differences. In practical terms, this means that, if hardness is to be minimized in order to favour sizing operation, a coarser graphite and/or a lower sintering temperature are to be considered, especially with WA1. If a very coarse graphite is already being used, these changes are not effective.

A special thanks goes to Dr. R. Gilardi of Imerys for having provided the graphite powder samples.

## References

- [1] W. Pahl, "Boccole sinterizzate", AIM course on non ferrous sintered metals, Milan (I) 15/04/2008
- [2] N. A. Arnold, "P/M Bearings", ASM Handbook Vol. 7 1992, pp. 705-6
- [3] M. Zanon & others, "Iron-base solutions for bearings", World PM 2016 Hamburg, conference proc.
- [4] K. P. Jonnalagadda, "Influence of graphite type on copper diffusion in Fe-Cu-C alloys", MSc degree thesis, 2012
- [5] L. S. Darken (Trans. AIME, Vol. 180 (1949), pp. 430-438
- [6] H. K. D. H. Bhadeshia, "Case study: design of bainitic steels", 2000 <http://www.msm.cam.ac.uk/phase-trans/2000/C9/C9-8.pdf>
- [7] C. Shade & T. Murphy, "Microstructure and mechanical properties of PM steels with Silicon and Vanadium", MPIF Congress Nashville 2012 proc.

# PRELIMINARY PROCESS PROTOTYPING TRAILS FOR PRODUCTION SCALE SINTER (BAINITE) HARDENING OF PM PARTS BY GAS QUENCHING

N. Gopinath, V. Raghunathan

Fluidtherm Technology, India

**Abstract** - The microstructure of sintered PM parts are generally ferrite and pearlite where the pearlite content varies with the carbon content. Other than by a separate heat treatment process PM parts can also hardened by sinter hardening in a mesh belt sintering furnace within a module placed immediately after the furnace. The furnace atmosphere is re-circulated across heat exchangers & blasted on parts as they emerge from the sintering furnace. Generally high alloy compositions are required to obtain a predominantly martensitic structure with some bainite being allowed depending on the alloy & application.

Fully bainitic microstructure is conventionally obtained in a process called austempering where steel & ductile iron parts are austenised & quenched in a salt bath generally maintained between 280°C to 400°C depending on the required hardness, the carbon & alloy content & section thickness. The parts are held for the desired transformation time required for full bainitic transformation. This 'austempering' process is practiced for improving the toughness & fatigue strength of processed parts whether wrought or sintered.

Other researchers<sup>(1,2)</sup> have published their work on methods of obtaining a bainitic microstructure in PM parts by suitable alloying & cooling rate control and resulting properties obtained. However there are very few references on the results of conventional austempering which includes isothermal holding. It was decided to build an (open to public) process prototyping furnace to perform the conventional processes of sintering ( $T_{max}=1150^{\circ}\text{C}$  in  $\text{N}_2+\text{H}_2$ ) followed by rapid gas cooling (like in sinter hardening but with hot gas) followed by isothermal holding between 250°C to 500°C. The purpose was to study the response of a variety of PM alloys and production parts.

As a first trial gears made in Astalloy CRM + 0.5%C & Astalloy Mo + 0.6%C were processed and the results are reported in this paper.

**Keywords:** Bainite Hardening, Gas quenching, Sinter hardening, PM Austempering

## Experimental Methods:

We started with a study the CCT diagram of CRM alloy (courtesy Hognas AB) with a view to determine viable process parameters, implement these in our prototype furnace & study the different types of bainite obtained. Fig. 1 shows the CCT curve of CRM alloy & on this the we have superimposed the desired cooling curve.

## Experimental Setup:

A roller hearth furnace with a hot gas quench module was constructed for the study. The furnace concept and the required sintering & cooling profile are shown in Fig.2).

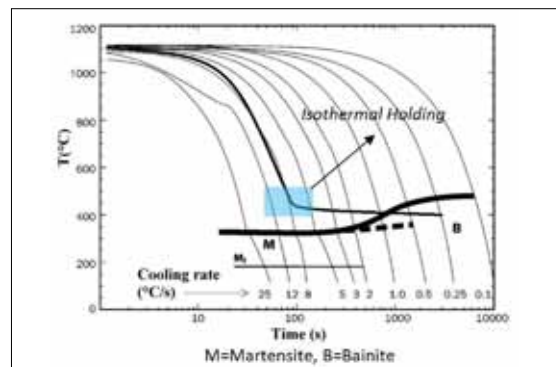
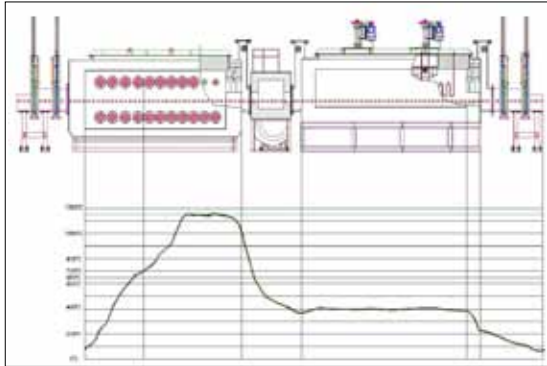


Fig.1 CCT Diagram for Astalloy CRM

# PRELIMINARY PROCESS PROTOTYPING TRAILS FOR PRODUCTION SCALE SINTER (BAINITE) HARDENING OF PM PARTS BY GAS QUENCHING



*Fig.2 Roller hearth Furnace with Thermal Profile*

The parts are transported through all parts of the furnace on metal & ceramic rollers in several groups with individual drives as well as chain conveyors. After the debinding & sintering sections appears a hot gas quench module and then a convection furnace for isothermal holding. Atmosphere lock doors are provided at both ends & between different sections to maintain control over the atmosphere composition.

First trials were performed in an atmosphere of 90%N<sub>2</sub>+ 10%H<sub>2</sub>. The test parts were loaded on a tray made from a furnace mesh belt (Fig.3) and sinter soaked at 1120°C for 25minutes and then moved rapidly to the hot gas quench chamber. The cooling rate was measured by a single trailing thermocouple. The quench gas temperature was maintained between 350°C to 470°C with varying re-circulation fan speeds (Fig. 4).



*Fig.3 Part Loaded on a Mesh Belt Tray*

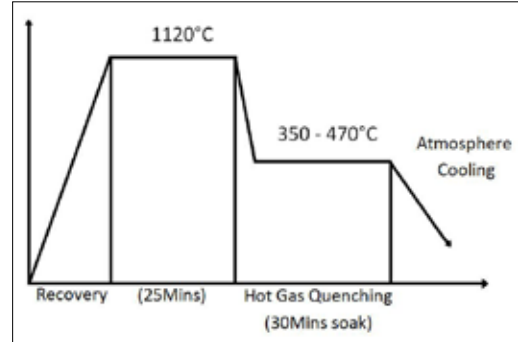


*Fig.4: Trial Process Cycle*

## Results:

1. The measured temperature profile & cooling rate is superimposed on the ASTALLOY CRM CCT curve are shown in Fig.5.

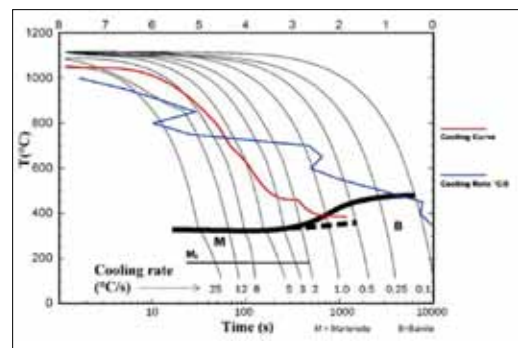


*Fig.5*

2. Microphotograph:



*Fig.6 Astalloy CRM Microstructure shows lower bainite with some ferrite and without any trace of martensite. Hardness: 350HV 0.5*

## PRELIMINARY PROCESS PROTOTYPING TRAILS FOR PRODUCTION SCALE SINTER (BAINITE) HARDENING OF PM PARTS BY GAS QUENCHING

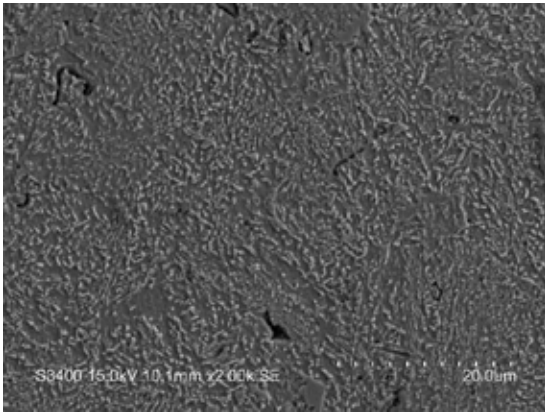


*Fig.7 Astalloy CRM SEM Micrograph shows predominantly bainitic structure.*

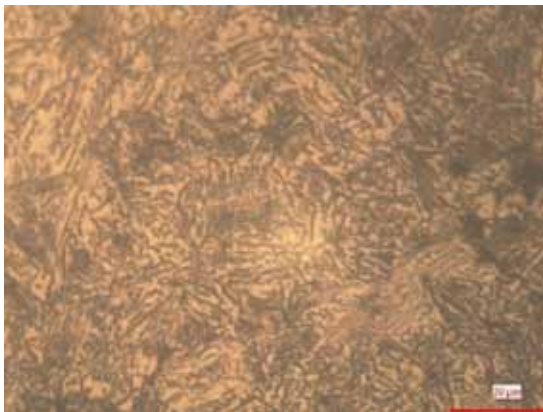


*Fig.8: Astalloy Mo + 0.6C Microstructure:  
Predominantly upper bainite with some ferrite and  
without any trace of martensite.  
Hardness: 240HV 0.5kgs*

### Remarks:

Preliminary trials shows that predominantly bainitic structure can be achieved on ASTALLOY CRM sintered parts by rapid cooling under hot furnace atmosphere & isothermal holding at the bainite transformation temperature. The prototype furnace is suitable to carry out sinter (Bainite) hardening trails for a variety of parts under different procesing conditions.

### References;

1. Microstructure and Mechanical properties of Bainitic PM Steel - Chris Schade & others, Hoeganaes Corporation.
2. The effects of processing parameters on the structure and mechanical properties of structural PM steels containing Mn, Cr and Mo – M. Sulowski; *Journal Archives of Metallurgy and Materials* Vol 59, 2014.

# ANALYSIS OF RESIDUAL THERMAL STRESSES IN MoSi<sub>2</sub> BASED PARTICULATE COMPOSITES

Manoj Kumar Jain, Jiten Das, S Deb, J Subrahmanyam and S Ray<sup>a</sup>

Defence Metallurgical Research Laboratory, Kanchan Bagh, Hyderabad, India

<sup>a</sup>Visiting Distinguished Professor, Indian Institute of Technology Mandi, Mandi, India

**Abstract** - Effort is made, in this paper, to estimate the nature and magnitude of residual thermal stresses in SiC particles reinforced MoSi<sub>2</sub> matrix composite by finite element methods (FEM) as well as analytical approach. It is observed that while SiC particles experience the constant compressive stress throughout, the MoSi<sub>2</sub> matrix has two stress components. The radial stress is compressive and maximum at particle / matrix interface. It decreases with increasing distance from the interface. It falls off to zero at free surface. The tangential (hoop) stress in the matrix is tensile in nature, which is maximum at particle / matrix interface and decreases with increasing distance with a non-zero value at the free surface.

**Keywords:** Molybdenum Disilicide, Particulate Composite, Thermal Stresses

## Introduction

Molybdenum Disilicide (MoSi<sub>2</sub>), widely employed as heating element in industrial furnaces, has attracted attention due to its unique physical and mechanical properties. Although brittle like typical ceramics at room temperature, MoSi<sub>2</sub> undergoes plastic deformation and creep at high temperatures like metals, demonstrating its potential for application in advanced high temperature structural components. Above 1200°C, It has better ductility than competitive ceramics [1] and has adequate electrical conductivity, making it amenable to electro-discharge machining [2].

Poor fracture toughness of MoSi<sub>2</sub> at temperatures below 1000°C, coupled with relatively low creep resistance is a major challenge for structural application of this material and it is necessary to toughen it at lower temperatures where MoSi<sub>2</sub> is brittle. At the same time, there is a need to increase strength at higher temperatures in order to enhance its capability as a structural material. One of the approaches to attain these twin objectives is to develop MoSi<sub>2</sub> matrix based composites using different reinforcements. Addition of brittle ceramic particles like SiC,

Si<sub>3</sub>N<sub>4</sub>, Al<sub>2</sub>O<sub>3</sub>, TiC, TiB<sub>2</sub>, ZrB<sub>2</sub> and Y<sub>2</sub>O<sub>3</sub> in MoSi<sub>2</sub> matrix has shown improvements in high temperature mechanical properties [3] and there is improvement in creep resistance as well. But fracture toughness at room temperature shows little improvement using these particulate reinforcements of brittle ceramic in MoSi<sub>2</sub>. Thus, there is a need to explore ductile reinforcements.

Ductile phase toughening of MoSi<sub>2</sub>, originally proposed by Kristic et al [4] has resulted in significant improvements in toughness of MoSi<sub>2</sub> based composites at low temperatures, primarily due to crack bridging by unbroken ductile ligaments across it. However, the use of ductile phase toughening of MoSi<sub>2</sub> has received only a very limited attention. The present work explores model tri-layer laminated composites consisting of a single ductile refractory metal foil sandwiched between two layers of MoSi<sub>2</sub> reinforced with 20 vol% SiC<sub>p</sub>. Three different tri-layer composites using ductile refractory metal foils viz. Mo, Ta and Nb were made by vacuum hot pressing at 1600°C. Due to high processing temperatures involved, residual thermal stresses are likely to develop and unless properly distributed, may pose the danger of premature failure in the laminated composites.

## ANALYSIS OF RESIDUAL THERMAL STRESSES IN MoSi<sub>2</sub> BASED PARTICULATE COMPOSITES

In a composite processed at high temperature, residual stresses are mostly thermal stresses, generated during cooling due to “constraint” on free dimensional change of a body [5]. This constraint arises in a composite because of components having different coefficients of thermal expansion. The extent of thermal expansion mismatch is more important in ceramic matrix composites as ceramic materials generally have a very low fracture strain and the processing requires high temperatures, making the problem of residual stress more severe. The thermal expansion mismatch ( $\Delta\alpha = \alpha_r - \alpha_m$ ) where  $r$  and  $m$  denote the reinforcement and the matrix, respectively, and the temperature interval ( $T_f - T_r$ ) during cooling from the high processing temperatures,  $T_r$ , to room temperature,  $T_r$ , are the key parameters deciding the extent of thermal residual stress developing in a composite. Thermal strain is estimated as  $\Delta\alpha\Delta T$ . However, the volume fraction and geometry of the reinforcement as well as the elastic moduli of the matrix and the reinforcement will also determine the thermal stresses in a given composite material.

The mechanical properties obtained in a composite will depend on the residual thermal stresses. may influence the mechanical properties of these composites. It is important to study the nature and magnitude of residual thermal stresses in MoSi<sub>2</sub> based particulate and laminated composites and the present work is limited to modelling of these composites by application of analytical methods as well as by Finite Element Methods (FEM).

### Residual Thermal Stresses in Pure MoSi<sub>2</sub>

The crystal structure of MoSi<sub>2</sub> is body centered tetragonal (C11b) as shown in Fig. 1 [2]. The large axial ratio ( $c/a = 2.45$ ) is expected to generate anisotropic stresses within individual grains after cooling from the processing temperature [6]. Moreover, anisotropy in coefficient of thermal expansion values along a-axis and c-axis is also

expected to result in residual thermal stresses in individual grains.

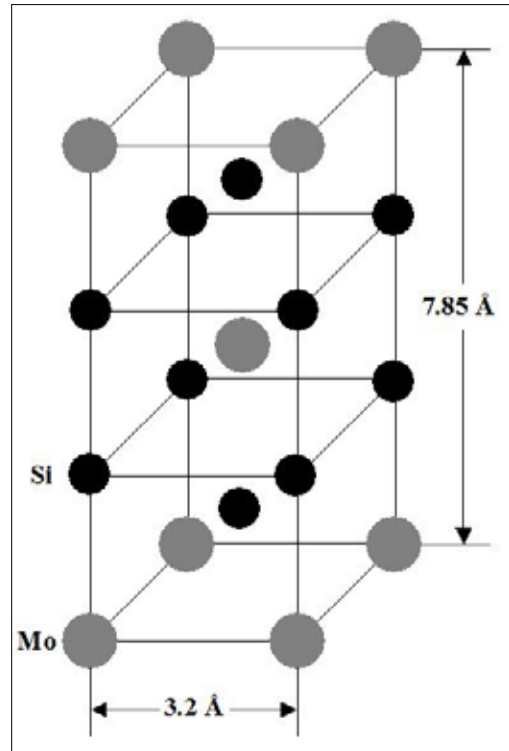


*Fig. 1 Crystal structure of MoSi<sub>2</sub>*

The maximum possible number of independent coefficients of thermal expansion (CTEs) in any crystal system is six. In different crystal systems, depending upon the symmetry, the number of independent CTEs is further reduced as shown in Table 1 [5].

*Table 1 No. of independent coefficients of thermal expansion in various crystal systems*

Crystal Structure	No. of Components	Components
Triclinic	6	$\alpha_1, \alpha_2, \alpha_3, \alpha_4, \alpha_5, \alpha_6$
Tetragonal	2	$\alpha_1 = \alpha_2 = \alpha_{\perp}$ $\alpha_3 = \alpha_{\parallel}$
Cubic	1	$\alpha_1 = \alpha_2 = \alpha_3 = \alpha$

## ANALYSIS OF RESIDUAL THERMAL STRESSES IN MoSi<sub>2</sub> BASED PARTICULATE COMPOSITES

The independent coefficients of thermal expansion of MoSi<sub>2</sub> are depicted schematically in Fig. 2.

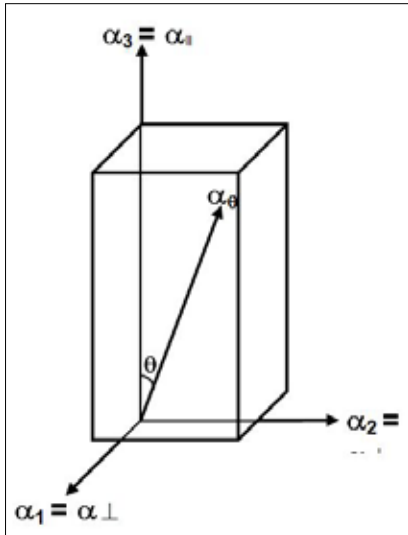


Fig. 2 Thermal expansion coefficients in tetragonal MoSi<sub>2</sub>

In MoSi<sub>2</sub> (Berkowitz, 1966):

$$\alpha_1 = \alpha_2 = \alpha_{\perp} = 8.25 \times 10^{-6} / \text{K}$$

$$\alpha_a = \alpha_{\parallel} = 9.05 \times 10^{-6} / \text{K} \text{ (parallel to c-axis)}$$

The large difference in coefficient of thermal expansion values along a-axis and c-axis is expected to generate residual thermal stresses in individual grains upon cooling from processing temperature. With increasing grain size of MoSi<sub>2</sub>, internal stresses are believed to increase. Berkowitz et al [7] estimated a residual stress of 84 MPa at room temperature in a polycrystalline MoSi<sub>2</sub> having a grain size of 80 μm.

### Effect of SiO<sub>2</sub>

The powders of MoSi<sub>2</sub> that are commercially available carry with them significant amounts of SiO<sub>2</sub> [8]. SiO<sub>2</sub> phase is found mainly at grain boundaries but it is present inside MoSi<sub>2</sub> grains also. Apart from SiO<sub>2</sub> in starting MoSi<sub>2</sub> powders,

the additional oxygen is picked up during hot pressing of MoSi<sub>2</sub> powders. Maloy et al reported the oxygen content in their hot pressed MoSi<sub>2</sub> as 2.8 wt% (~ 14 vol% SiO<sub>2</sub>), while their starting MoSi<sub>2</sub> powder contained only 0.2 wt% SiO<sub>2</sub>. MoSi<sub>2</sub> reacts with oxygen during processing, forming vitreous SiO<sub>2</sub> on the surface of MoSi<sub>2</sub> powders [9]. It forms on the surface of almost all powder particles. The SiO<sub>2</sub> on the surface of the powder particles ends up at grain boundaries in the microstructure after consolidation. The presence of vitreous SiO<sub>2</sub> within MoSi<sub>2</sub> grains and at grain boundaries is likely to increase further the internal stresses in MoSi<sub>2</sub> due to a very low coefficient of thermal expansion of SiO<sub>2</sub>, placing MoSi<sub>2</sub> grains in nonuniform tension after cooling [6].

### Residual Thermal Stresses in MoSi<sub>2</sub> - SiC Particulate Composites

In the case of a particulate composite, a stress can develop during cooling from the high processing temperatures similar to that obtained by embedding a spherical ball in a spherical hole of a relatively smaller radius. The thermal strain results from thermal expansion mismatch  $\Delta\text{CTE}$  (or  $\Delta\alpha$ ) between matrix and the reinforcement [5].

$$\text{Thermal strain} = \Delta\alpha \times \Delta T$$

$$\Delta\alpha = \alpha_r - \alpha_m$$

$\alpha_r$  = coefficient of thermal expansion of reinforcement

$\alpha_m$  = coefficient of thermal expansion of matrix

$$\Delta T = T_f - T_i \text{ (during cooling)}$$

$T_f$  = room temperature

$T_i$  = processing temperature

$\Delta T$  is always negative

In the present case of SiC particles reinforced MoSi<sub>2</sub> matrix composite,  $\alpha_m > \alpha_r$ , i.e., on cooling, matrix would tend to contract more than the reinforcement, putting the reinforcement in compression.

## ANALYSIS OF RESIDUAL THERMAL STRESSES IN MoSi<sub>2</sub> BASED PARTICULATE COMPOSITES

Based on the theory of elasticity [10], Chawla has shown that an axially symmetrical stress distribution results around each particle [5] as depicted in Fig. 3. Fig. 3 is a schematic illustration of such a particle reinforced composite in which a central SiC particle of radius,  $a$ , is surrounded by its associated spherical shell of MoSi<sub>2</sub> matrix of radius,  $b$ . The SiC particle will be under a uniform radial pressure,  $P$ , while the MoSi<sub>2</sub> matrix will have two unequal stress components:

- (i) The radial stress in the matrix will be compressive.
- (ii) The tangential (hoop) stress in the matrix will be tensile.

Chawla obtained the analytical expressions for residual thermal stresses by applying the following boundary conditions [5]:

- (i) The radial stress at the interface ( $r = a$ ) is the interfacial pressure,  $P$ .
- (ii) The radial stress at the free surface ( $r = b$ ) is zero.

The analytical expression for radial pressure,  $P$  is given by

$$P = \frac{(\alpha_m - \alpha_r)\Delta T}{\left[ \frac{0.5(1+v_m) + (1-2v_m)V_r}{E_m(1-V_r)} + \frac{1-2v_r}{E_r} \right]} \quad (1)$$

Where,  $E$  is the elastic modulus,  $v$  is the Poisson's ratio and  $V_r$  is the volume fraction of the reinforcement particles. Suffixes  $r$  and  $m$  stand for reinforcement and the matrix, respectively.

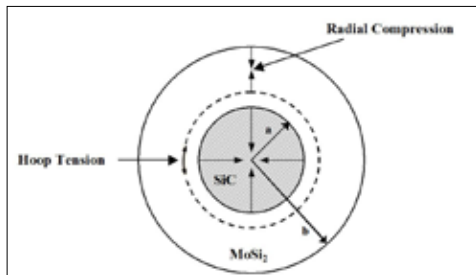


**Fig. 3 Residual thermal stresses in a particle reinforced composite consisting of a SiC particle of radius,  $a$ , embedded in a MoSi<sub>2</sub> matrix of radius,  $b$**

The expressions for the radial stress,  $\sigma_r$  and the tangential stress,  $\sigma_\theta$  in the matrix as obtained by Chawla [5] are given by:

$$\sigma_r = \frac{P}{(1-V_r)} \left[ \frac{a^3}{r^3} - V_r \right] \quad (2)$$

$$\sigma_\theta = -\frac{P}{(1-V_r)} \left[ \frac{a^3}{2r^3} + V_r \right] \quad (3)$$

Where,  $r$  is the distance from the center of the SiC particle and  $V_r = \left(\frac{a}{b}\right)^3$

### Residual Stresses in SiC Particles

MoSi<sub>2</sub> due to its tetragonal crystal structure has two independent coefficients of thermal expansion,  $\alpha_1 = \alpha_2 = \alpha_\perp$  and  $\alpha_3 = \alpha_\parallel$  (parallel to c-axis). Referring to Fig. 2, in any arbitrary direction  $[hkl]$ , if its direction cosines are  $n_1, n_2$  and  $n_3$ , the  $\alpha_{hkl}$  in that direction can be written as [5]:

$$\alpha_{hkl} = n_1^2 \alpha_1 + n_2^2 \alpha_2 + n_3^2 \alpha_3$$

Where,  $n_1^2 + n_2^2 + n_3^2 = 1$

$$\begin{aligned} \text{In MoSi}_2, \alpha_{hkl} &= (n_1^2 + n_2^2) \alpha_\perp + n_3^2 \alpha_\parallel \\ &= (1-n_3^2) \alpha_\perp + n_3^2 \alpha_\parallel = \alpha_\perp + (\alpha_\parallel - \alpha_\perp) n_3^2 \end{aligned}$$

$n_3 = \cos\theta$ , where  $\theta$  is the angle between the direction  $[hkl]$  and c-axis.

Therefore,  $\alpha_{hkl} = \alpha_\perp + (\alpha_\parallel - \alpha_\perp) \cos^2\theta$

At  $\theta = 90^\circ$   $\alpha = \alpha_\perp = 8.25 \times 10^{-6}/K$  (minimum value of  $\alpha$  along a-axis)

$\theta = 0^\circ$   $\alpha = \alpha_\parallel = 9.05 \times 10^{-6}/K$  (maximum value of  $\alpha$  along c-axis)

$\theta = 45^\circ$   $\alpha = \alpha_{45} = 8.65 \times 10^{-6}/K$

In all other directions ( $0 < \theta < 90$ ),  $\alpha$  will vary from  $8.25 \times 10^{-6}/K$  to  $9.05 \times 10^{-6}/K$ . Assuming that grains are oriented randomly in a polycrystalline MoSi<sub>2</sub>, it is probably most appropriate to take an average of the values along three axial directions as the coefficient of thermal expansion of polycrystalline MoSi<sub>2</sub>. Therefore,

$$\alpha_{\text{MoSi}_2} (\alpha_\perp + \alpha_\perp + \alpha_\parallel) / 3 = 8.52 \times 10^{-6}/K$$

## ANALYSIS OF RESIDUAL THERMAL STRESSES IN MoSi<sub>2</sub> BASED PARTICULATE COMPOSITES

SiC used in the present study was of  $\beta$ -type having a cubic crystal structure. In cubic structures,  $\alpha_1 = \alpha_2 = \alpha_3 = \alpha$ . Therefore, coefficient of thermal expansion of polycrystalline  $\beta$ -SiC, =  $4.78 \times 10^{-6}/K$ .

The values of other properties for the materials and processing parameters used in the present composite system are given in Table 2.

**Table 2 Material properties and processing parameters for MoSi<sub>2</sub>/SiC<sub>p</sub> composite**

Material	$\alpha$ ( $\times 10^{-6}/K$ )	$E$ (GPa)	$\nu$	$V_r$	$\Delta T$ (K)
MoSi <sub>2</sub>	8.52	440	0.15	0.2	-1570
SiC	4.78	420	0.14		

Substituting the above values in equation (1) yields a residual thermal stress in SiC particle,  $P = 1568$  MPa (compressive). SiC particle will be under a uniform compressive stress,  $P$ .  $P$  is constant and does not vary from  $r = 0$  to  $r = a$ . Corten [11] has provided expression for estimating the radial stress but it is for two dimensional case while that used by *Timoshenko and Goodier* [10], *Selsing* [12] and *Venkateswara Rao et al* [13] does not show dependence of volume fraction of the reinforcement or matrix.

(Note: In literature, researchers have used different expressions to estimate the radial stress in the particle. Some of them are:

1. For a 2-dimensional problem in plane strain consisting of a circular reinforcement particle embedded in an infinite matrix, the particle experiences a radial stress,  $P$ , which is given by Corten [11]:

$$P = \frac{(\alpha_r - \alpha_m) \Delta T}{\frac{(1 + \nu_r)}{E_r} + \frac{(1 + \nu_m)}{E_m}}$$

2. *Timoshenko and Goodier* [10], *Selsing* [12] and *Venkateswara Rao et al* [13] have used the following expression to calculate the radial stress:

$$P = \frac{\Delta\alpha\Delta T}{\frac{(1-2\nu_r)}{E_r} + \frac{(1+\nu_m)}{2E_m}}$$

However, the above expressions seem to be less vigorous as these do not include the term,  $V_r$ , i.e., the effect of volume fraction of the reinforcement particles.)

### Residual Stresses in MoSi<sub>2</sub> Matrix

#### The Radial Stress, $\sigma_r$

The radial stress in MoSi<sub>2</sub> matrix is compressive and vary with distance,  $r$ . At particle / matrix interface ( $r = a$ ),  $\sigma_r = P$  and at free surface located at ( $r = b$ ),  $\sigma_r = 0$  (as per the boundary conditions).

$$V_r = \left(\frac{a}{b}\right)^3 \text{ Therefore, } b = \frac{a}{(V_r)^{1/3}} \quad (4)$$

In the present study, the average particle size of SiC used was  $2 \mu\text{m}$  ( $a = 1 \mu\text{m}$ ) and  $V_r = 0.2$ . Substituting these values in equation 4 yields  $\sigma_r = 0$  at  $r = 1.7 \mu\text{m}$ . The variation of  $\sigma_r$  with distance  $r$  is schematically presented in Fig. 4. In Fig. 4,  $ab = 0.7 \mu\text{m}$ .

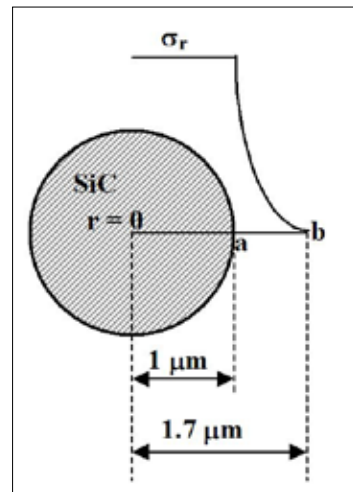


**Fig. 4 The variation of radial stress,  $\sigma_r$  with distance  $r$  in MoSi<sub>2</sub> matrix**

## ANALYSIS OF RESIDUAL THERMAL STRESSES IN MoSi<sub>2</sub> BASED PARTICULATE COMPOSITES

The radial compressive stress in MoSi<sub>2</sub> matrix is maximum at particle / matrix interface. The stress decreases with increasing distance from the interface and falls off to zero at a distance of 0.7 μm away from the particle / matrix interface.

### The Tangential (Hoop) Stress, $\sigma_r$

The tangential stress in the matrix also varies with distance,  $r$ . At  $r = a$  (particle / matrix interface), from equation 3

$$\sigma_0 = -\frac{P}{(1-V_r)} \left[ \frac{1}{2} + V_r \right] = 0.875P = 1372 \text{ MPa (tensile).}$$

At  $r = b$  (free surface), from equation 3

$$\begin{aligned} \sigma_0 &= -\frac{P}{(1-V_r)} \left[ \frac{1}{2} \frac{a^3}{b^3} + V_r \right] = -\frac{P}{(1-V_r)} \left[ \frac{1}{2} V_r + V_r \right] \\ &= -\frac{3}{2} \frac{PV_r}{(1-V_r)} = 0.375P = 588 \text{ MPa (tensile)} \end{aligned}$$

The above results reveal the following:

- (i) The tangential hoop stress,  $\sigma_0$  in MoSi<sub>2</sub> matrix is tensile in nature.
- (ii)  $\sigma_0$  is maximum at particle / matrix interface.
- (iii)  $\sigma_0$  decreases with increasing  $r$ , but never reaches to a zero value inside MoSi<sub>2</sub> matrix.

The graphical representation of the above results is shown schematically in Fig. 5. The tangential hoop stress in MoSi<sub>2</sub> matrix has a non-zero value at the free surface.

### Analysis of Residual Thermal Stresses by Finite Element Methods (FEM)

To check the validity of the analytical results, the problem was solved by finite element analysis using a commercially available FEM package, NISA 11.0 developed and marketed by EMRI Private Limited, India, a subsidiary of Engineering Mechanics Research Corporation

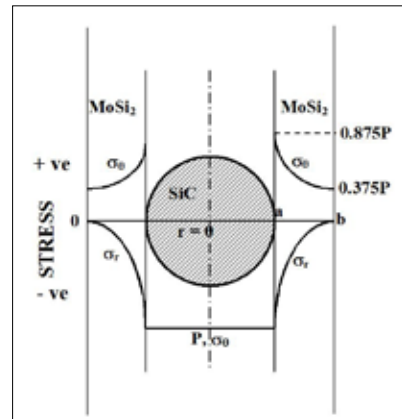


Fig. 5 Residual thermal stresses (radial,  $\sigma_r$  and tangential,  $\sigma_0$  components) in MoSi<sub>2</sub> matrix varying with distance

(EMRC), USA. NISA is a general purpose modular type finite element program and is one of the most comprehensive and versatile programmes to solve a wide range of static, dynamic, buckling, heat transfer and nonlinear analysis problems encountered in aerospace, mechanical and civil engineering environments. The programmes are completely integrated through an interactive graphical interface "Display IV" (Pre and Post Processor). The software is tailored specifically for accurate and efficient analysis of a wide range of structures due to large element library. The software generates solution using simple incremental techniques. The problem in the present investigation was formulated using NISA Display-IV Pre-Processor module and was solved using NISA Linear Static Analysis module. In linear analysis, the material properties are assumed to be constant (or dependent only on temperature). In an isotropic linear elastic case, the elastic constants are assumed to be independent of the direction, i.e., they do not change with any orthogonal transformation of axes. Linear static analysis is performed to predict the response of a structure under time independent applied loads (loading due to thermal expansion / contraction). Loads

## ANALYSIS OF RESIDUAL THERMAL STRESSES IN MoSi<sub>2</sub> BASED PARTICULATE COMPOSITES

due to thermal expansion or contraction may be applied to any element, which has a thermal expansion coefficient as a material property.

NISA provides the components of the stress tensor in the global and/or local XYZ Cartesian coordinate system. In order to establish the directions of the stress components, an infinitesimal cube is considered at the point of interest. The positive stresses act on the positive faces of the cube in the positive direction. The components of the stress tensor are the direct stresses  $\sigma_{xx}$ ,  $\sigma_{yy}$ ,  $\sigma_{zz}$  and the shear stresses  $\sigma_{xy}$ ,  $\sigma_{yz}$ ,  $\sigma_{xz}$  ( $= \sigma_{yx}$ ,  $\sigma_{zy}$ ,  $\sigma_{zx}$ , respectively). The first subscript indicates the face on which the stress is acting and the second subscript gives the direction. In the present work,  $\sigma_{xx}$  stress contour plots were generated using Display-IV Post-Processor module, which is a three-dimensional colour graphics programme with extensive plotting features for displaying the results.

The model considered for the analytical case assumes a spherical SiC particle of 1  $\mu\text{m}$  radius, embedded in a spherical MoSi<sub>2</sub> matrix with a volume fraction of the reinforcement particles as 0.2. For the purpose of numerical analysis also, a spherical SiC particle of the same radius within a spherical matrix with the same volume fraction of the reinforcement particles was considered. However, due to a shortcoming of the FEM package used, it was not possible to model the shape of these two concentric spheres exactly as spherical. A certain degree of approximation was used in the model, which is shown in Fig. 6.

Essentially, instead of perfect geometrical spheres, the two entities (reinforcement and the matrix) of the model were constructed of small cubical elements as shown in the cross-sectional view in Fig. 6. In Fig. 6, the red elements represent the MoSi<sub>2</sub> matrix and the green elements represent the SiC particle. Due to this the surface of the model was not totally smooth and consisted of a number of small steps and sharp corners. The

interface between the particle and the matrix was assumed to be perfectly strong.

The stress ( $\sigma_{xx}$ ) contour pattern is shown in Fig. 7 for the whole system, i.e., the matrix and the reinforcement. This pattern shows the presence of an almost stress free zone on the surface of the composite sphere along the x-axis. This is the radial stress component acting in the matrix. There is another vertical zone of tensile stress running along the central portion of the matrix, which is the tangential stress component. The other small patches occurring at the sharp angled corners on the matrix surface are discarded as they have originated from the roughness of the model geometry.

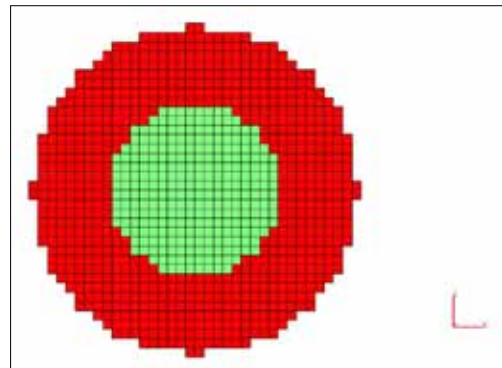


Fig. 6 Cross-sectional view of the model of composite used for the FEM analysis (Green - SiC particle and Red - MoSi<sub>2</sub> matrix)

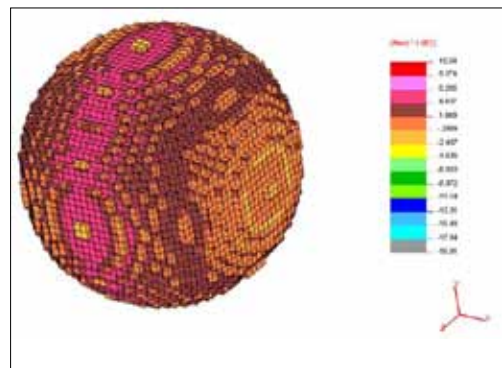


Fig. 7 Isometric view of the stress ( $\sigma_{xx}$ ) contour pattern of the composite

## ANALYSIS OF RESIDUAL THERMAL STRESSES IN MoSi<sub>2</sub> BASED PARTICULATE COMPOSITES

The stress state in the MoSi<sub>2</sub> matrix is more clearly visible in Fig. 8, which shows the stress contour on an equatorial cross-section of the matrix. The reinforcement particle is not shown in this figure for clarity. As described earlier, the residual thermal stress in the matrix will have two different components, (i) a radial compressive stress and (ii) a tangential tensile stress. The stress contour pattern in Fig. 8 exhibits the existence of both types of stresses. Along the line AA in Fig. 8, the direction of  $\sigma_{xx}$  is radial and it is compressive in nature. Its magnitude is 1437 MPa at the particle / matrix interface which decays to 42 MPa compressive at the free surface.

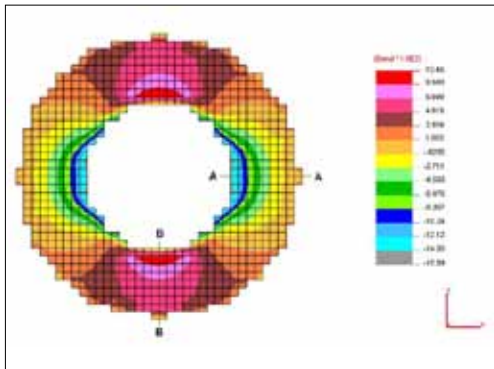


Fig. 8 Stress contour pattern on an equatorial cross-section of the MoSi<sub>2</sub> matrix (SiC particle not shown)

The variation of radial compressive stress with distance in the matrix as obtained by FEM analysis is graphically represented in Fig. 9. The stress distribution in the matrix is found to be similar with the analytical results as described earlier, which says that the radial stress in the matrix is compressive and varies with the distance as per equation 2. The calculated stress values from equation 2 are also plotted in Fig. 9 for comparison with FEM results. These two plots are found to be in good agreement except that the stress values obtained from FEM analysis are slightly lower than the stress values calculated by analytical method.

The magnitude of tensile hoop stress at the particle / matrix interface was found to be 1037 MPa by FEM analysis, which is lower than the analytically calculated value of 1372 MPa. In numerical solution the magnitude of this stress reduces with increasing distance from the interface as graphically represented in Fig. 10. The stress values calculated from equation 3 are also plotted in Fig. 10 for comparison with FEM results. The stress values obtained from FEM analysis are slightly lower than the calculated stress values by analytical method. However, the same trend is predicted by the results obtained from both the methods. The variation present in between the two plots may be attributed to a slightly different volume fraction of reinforcement particles as a result of roughness of the interface in the numerical model.

Fig. 11 shows an isometric view of stress contour pattern of only SiC particle with the matrix removed. It reveals the presence of compressive stress all over the surface of the particle. It can be seen from Fig. 11 that a zone of higher compressive stresses runs along the central portion of the particle along the x-axis. Another band of relatively lower compressive stresses exists normal to the previous zone on the YZ plane. The small irregular patches of varying stress concentration on the surface are ignored as they have resulted from the ridged nature of the surface of the model.

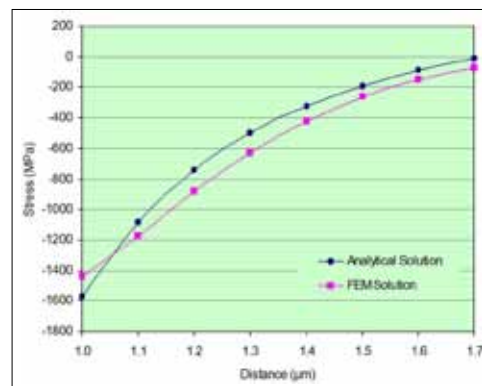


Fig. 9 Variation of radial compressive stress with distance in MoSi<sub>2</sub> matrix

## ANALYSIS OF RESIDUAL THERMAL STRESSES IN MoSi<sub>2</sub> BASED PARTICULATE COMPOSITES

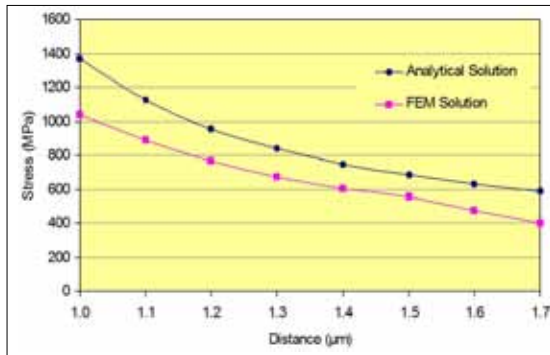


Fig. 10 Variation of tangential tensile (hoop) stress with distance in MoSi<sub>2</sub> matrix

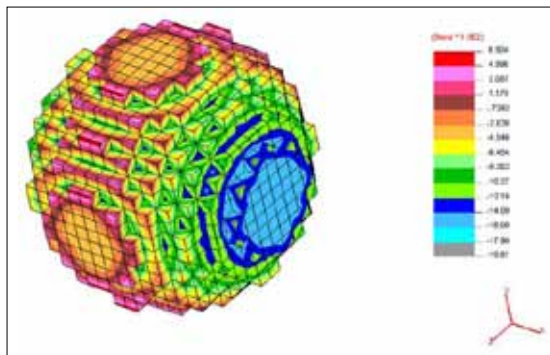


Fig. 11 Stress contour pattern of SiC particle (MoSi<sub>2</sub> matrix not shown).

The interior of the particle is shown in a cross-sectional view in Fig. 12. It is evident from Fig. 12 that inside bulk of the particle the stress is almost uniform and compressive in nature. The magnitude of this compressive stress is estimated to be 1680 MPa, which is matching closely with the analytically calculated value of 1568 MPa. The irregularities in the form of gray areas with higher compressive stress near the periphery of the particle are again mostly caused by the sharp angled vertices on the interface and hence are ignored.

### Thermal Stresses - Criterion for Matrix Cracking

The above analysis clearly reveals that the composites processed in the present study

contain large magnitudes of residual thermal stresses. In case of ceramic matrix composites, cracking may occur in the matrix to relieve the high level of thermal stresses while, in metal matrix composites, matrix is likely to deform plastically instead of cracking. However, in spite of these high residual stresses, no cracking was observed in MoSi<sub>2</sub> matrix in as processed condition at room temperature. This is in agreement with the criterion for matrix cracking as proposed by Lu et al [14-15]. They have described a non-dimensional quantity, R, which relates the thermal expansion mismatch stress ( $\sigma$ ) to the fracture toughness of the matrix ( $K_{IC}$ ) and the size of the reinforcement phase ( $r$ ) by

$$R = r \left( \frac{\sigma}{K_{IC}} \right)^2 \quad (5)$$

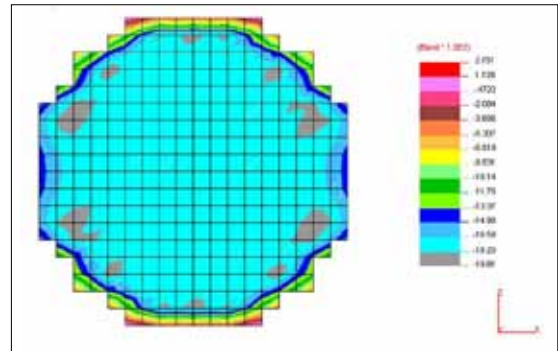


Fig. 12 A cross-sectional view of the stress contour pattern inside the SiC particle

Where,  $r$  = particle radius for particulate composites

= fiber radius for fiber reinforced composites

When  $R \leq 1$  the matrix cracking will not occur. When  $R > 10$  all forms of matrix cracking will occur profusely. A large particle size, higher residual thermal stresses and a low fracture toughness of the matrix material will promote matrix cracking.

# ANALYSIS OF RESIDUAL THERMAL STRESSES IN MoSi<sub>2</sub> BASED PARTICULATE COMPOSITES

In the present case of MoSi<sub>2</sub> + 20 vol. % SiC<sub>p</sub> Composite:

The residual thermal tensile stress in the matrix,  $\sigma_0 = 1372$  MPa. Fracture toughness of MoSi<sub>2</sub> matrix,  $K_{IC} = 3.0$  MPa $\sqrt{m}$  [16]. The average radius of SiC particles,  $r = 1 \mu\text{m} = 1 \times 10^{-6}$  m. Substituting these values in equation (5) results in  $R = 0.21$  which is  $< 1$ . Therefore, no cracking in MoSi<sub>2</sub> matrix will occur.

## Limitations

The various limitations of the analysis to estimate the residual thermal stresses in MoSi<sub>2</sub> / SiC particulate composite carried out in the present work by analytical as well as FEM methods are summarized below:

1. Coefficients of thermal expansion (CTEs) of MoSi<sub>2</sub> and SiC have been assumed to be constant with temperature.
2. The effect of SiO<sub>2</sub> in MoSi<sub>2</sub> has not been taken into account. The commercial MoSi<sub>2</sub> powders contain significant amounts of SiO<sub>2</sub>. The coefficient of thermal expansion of SiO<sub>2</sub> is very low ( $\alpha = 0.55 \times 10^{-6}/\text{K}$ ). This may result in a net value of coefficient of thermal expansion of the MoSi<sub>2</sub> matrix considerably lower leading to a lower thermal expansion mismatch with SiC. Therefore, the values of residual thermal stresses arrived at in the present analysis may be an over-estimation.
3. SiC particles are assumed to be spherical, to be of the same size and having a uniform distribution. However, in the present study, SiC particles used were of irregular shape and of different sizes (having a large size distribution). The SiC particles have only a reasonably good uniform distribution in the matrix as shown in Fig. 13.
4. No stress relaxation was assumed during cooling from the processing temperature. In case of ceramic matrix composites (CMCs),

cracking may occur in the matrix to relieve the high level of thermal stresses. In metal matrix composites (MMCs), matrix is likely to deform plastically instead of cracking. However, in MoSi<sub>2</sub> based composites some stress relaxation during cooling will occur as MoSi<sub>2</sub> shows ductility at elevated temperatures.

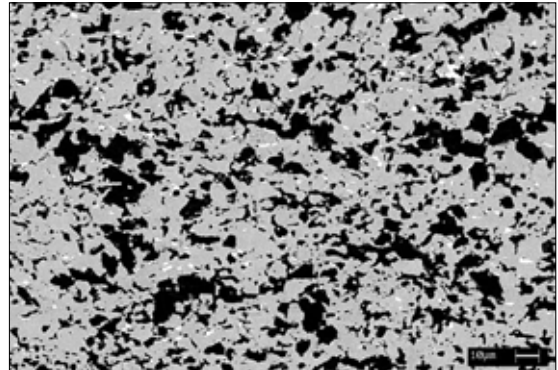


*Fig. 13 SEM back scattered electron image of MoSi<sub>2</sub> + 20 vol. % SiC<sub>p</sub> composite showing distribution of SiC particles in MoSi<sub>2</sub> matrix*

## Conclusions

In the present investigation, an attempt has been made to evaluate the nature and magnitude of residual thermal stresses in SiC particles reinforced MoSi<sub>2</sub> matrix composite by theoretical methods. It was found that

1. SiC particles are under compressive stress which is constant and does not vary within the particle from the centre of the particle to the particle / matrix interface.
2. The MoSi<sub>2</sub> matrix has two stress components. The radial stress is compressive and maximum at particle / matrix interface. It decreases with increasing distance from the interface. It falls off to zero at free surface (free surfaces do not support the normal stresses). The tangential (hoop) stress in the matrix is tensile in nature, which is maximum

# ANALYSIS OF RESIDUAL THERMAL STRESSES IN MoSi<sub>2</sub> BASED PARTICULATE COMPOSITES

at particle / matrix interface and decreases with increasing distance with a non-zero value at the free surface.

3. The residual thermal stresses estimated by finite element methods (FEM) are found to be similar to the as calculated by analytical approach, thus validating the analytical expressions used in the present study.

## Acknowledgements

The authors are thankful to Dr S V Kamat, Outstanding Scientist & Director, DMRL for his support and DRDO for funding to carry out this work.

## References

1. K. Badrinarayanan, A. L. Mckelvey, K. T. Venkateswara Rao and R. O. Ritchie, "Fracture and Fatigue Crack Growth Behaviour in Ductile Phase Toughened MoSi<sub>2</sub>: Effects of Nb Wire vs. Particulate Reinforcements", *Met. Mater. Trans. A*, **27A**, 3781-3792, (1996).
2. J. J. Petrovic, "Mechanical Behaviour of MoSi<sub>2</sub> and MoSi<sub>2</sub> Composites", *Mater. Sci. Engg.*, **A192/193**, 31-37, (1995).
3. A. K. Vasudevan and J. J. Petrovic, "A Comparative Overview of MoSi<sub>2</sub> Composites", *Mater. Sci. Engg.*, **A155**, 1-17, (1992).
4. V. K. Krstic, P. S. Nicholson and R. G. Hoagland, "Toughening of Glasses by Metal Particles", *J. Am. Cer. Soc.*, **64**, 499-504. (1981)
5. K. K. Chawla, *Ceramic Matrix Composites*, (Chapman and Hall, London, 1993).
6. R. K. Wade and J. J. Petrovic, "Fracture Modes in MoSi<sub>2</sub>", *J. Am. Cer. Soc.*, **75**, 1682 - 1684, (1992).
7. J. B. Berkowitz-Mattuck, M. Rossetti and D. W. Lee, "Enhanced Oxidation of MoSi<sub>2</sub> Under Tensile Stress: Relation to Pest Mechanism", *Met. Trans.*, **1**, 479-483, (1970).
8. D. A. Hardwick, P. L. Martin and R. J. Moores, "Reaction Synthesis of MoSi<sub>2</sub> from High Purity Elemental Powders", *Script. Met.* **27**, 391-394, (1992).
9. S. A. Maloy, A. H. Heuer, J. J. Lewandowski and J. J. Petrovic, "Carbon Additions to MoSi<sub>2</sub>: Improved High Temperature Mechanical Properties", *J. Am. Cer. Soc.*, **74**, 2704-2706, (1991).
10. S. Timoshenko and J. N. Goodier, *Theory of Elasticity*, pp.416, (McGraw-Hill, New York, 1951).
11. J. T. Corten, "Micromechanics and Fracture Behaviour of Composites" in *Modern Composite Materials*, L. J. Broutman and R. H. Krock (Eds.), pp. 20-30, (Addison-Wesley, Massachusetts, 1967).
12. J. Selsing, "Internal Stresses in Ceramics", *J. Am. Cer. Soc.*, **44**, 419, (1961).
13. K. T. Venkateswara Rao, W. O. Soboyejo and R. O. Ritchie, "Ductile Phase Toughening and Fatigue Crack Growth in Nb Reinforced MoSi<sub>2</sub> Intermetallic Composites", *Met. Trans. A*, **23A**, 2249-2257, (1992).
14. T. C. Lu, A. G. Evans, R. J. Hecht and R. Mehrabian, "Toughening of MoSi<sub>2</sub> with a Ductile (Niobium) Reinforcement", *Acta Met. Mater.* **39**, 1853-1862, (1991).
15. T. C. Lu, J. Yang, A. G. Evans, R. J. Hecht and R. Mehrabian, "Matrix Cracking in Intermetallic Composites Caused by Thermal Expansion Mismatch", *Acta Met. Mater.*, **39**, 1883-1890, (1991).
16. L. Xiao, Y. S. Kim and R. Abbaschian, "Ductile Phase Toughening of MoSi<sub>2</sub> - Chemical Compatibility and Fracture toughness", *Intermetallic Matrix Composites, Proceedings Materials Research Society Symposium*, **194**, 399-404, (1990).

# MICROSTRUCTURAL INVESTIGATIONS ON HOT ISOSTATICALLY PROCESSED PM NICKEL BASE SUPERALLOY

B. Sreenu\*, Subhradeep Chatterjee<sup>1</sup> and G. Appa Rao

Defence Metallurgical Research Laboratory, Kancharbagh, Hyderabad 500058, India

<sup>1</sup>Dept. of Materials Science & Metallurgical Engineering, IIT, Hyderabad 502285, India

**Abstract** - Nickel base superalloy powder of composition comparable to that of the superalloy N18 was hot isostatically pressed (HIPed) at  $1190 \pm 2$  °C under 120 MPa pressure for 3 h of sustaining time. Subsequently, the HIPed billet was subjected to near isothermal forging (NIF) by soaking at  $1170^\circ\text{C}/2\text{h}$ , with die temperature of  $920$  °C. The samples from HIP+forged alloy were extracted and subjected to solutionising treatment at  $1165^\circ/4\text{h}$ /oil quenching. Subsequently, these samples were given dual-ageing treatment at  $700$  °C /  $24\text{h}$  / AC and  $800$  °C /  $4\text{h}$  / AC. The microstructural characterization was carried out on (i) as-forged, (ii) forged + solution treated and (iii) forged + fully treated (i.e. solution treatment+aging) material. The forged and fully heat treated material has shown equiaxed grains of varied size between  $2\text{-}43$   $\mu\text{m}$  with an average grain size  $\sim 5$   $\mu\text{m}$ . The heat treated alloy further revealed that the microstructure is free from the undesirable phases such as prior particle boundary (PPB) networks. The  $\text{M}_{23}\text{C}_6$  and MC type carbides enriched with Cr and Ti, respectively, were present at the grain boundaries. Hafnium oxide particles, disrupted during forging were also seen at the grain boundaries as well in the matrix. The processing and microstructural details on HIP+forged and HIP+forged and fully heat treated material is presented in this paper.

**Key words:** Hot isostatic pressing, near isothermal forging, superalloy, prior particle boundaries.

## Introduction

Fabrication of powder metallurgy (P/M) nickel-base superalloy turbine discs generally involves number of steps, which mainly includes powder production, hot isostatic pressing (HIP), isothermal or near-isothermal forging (NIF) and optimum heat treatment to realize the microstructure with improved properties. In P/M route, generally, two different techniques (i.e. hot isostatic pressing (HIPing) or hot extrusion (HE)) are adopted for consolidation of powder to produce the billets for subsequent forging. In the former route, HIPing of powder is carried out to obtain the billets or preforms which are subsequently hot worked to produce the discs. In the later route, the powders or HIPed compacts are subjected to extrusion to produce billets having a fine grain size and these billets are then used as feed-stock for superplastic

forming under isothermal conditions to produce the components. In the present study, superalloy powder produced by Inert-gas (Ar) atomisation technique (IGA) was consolidated by HIPing at  $\gamma'$ -solvus temperature ( $1190 \pm 2^\circ\text{C}$ ). Subsequently, the as-HIPed billet was subjected to near-isothermal forging (NIF) to accomplish the microstructure free from prior particle boundaries (PPBs). The detailed microstructure of alloy has been carried out and presented in the following section.

## Experimental Work

Hot isostatic pressing of superalloy powder: The nominal composition of nickel-base superalloy powder used in this study is given in Table-1. For consolidation of alloy powder, capsule of size 80 mm diameter and 95 mm height was fabricated from AISI-304 stainless steel tube having 2 mm

# MICROSTRUCTURAL INVESTIGATIONS ON HOT ISOSTATICALLY PROCESSED PM NICKEL BASE SUPERALLOY

wall thickness. The steel capsule was filled with superalloy powder and de-gassed at room temperature (RT) until a vacuum level of  $10^{-5}$  torr is achieved using diffusion pump. Subsequently, the capsule was introduced into furnace for degassing at elevated temperature of about  $800^{\circ}\text{C}$  for 16 hours. After attaining a stable vacuum level of  $6 \times 10^{-6}$  torr, the capsule was crimp-sealed under dynamic vacuum condition. The crimp-sealed capsule was loaded into Laboratory-HIP (Model: EPSI-SO11144) and powder mass has been consolidated at  $1190 \pm 2^{\circ}\text{C}$  under a pressure of 120 MPa for 3 h of sustaining time.

*Table-1: Composition of superalloy powder (wt.%)*

Co	Cr	Mo	Al	Ti	Hf	C	B	Zr	Ni
15.4	12.5	6.3	4.5	4.6	0.49	0.021	0.014	0.030	Bal.

Oxygen content of powder: 120 ppm

**Near-isothermal forging and heat treatment :** For subsequent near-isothermal forging experiment, the HIPed compact was heated at  $1170^{\circ}\text{C}$  for 2hrs and forged with a speed of 0.5mm/s, at the die temperature of  $920^{\circ}\text{C}$ . Five-step forging with 15 minutes intermittent heating was adopted for realizing the 50% deformation on the HIPed compact. The samples of 10mm diameter extracted from interior of the forged compact by wire-cut EDM were used for evaluation of metallurgical properties. To refine and improve the microstructure, the as-forged material was subjected to heat treatment. Initially, the HIP+forged samples were solution treated at  $1165^{\circ}\text{C}$  for 4 hour and fast cooled to room temperature by oil quenching. Subsequently, double-ageing treatment for the solution treated samples was carried out at  $700^{\circ}\text{C}$  for 24 hours and air cooled to room temperature +  $800^{\circ}\text{C}$  for 4 hours and air cooled to room temperature.

**Microstructural characterization:** Microstructure of as-forged and forged + fully heat treated material was examined by optical microscope (OM) and scanning electron microscope (SEM) while the size and distribution of the grains were determined by using electron back scattered

diffraction (EBSD) [Oxford, UK] attached with field emission scanning electron microscope (FESEM) [Supra55, Carl Zeiss, Germany]. Electron probe microanalysis (EPMA) was carried out on the forged + heat treated material to find out the composition of prior particle boundary (PPB) precipitates. Transmission electron microscope (TEM) [Tecnai 20 T G2, FEI, Netherland] was used to find out the phases present in the forged + fully heat treated material.

## Results

**Microstructure of as-forged material:** The optical microstructures of near-isothermally forged material, in transverse and longitudinal directions are presented in Fig.1, respectively, reveals deformed grain structure. The aspect ratio of grains (L/D) in as-forged material varies between 1.5 and 2.0.

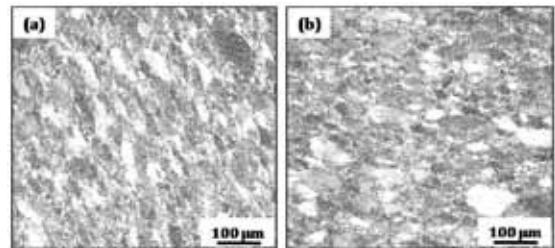


*Fig.1 Optical micrographs of HIP + forged material in (a) Transverse and (b) Longitudinal direction*

This indicates that considerable deformation has been taken place in the material during forging. The microstructure of the as-forged material further reveals the disruption of PPB networks, which are commonly present in the as-HIPed material [1,2]. The scanning electron micrographs of as-forged alloy presented in the Fig.2 reveal primary and secondary  $\gamma'$ -precipitates at the grain boundaries and within the grains, respectively. The size and volume fraction of coarse primary  $\gamma'$  precipitate are found to be  $6 \pm 2 \mu\text{m}$  and  $13 \pm 2\%$  respectively

## MICROSTRUCTURAL INVESTIGATIONS ON HOT ISOSTATICALLY PROCESSED PM NICKEL BASE SUPERALLOY

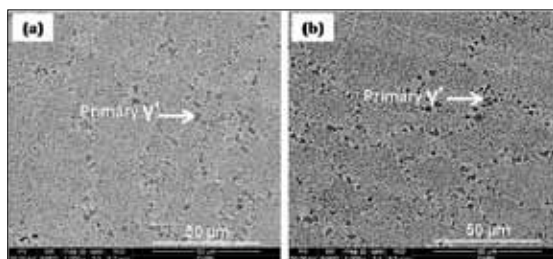


**Fig.2. SEM micrographs of HIP + forged material in (a) Transverse and (b) Longitudinal direction**

The inverse pole figure (IPF) colour map superimposed with band contrast image obtained from EBSD in as-forged condition is shown in Fig.3.a. The microstructure is characterized by the presence of deformed coarse grained structure and fine re-crystallized grains. The grain size distribution estimated by linear intercept method illustrated in Fig.3.b reveals bimodal or duplex grain size distribution owing to the presence of deformed and recrystallized grain structure. The average grain size in as-forged condition is estimated of about  $\sim 5 \mu\text{m}$ .

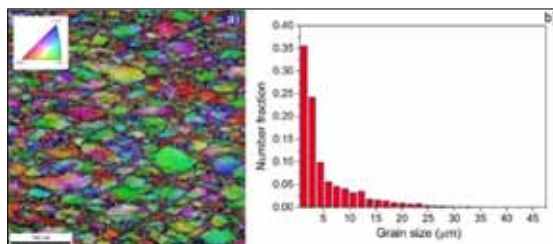


**Fig.3 (a). IPF colour map superimposed with band contrast image and (b) grain size distribution obtained from EBSD analysis of as-forged material.**

The deformed state of the superalloy is further substantiated by the orientation imaging microscopy (OIM) image depicting the grain boundaries shown in Fig.4.a, which clearly reveals the evolution of high angle grain boundaries (HAGBs) and low angle grain boundaries (LAGBs) having misorientation angles  $\theta > 15^\circ$  and  $2^\circ < \theta < 15^\circ$ , respectively. HAGBs and LAGBs are highlighted in black and red colour respectively. The OIM map is prevalent of LAGBs constituting

of 65% which substantiates the deformed nature of the superalloy in as-forged condition. Similar observation is also manifested by the misorientation angle distribution illustrated in Fig.4.b wherein an average misorientation angle ( $\theta_{\text{avg}}$ ) is estimated of about  $18.4^\circ$ .

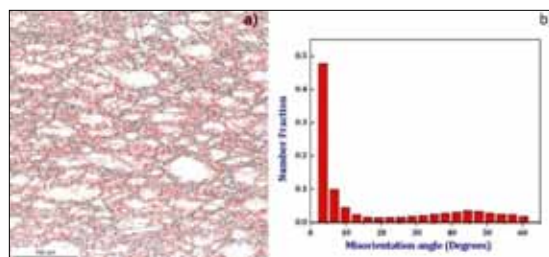


**Fig.4 (a) OIM map showing HAGBs (black colour and LAGBs (red colour) in the HIP+forged material (b) misorientation angle distribution in the HIP+forged material.**

Microstructure of forged + solution treated material: To refine the microstructure and improve mechanical properties, appropriate heat treatment, consisting of solutionising treatment followed by double-aging treatment is generally adopted for forged material [3]. In this connection, the as-forged alloy was subjected to solutionising treatment at  $1165^\circ\text{C}$  for 4 hours followed by oil quenching. The optical microstructure of forged+solution treated alloy presented in Fig.5.a reveals presence of fine secondary  $\gamma'$  precipitates within the grains. The similar features can also be seen in the SEM micrograph presented in Fig.5.b. The secondary  $\gamma'$ -precipitates which were promptly seen in the as-forged material have been dissolved to a greater extent during solutionising treatment.

The IPF colour map obtained from EBSD after solution treatment is shown in Fig.6.a. The microstructure is characterized by the dominance of fine equiaxed grain formed by dynamic recrystallization during near isothermal forging. In addition to that, moderate sized coarse grains (indicated by white arrow) and abnormally large sized coarse grains (indicated by black arrows)

# MICROSTRUCTURAL INVESTIGATIONS ON HOT ISOSTATICALLY PROCESSED PM NICKEL BASE SUPERALLOY

are also present. The coarse grained structure observed in as-forged material remains almost unchanged during solutionising treatment. This is mainly attributed to the grain boundary pinning effect provided by the primary  $\gamma'$ -precipitates present along the grain-boundaries, thereby retarding grain growth. On the other hand, the fine re-crystallized equiaxed structure observed in the as-forged condition indicated marginal increase in size which is manifested by the grain size distribution presented in Fig.6.b. The number fraction of fine grains ( $< 5 \mu\text{m}$ ) tends to decrease from  $\sim 0.7$  in the as-forged condition to  $\sim 0.6$  after solution treatment. The grain size distribution reveals broad range of grain sizes ranging from  $1.8 \mu\text{m}$  to as large as  $75 \mu\text{m}$ . The average grain size of forged and solution treated alloy is found to be about  $7.5 \mu\text{m}$ .

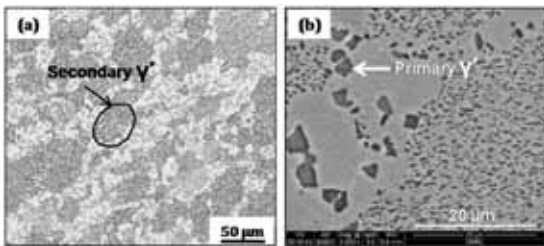


Fig.5. Micrographs of forged + solution treated material (a) optical (b) SEM

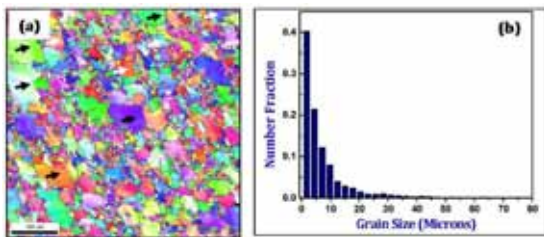


Fig.6. (a) IPF image and (b) grain size distribution of forged + solution treated material

The OIM boundary map and the misorientation angle distribution plot illustrated in Fig.7 indicate significant increase in HAGBs from 35% in as-forged condition to  $\sim 70\%$  owing to the thermal exposure during solution treatment at  $1165^\circ\text{C}$ .

This observation is substantiated by the increase in average misorientation angle ( $\theta_{\text{avg}}$ ) to  $33.1^\circ$  which is almost doubled to that of the as-forged material.

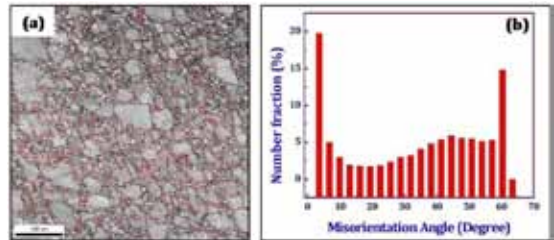


Fig.7. (a) OIM map showing HAGBs (black colour), LAGBs (red colour) in the forged +solution treated material and (b) Misorientation angle distribution

Microstructure of forged + fully heat treated material: The optical micrograph of forged and fully heat treated (i.e. solution treatment + dual-aging) alloy presented in Fig.8.a, reveals homogeneous microstructure with equiaxed grains. The micrograph further reveals the presence of coarse bright primary  $\gamma'$ -precipitates which are uniformly distributed at the grain boundaries (Fig.8.b). In addition, few grains of irregular morphology and very fine precipitates within (circles marked in figures) were seen in the micrographs. The SEM micrograph of heat treated alloy presented in Fig.9 shows the substantial amount of secondary  $\gamma'$  precipitates in the inter-crystalline region. The carbides (bright regions) also seen at the grain boundaries as well at the edges of primary  $\gamma'$  precipitates.

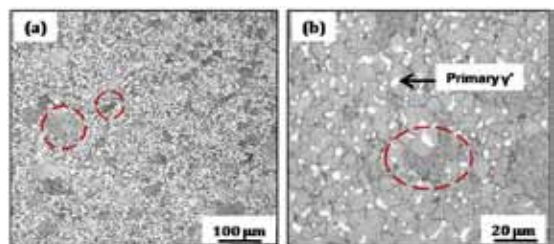


Fig.8. Optical micrographs of forged + fully heat treated material at (a) 100X and (b) 500X magnifications

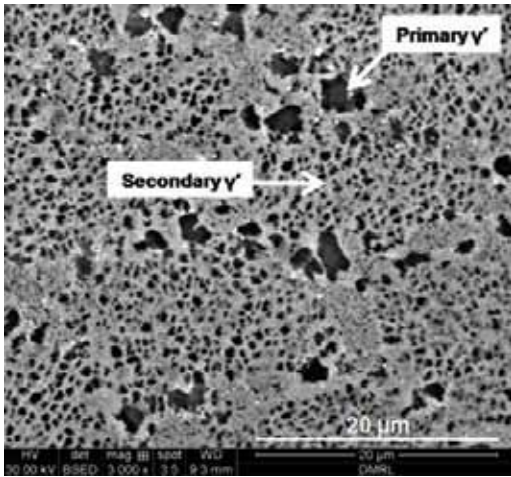


Fig.9. SEM micrograph of forged + fully heat treated material

The IPF colour map observed after forged + solution treated + duplex aging is shown in Fig. 10.a. The microstructure is characterized dominantly by fine equiaxed grains bounded by definite grain boundaries. However, few abnormally coarse grains (indicated by black arrows) are also observed. The grain size distribution (Fig.10.b) is relatively narrowed down wherein the grain sizes are found to be ranging between 2 to 43 μm. This observation indicates the improvement in microstructural homogenization facilitated by the relatively large duplex aging soaking times. The average grain size estimated by linear intercept method is found to ~5 μm, however the number fraction of fine grains (<5 μm) is unaffected during duplex aging. The misorientation angle distribution (Fig.11.a) obtained after heat treatment is characterized by the dominance HAGBs (~0.86) wherein the fraction of LAGBs is estimated at ~0.14. The increase in the fraction of HAGBs is attributed to the recovery and rearrangement of dislocation structures imposed during deformation and subsequent solutionising treatment. The average misorientation angle ( $\theta_{avg}$ ) is increased to 42.2° after fully heat treatment.

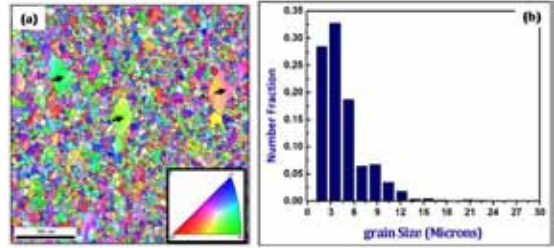


Fig.10. (a) IPF image and (b) grain size distribution of forged + fully heat treated material

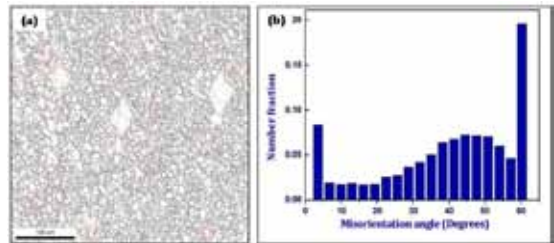


Fig. 11 (a) OIM map showing HAGBs (black colour), LAGBs (red colour) and (b) Misorientation angle distribution in the forged + fully treated material.

The EPMA analysis was carried out on the forged + fully heat treated material. The backscattered electrons (BSE) image obtained by EPMA presented in Fig.12 reveals the presence of bright particles of size range between 1 to 1.5 μm. Elemental mapping carried over these particles/precipitate shows the enrichment of oxygen, hafnium and zirconium. These fine bright-particles are nothing but part of PPB precipitates, disrupted during isothermal forging and distributed randomly in the matrix.

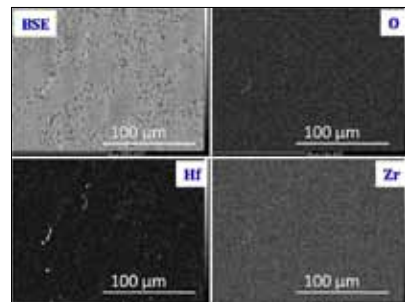


Fig.12. BSE image obtained by EPMA analysis of forged + fully heat treated material

# MICROSTRUCTURAL INVESTIGATIONS ON HOT ISOSTATICALLY PROCESSED PM NICKEL BASE SUPERALLOY

The TEM micrograph of forged and heat treated alloy presented in the Fig.13 shows the presence of primary, secondary and tertiary gamma prime ( $\gamma'$ ) in the material. The coarse primary  $\gamma'$  is present at the grain boundaries and occasionally inside the grains in the form of irregular shape. The secondary  $\gamma'$  of near cubical shape morphology (Fig.13.b) is existing within the grains. The very fine tertiary gamma prime of near spherical morphology is found to be present between secondary  $\gamma'$  precipitates.

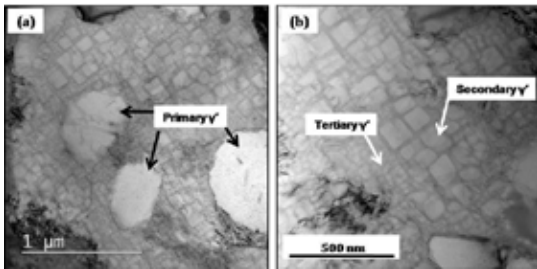


Fig.13. BF-TEM micrograph of the forged + fully heat treated material showing (a) primary  $\gamma'$  and (b) secondary and tertiary  $\gamma'$  in the matrix.

The TEM micrographs presented in Fig.14.a & b reveals that the grain boundaries are mostly decorated with different types of carbide and oxide particles. The SAD patterns confirm that both  $M_{23}C_6$  enriched with Cr having complex-FCC structure (Fig. 14. c) and  $Cr_3C_2$  having orthorhombic structure (Fig.14.d) are present at grain boundaries. On the other hand, fine hafnium oxide particles ( $HfO_2$ ) having monoclinic structure confirmed by SAD pattern (Fig. 14. e) are also present at the grain boundaries.

MC type carbides (Ti-rich) are observed at some places (Fig.15.a) in the forged and heat treated material. Presence of Cr-rich carbide is also observed around the TiC particles (Fig.15.a) and around primary  $\gamma'$  particles (Fig.15.b). The EDS results from the Ti-rich and Cr-rich carbides are shown in Fig.15.c&d respectively. The SAD pattern confirms that they are the TiC and  $Cr_3C_2$  type carbides (Fig.15.e&f).

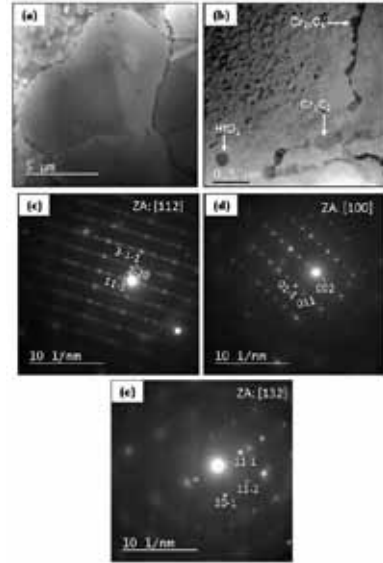


Fig.14. BF-TEM micrograph showing: (a and b) grain boundary carbides (c, d and e) SAD pattern of  $Cr_{23}C_6$ ,  $Cr_3C_2$  type carbides and  $HfO_2$  oxide, respectively.

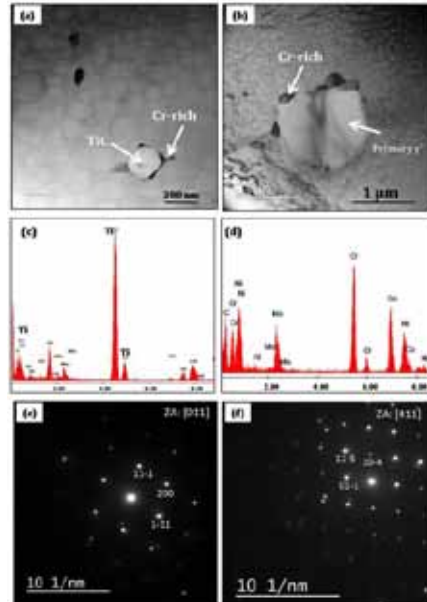


Fig.15. BF-TEM micrographs showing (a and b) Ti- and Cr- rich carbides, (c and d) EDS analyse of Ti- and Cr- rich carbides and (e and f) SAD patterns of TiC and  $Cr_3C_2$  type carbides.

# MICROSTRUCTURAL INVESTIGATIONS ON HOT ISOSTATICALLY PROCESSED PM NICKEL BASE SUPERALLOY

## Discussion

The as - HIPed material has revealed homogeneous microstructure with an average grain size of 12 microns and occasional presence of PPBs [1,2]. It is found that the PPB precipitates are mainly hafnium oxide ( $\text{HfO}_2$ ) and MC-type carbide enriched with Ti. These precipitates have very bad effect on the mechanical properties of the HIPed material, particularly, ductility at high temperature [4]. The size and quantity of PPB precipitates cannot be altered majorly by heat treatment involving sub-solvus solutionising treatment. On the other hand, super-solvus heat treatment can minimise the PPB precipitation, however, grains will be coarsened [5,6]. Therefore, hot working is the better option to disrupt/break the PPB precipitates and improve the mechanical properties of the HIPed material [7-9]. In view of the above, in the present study, the as-HIPed material was subjected to near-isothermal forging with a total deformation of about 50% on original height.

In the as-forged condition the microstructural evolution is characterized by highly deformed structure along with fine equiaxed re-crystallized grains along the grain boundaries as shown in Fig.3. The coarse deformed grains are dominantly bounded by fine dynamically re-crystallized grains along the grain boundaries resembling necklace type of microstructure typically observed in hot deformed materials [7,8]. The presence of deformed structure along with re-crystallized fine grains indicates the occurrence of partial dynamic re-crystallization during near isothermal forging. The observation of necklace type of microstructure substantiates the occurrence of discontinuous dynamic re-crystallization (DDRX). DDRX characterized by distinct nucleation and growth stages is most commonly evidenced during hot working of low to medium stacking fault energy materials. The initiation of DDRX is manifested by serrated/bulged grain boundaries driven by strain

induced grain boundary migration (SIBM). The grain boundary shearing during the initial stages of hot deformation leads to heterogeneous deformation and development of orientation gradient in the vicinity of pre-existing grain boundaries which contributes to grain boundary bulging. The bulged/serrated grain boundaries act as potential DRX nucleation sites.

In order to further understand the DDRX evolution in the deformed structure, magnified IPF colour maps superimposed with HAGBs (black lines) are presented in Fig.16.a. The presence of serrated/bulged grain boundaries indicated by white arrows suggests DDRX as the primary re-crystallization mechanism. Moreover, the observation of large intra-grain misorientation gradient reflected by IPF legend colour gradient within the deformed grains is attributed to the accumulation of deformation substructure and dislocation density. In fact the deformed and the dynamically re-crystallized grains can be differentiated by the misorientation gradient analysis from EBSD data.

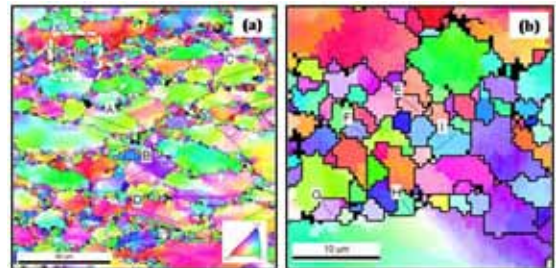


*Fig.16. EBSD analysis of as-forged material: (a) IPF colour map showing coarse deformed grains indicated by A,B, C and D and fine recrystallised grains indicated within square-region (b) Magnified square-region of fine recrystallised region and indicated few grains by E,F,G,H and I.*

The point-origin misorientation gradient across the grain boundaries is quantified for the selected deformed and recrystallised grains highlighted in Fig.16. Meanwhile in case of fine re-crystallized grains (the region highlighted by

## MICROSTRUCTURAL INVESTIGATIONS ON HOT ISOSTATICALLY PROCESSED PM NICKEL BASE SUPERALLOY

red-dotted lines in Fig.16.a) is magnified and misorientation gradient is measured for selected grains as indicated in Fig.16.b. The measured misorientation gradient for re-crystallised fine grains presented in Fig.17.a hardly exceeds  $1^\circ$  clearly indicating the re-crystallized nature of the grains. On the other hand, misorientation gradient for the coarse deformed grains (Fig.17.b) is found to be relatively higher and attains as high as  $22^\circ$  which indicates the highly deformed state of the structure. The presence of large fraction of LAGBs also substantiates the dominant presence of deformed structure and the partial dynamic re-crystallization.

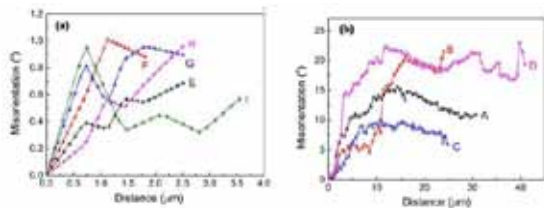


**Fig.17. EBSD analysis of as-forged material: (a) Misorientation across the selected grains within fine recrystallised region (b) Misorientation across the selected coarse deformed grains.**

The microstructural evolution observed after solution treatment at  $1165^\circ\text{C}$  for 4 hours followed by oil quenching is shown in Fig.6.a. The striking difference observed when compared to the microstructure obtained in as-forged condition is the significant increase in HAGBs and marginal coarsening of equiaxed re-crystallized fine grains. The increase in HAGBs is attributed to the rearrangement and annihilation of dislocation sub-structure during solution treatment through static re-crystallization. The observation of static re-crystallization during solution treatment is typically observed in a hot deformed material during subsequent heat treatment. The driving force for the static re-crystallization arises from the deformation stored energy imposed during hot deformation. The occurrence of static re-crystallization eventually results increase in fraction of re-crystallized grains. Meanwhile

the increase in average grain size of the re-crystallized grains is attributed to the higher solution treatment temperature for longer time period of 4h.

It is a well-established fact that as the solution treatment temperature approaches  $\gamma'$  solvus temperature ( $1190^\circ\text{C}$ ) the volume fraction of  $\gamma'$  precipitates tends to decrease. The marginal decrease in harder  $\gamma'$  precipitates tends to retard the pinning effect provided by the precipitates eventually resulting in marginal increase in grain size. However, the pinning effect offered by the precipitates though weakened could be responsible for the prevention of substantial coarsening of coarse grains observed as evident from Fig.6. Moreover the coarse grains observed after solution treatment revealed intra-grain misorientation gradient highlighted by the IPF colour gradient (Fig.6) which suggest the existence of deformation stored energy. The subsequent duplex aging has improved the microstructural homogeneity which is simultaneously reflected by the significant increase in HAGBs and the narrow grain size distribution. The duplex aging process subsequent to the solution treatment is responsible for the complete precipitation of mainly secondary and tertiary  $\gamma'$ -precipitates. The observation of few abnormally large grains in the heat treated condition could be originated from the coarser powder particles present during HIPing. These coarser powder particles may not have subjected to deformation during HIPing and subsequent near isothermal forging. The signature of PPB networks was eliminated completely during 50% deformed material. The PPB precipitates are disrupted to fine size and distributed at the matrix as well as the grain boundaries.

### Conclusions

- The HIPed nickel-base superalloy billet subjected to near isothermal forging (50% deformation) has shown disruption/elimination of PPB networks.

# MICROSTRUCTURAL INVESTIGATIONS ON HOT ISOSTATICALLY PROCESSED PM NICKEL BASE SUPERALLOY

- The HIP+forged and heat treated material has shown irregular shaped primary  $\gamma'$  precipitates located at the grain boundaries. The size and the morphologies of primary  $\gamma'$ -precipitates are unaffected during heat treatment.
- As-forged material has revealed fine dynamically re-crystallized grains along the coarse grain boundaries resembling necklace/duplex type of microstructure. The solution treatment followed by duplexing of as-forged material has resulted fine equiaxed re-crystallized grains of size  $\sim 5\mu\text{m}$  along with few abnormal coarse grains.

## Acknowledgements

The authors would like to thank Defence Research and Development Organization (DRDO) for extending financial support to carry out this study. The authors gratefully acknowledge Dr. Vikas Kumar, Outstanding Scientist and Director, DMRL for his guidance and support for this study. The keenness and immense support of Dr. Samir V. Kamat, Distinguished Scientist and DG (NS&M) for initiating the present study is greatly acknowledged. The authors would like to thank Dr. TK. Nandy, Scientist 'H', Division Head, PMD for his constant encouragement for this work. The active involvement and technical contribution of all members of powder processing group (PPG) in their respective capacities for this work is sincerely acknowledged. The technical support extended by Shri SS. Satheesh Kumar, Dr. Rajdeep Sarkar, Shri Vajinder Singh and D. M. Sudhakara Rao is greatly acknowledged. The members of other groups: NNSG, MEG, SFAG, EMG, MBG, ACG and NDT of DMRL is duly acknowledged.

## References

1. B. Sreenu, B. Suresh Babu, Jalaj Kumar and G. Appa Rao, "Effect of solutionising treatment on the microstructure of HIPed superalloy N18", DRDO-DMRL-PPG-090-2015, April 2015.
2. B. Sreenu, B. Suresh Babu, Rajdeep Sarkar and G. Appa Rao, "Characterisation of P/M HIP processed alloy N18", DRDO-DMRL-PPG-148-2016, December 2016.
3. M.J. Donachie and S.J. Donachie, "Superalloys A Technical Guide", pp. 135-147, (ASM International, 2nd Ed., Materials Park, OH, 2002).
4. G. Appa Rao, M. Srinivas and D. S. Sarma, "Effect of oxygen content of powder on microstructure and mechanical properties of hot isostatically pressed superalloy Inconel 718", *Mater. Sci. Engg. A*, **435**, 84-99, (2006).
5. L. Zhang et al, "Thermal evolution behavior of carbides and  $\gamma'$  precipitates in FGH96 superalloy powder", *Mater. Charact.*, **67**, 52-64, (2012).
6. G. Appa Rao, M. Kumar, M. Srinivas and D. S. Sarma, "Effect of standard heat treatment on the microstructure and mechanical properties of hot isostatically pressed superalloy inconel 718", *Mater. Sci. Engg. A*, **355**, 114-125, (2003).
7. C.T. Sims, N.S. Stoloff and W.C. Hagel: Superalloy-II, *High temperature materials for aerospace and industrial power*, (John Wiley & Sons, 1986).
8. G.H. Gessinger: Powder metallurgy of superalloys, Butterworth & Co publishers (1984)
9. G. Appa Rao and DS. Sarma, "Effect of thermomechanical working on the microstructure and mechanical properties of hot isostatically pressed superalloy Inconel 718", *Mater. Sci. Engg. A*, **383**, 201-212, (2004).

# COATING OF CALCIUM PHOSPHATE CERAMICS OVER DUPLEX STAINLESS STEEL (S2205) AND ITS CHARACTERIZATION

Adhitya K, Kavitha M

Department of Metallurgical Engineering, PSG College of Technology, Coimbatore

**Abstract** - Bio materials are the emerging field in the world of science and innovation. Austenitic stainless steels and titanium alloys are widely used for orthopedic applications. However, a long time exposure leads to dissolution of alloying elements in to the body fluids causing allergic issues. In this work, bioactive HAp is coated over duplex stainless steel for fast recovery of the patient reducing the problem like allergy, ulcer, and pain and cancer cell generation. Parameters like voltage and coating time are varied for coating by maintaining the composition and pH. Coated samples were characterized using scanning electron microscope coupled with spectroscopy. The various morphologies of HAp and TCP crystals were observed and the formation of calcium deficient HAp was confirmed by EDS analysis. It is also observed that, increasing the coating time leads to the formation of thicker coating with poor adherency.

**Keywords** - Electrophoretic deposition, HAP, TCP, Duplex Stainless Steel

## Introduction

Material science engineers are increasingly faced with the need to produce material that should not produce any allergic effect after implanting inside the human body. Ceramics has better corrosion property than metals but they have poor weight to strength ratio (ie, the toughness of the human bone does not match with that of ceramics and also problems that are identified in implanting of metals is that they release metallic ions inside the body leading to several problems after implantation.)

The requirement of materials with combined properties of strength, corrosion resistance, and preferable elongation is growing in a random manner. One of the developed material which combined the properties of ferritic stainless steel and austenitic stainless steel is duplex stainless steel. The most common duplex stainless steel used for various corrosion resistance applications is 2205 duplex stainless steel. Because of its enhanced corrosion resistance, it has replaced various grades of austenitic stainless steel such as 304, 316, and 317 - austenitic stainless steel. But 2205 was not economical like these alloys. This

is due to incorporation of alloy elements like Ni (5.5%) and Mo (3%).

In this coating process, Ca and P are added as separate compounds in the electrolytic solution. During processing period, these compounds dissociates and forms Ca and P ions which will combine and form Ca-P compounds with Ca/P ratio that depends on the parameters like pH of the solution, voltage, concentration of precursors added. Coating is did at pH of 7. The coated samples are characterized under SEM analysis supported with spectroscopy and various morphologies of HAp and TCP crystals are observed obeying various growth modes like Frank-van-der-Marwe mode (TCP coated sample at 7.5 min, and 10V), Stranski-Krastanow mode (HAp coating at 7.5 min, and 10V) and Volmer-Weber mode (HAp coated sample at 10 min, and 7.5V)

## Experiment

The HAp and TCP coatings are electrodeposited over 2205 steel with varying voltage and time. Duplex stainless steel samples are sized and machined for required dimensions. The steel

## COATING OF CALCIUM PHOSPHATE CERAMICS OVER DUPLEX STAINLESS STEEL (S2205) AND ITS CHARACTERIZATION

is degreased, polished with emery sheet (up to 1500) to get rough surface and inhibited in HCl for 30 minutes. After inhibition, samples are cleaned in running water followed by acetone cleaning. The electrolytic solution is prepared for coating TCP and HAp in the composition discussed. For electrolytic solution for coating of TCP 3.16 gram of Tricalciumphosphate + 4 gram of EDTA for a standard solution of 100ml and for electrolytic solution for coating of HAp the electrolyte solution contained 0.6 mM Ca (NO<sub>3</sub>)<sub>2</sub>•4H<sub>2</sub>O (analytical grade) and 0.36 mM NH<sub>4</sub>H<sub>2</sub>PO<sub>4</sub> (analytical grade) with Ca/P ratio being 1.67 in DI water. 0.1 M NaNO<sub>3</sub> was also added in order to improve the conductivity of the electrolyte. Once the solution is prepared, electro deposition unit is set up and the coating is carried out with voltage and time as varying parameters. A Pt plate was used as counter electrode (anode) and duplex stainless steel was used as working electrode. Coating is made with varying voltage and time. HAp is coated at 7.5 volt, 10 volt, 12.5 volt and 15 volt with coating time of 7.5 min, 10 min, 12.5 min, 15 min, 30 min, 60 min, and 120 min. Similarly TCP is coated at 10 volt, 12.5 volt and 15 volt with coating time of 7.5 min, 10 min, 12.5 min, and 15 min. Once the coating is made, to study the adherency of the coating, tape test is made. SEM analysis with EDS is made to study the morphology and composition of the HAp and TCP crystals.



*Fig. 1 Experimental Setup where Pt electrode and SS2205 are immersed in electrolytic solution*

### Results and Discussions

The characterization was made for both base metal and coated samples and the obtained results are discussed below.

#### A. Base Material Characterization:

The microstructure, phase fraction, mechanical properties of the duplex stainless steel was studied before coating the bioactive ceramics. The microstructure reveals homogeneously distributed austenite (Bright phase) in ferrite matrix (Dark phase). Phase fraction analysis was made through Ferritoscope and it is observed that the steel contains 49% ferrite. The mechanical test results shows an ultimate tensile strength of 748.13 MPa, yield strength of 536.70 MPa, with elongation of 37%. The obtained value is higher than the ASTM standard value of UTS 680 MPa (min) and YS 520 MPa (min). The ultimate tensile strength and yield strength of the steel is enhanced due to formation of homogeneous microstructure. The hardness of the produced DSS was found to be 229 BHN. The hardness of the material has met with the standard value of 225 BHN (Min) for the grade 4A. Charpy impact strength of the duplex stainless steel is 170 MPa that agree with the standard values (150 MPa (min)).

#### B. Characterization of the HAP Coated Samples:

##### 1. Visual Observation:

The coating of hydroxyapatite was done in the calcium phosphate electrolyte with pH maintained at 7 and at room temperature. During coating process various visual changes were observed. During trial coating of HAp, the electrolytic solution changed its color from white to yellowish color. This color change indicated some reactions taking place inside the electrolytic solution.

When the coating time was increased to 120 min, the color change was observed again from white

# COATING OF CALCIUM PHOSPHATE CERAMICS OVER DUPLEX STAINLESS STEEL (S2205) AND ITS CHARACTERIZATION

to transparent yellow color indicating that the Ca and P ions present in the solution were reacting and also the coated sample observed has a brownish coating. Where the coating was already completed at some particular time and the coating was removed due to excessive exposure of the material in the electrolytic solution.

In coating of HAP with varying voltage from 10V to 15V, the development of HAP particles over the duplex stainless steel substrate was keenly observed. At 10V the base layer of the coating was formed, with increase in voltage to 12.5V, network like structure with large number of pores was observed. When the voltage is further increased to 15V, the HAP particles started growing over the network and completely covered the network like growth and formed a completely coated layer with very less pores as shown in Fig.2



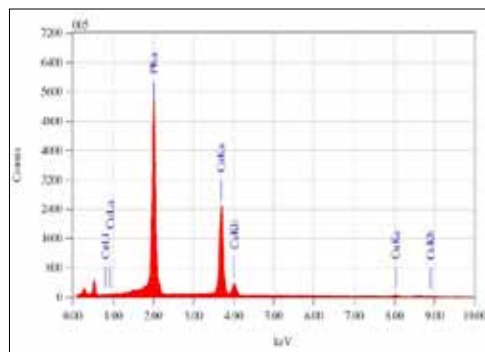
Fig. 2. A) At 10V Formation of base layer over the substrate which is adherent, uniform and homogeneous B) at 12.5V Homogeneous distribution of micro pores with relatively less adherency than A) is observed C) at 15V Uniform coating with less micro pores was formed but with poor adherency.

## 2. Tape test:

Samples coated at 10V with coating time 7.5 minute and 10 minute showed good adhesion than that of the other two coatings.

## 3. EDS Analysis:

The below Graph. 1 indicates the formation of the calcium deficient hydroxyapatite with Ca/P = 0.785.



Graph. 1 EDS Analysis of HAP coated sample

## 4. SEM Analysis:

The first experiment was carried out at the voltage of 10V and coating time ranging from 7.5 Mins to 15 Mins. Current density of the coating was 12.5 mA/cm<sup>2</sup>. The second experiment was carried out at voltage range of 7.5V to 12.5V. The coating time was maintained as 10 Min and the varying current densities of 7.85 mA/cm<sup>2</sup> for 7.5V, 12.5 mA/cm<sup>2</sup> for 10V and 14.58 mA/cm<sup>2</sup> for 12.5V.

The SEM analysis of the coated samples are made and are shown below.

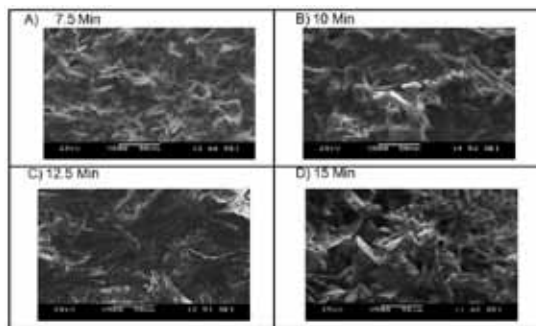


Fig 3. SEM images of electrolytic coated DSS with varying time A) for 7.5 Min, formation of short strings are observed B) for 10 Min, formation of flaky structure was observed with some round particles C) for 12.5 Min, large flakes are formed with a common point as a origin for various flaks D) for 15 Min, broken flake structure is obtained due to exposure of the sample in the electrolytic solution for excessive time.

# COATING OF CALCIUM PHOSPHATE CERAMICS OVER DUPLEX STAINLESS STEEL (S2205) AND ITS CHARACTERIZATION

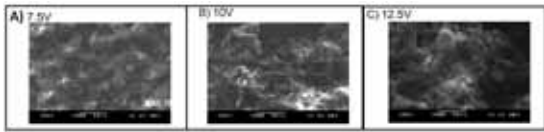
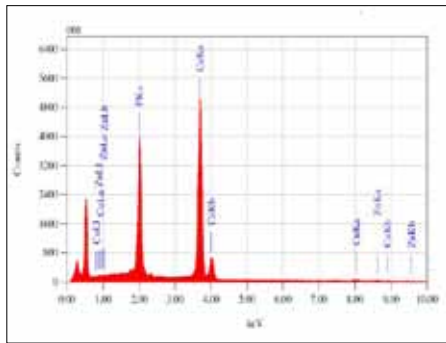


Fig 4. SEM images of electrolytic coated DSS with varying voltage A) for 7.5V, formation of short tubular structures are observed with micro pores B) for 10V, formation of flaky structure was observed with some round particles C) for 12.5V, large tubes are formed.



Graph. 2 EDS Analysis of TCP coated sample

### C. Characterization of the TCP Coated Samples:

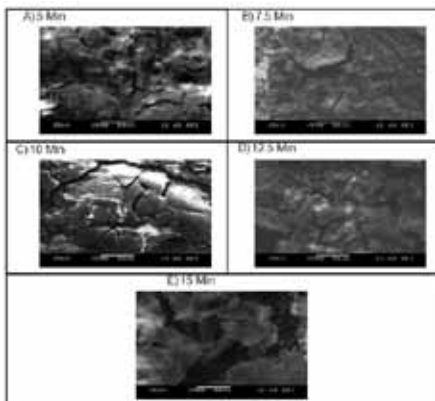


Fig. 5

#### 1. Tape test:

Samples coated at 10V with coating time 10 minute showed good adhesion than that of the other two coatings.

#### 2. EDS Analysis:

Graph.2 shows the result of TCP coated sample with Ca/P ratio of 1.935. Where the Ca/P ratio of TCP which is acceptable.

#### 3. SEM Analysis:

Fig 5. SEM images of electrolytic coated DSS with varying coating time A) for 5 min, formation of short fibrous structures are observed with micro pores B) for 7.5 min, formation of large flaky structure was observed C) for 10 min, rods are formed with some cleavages and also some micro particles of rounded shapes D) Flakes are formed with large pores and cracks formed due to hydrogen evolution E) Rod like structures with flakes at the top are observed resembling celosia structure.

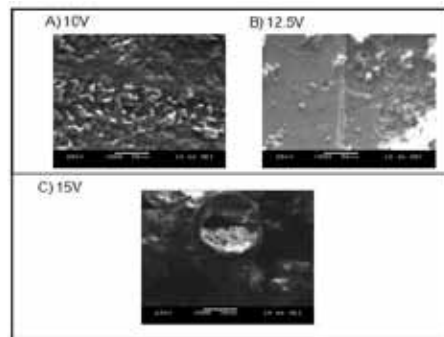


Fig 6. SEM images of electrolytic coated DSS with varying voltage

Coating of TCP was carried out on duplex stainless steel and the results are obtained as follows. The first experiment was carried out at the voltage of 10V and coating time ranging from 5 Mins to 15 Mins. Current density of the coating was 11.47 mA/cm<sup>2</sup>. Fig 6. reveals the SEM images of electrolytic coated DSS with varying voltage where A) shows the coating morphology at 10V, enclosing the formation of short rods like structures are observed with micro cracks B) indicates the coating at 12.5V, revealing the formation of rounded structure was observed but some of the particles started to break down from the surface due to high voltage and C) shows the coating at 15V, revealing large tubes are formed

# COATING OF CALCIUM PHOSPHATE CERAMICS OVER DUPLEX STAINLESS STEEL (S2205) AND ITS CHARACTERIZATION

with some micro particles of rounded and rod shapes are observed.

## Conclusion

HAp and TCP are successfully coated over the produced DSS samples and observed that the coating are very adherent at the following parameters. For HAp coating, 7.5 V and 10 V with 10 min coating time showed good adherency. Whereas for TCP coating, 10 V with 10 min coating time gave good adherency. Growth of HAp and TCP particles over the surface during the coating process was analyzed and reported. Crystallographic growth of calcium phosphates were discussed.

## Acknowledgement

The authors gratefully thank Mr. Barundeeb Raha, DGM, R&D Department, PeeKay Steel Castings (P) Ltd, Aravindh R, B.E. Metallurgical Engineering, Department of Metallurgical Engg, PSGCT (2013 - 2017 Batch) for their support during this work.

## References

- [1] Heejuon Hwang and Yongsoo Park, Effect of Heat Treatment on the Phase Ratio and Corrosion Resistance of Duplex Stainless Steel, *Materials Transactions*, Vol. 50, No. 6, 2009, pp 1548 - 1552.
- [2] Am. Soc. for Testing and Materials, ASTM A781/A781M-91, Standard practice for casting, steel and alloy, common requirements, for general industrial use, ASTM International, 1999.
- [3] Am. Soc. for Testing and Materials, ASTM A890/A890M-91, Standard practice for castings, iron-chromium-nickel-molybdenum corrosion resistant, duplex (austenitic/ferritic) for general application, ASTM International, 1999.
- [4] L. Jianchun, W. Tiyan and R. Yves: \_ Phase Precipitation and Its Effect on the Mechanical Properties of a Super Duplex Stainless Steel, General Metallurgy Department, Faculte Polytechnique de Mons, Mons, Belgium, 1993, pp. 149-156.
- [5] Yakuwa H., Miyasaka M., and Sugiyama K., Evaluation of Crevice Corrosion Resistance of Duplex and Super Duplex Stainless Steels for Seawater Pumps Corrosion, NACE Paper No. 09194, 2009.
- [6] Roscoe C. V. and Gradwell K. J., the History and Development of Duplex Stainless Steels. Duplex Stainless Steel'86, Paper No. 34, 1986.
- [7] Thi Mai Thanh Dinh, Thi Thom Nguyen, Thi Nam Pham and Thu Phuong Nguyen, Electro deposition of HAp coatings on Ti6Al4V alloy and its electrochemical Behaviour in simulated body fluid solution, published on 22 April 2016.
- [8] Nik Norziehana Che Isa\*, Yusairie Mohd and Norjanah Yury, Electrochemical Deposition and Characterization of Hydroxyapatite (HAp) on Titanium Substrate, ICCCP 2012: 5-6 May 2012, Kuala Lumpur, Malaysia.
- [9] Dong-Yang Lin, Xiao-Xiang Wang, Electro deposition of hydroxyapatite coating on CoNiCrMo substrate in dilute solution, accepted in revised form 10 March 2010.
- [10] S. Kannan, A. Balamurugan and S. Rajeswari, Development of calcium phosphate coatings on type 316L SS and their in vitro response, Vol. 16 (1) pp 8-11 (2002).
- [11] Hanan Ali, Shatha Saleem, Thair L. Al-Zubaydi, Evaluation of corrosion behavior of bioceramics coated commercially pure titanium and Ti-6Al-4V alloy, Vol 26 (3), September 2014.
- [12] S.Natarajan,Kousik Polley, Edward Anand,E, Study on Corrosion behavior of 4A and 5A cast duplex stainless steel in different heat treatment conditions, published on, 2015.
- [13] Lin DY, Wang XX. Electro deposition of hydroxyapatite coating on CoNiCrMo substrate in dilute solution. *Surface & Coatings Technology* 2010; 204: 3205-3213.
- [14] Zhao X, Yang L, Zuo Y, Xiong J. Hydroxyapatite coatings on titanium prepared by electro deposition in a modified simulated body fluid. *Chinese Journal of Chemical Engineering* 2009; 17(4): 667-671.
- [15] Zhang Z, Yang Y, Ong JL. Nano-hydroxyapatite for biomedical applications. Taylor & Francis Group, LLC 2006.
- [16] Ducheyne P, Radin S, KingL. The effect of calcium phosphate ceramic composition and structure on in vitro behavior. I. Dissolution. *J Biomed Mater Res* 1993; 27:25-34.
- [17] Morris WF. Hydroxyapatite-coated implants: a case for their use. *J Oral Maxillofac surg* 1998; 56(11) pp. 1303-1311.
- [18] Rudnev V S, Morozova V P, Lukiyanchuk I V and Adigamova M V. Calcium-containing biocompatible oxide-phosphate coatings on titanium. *Russian Journal of Applied Chemistry*. 2010; 83(4):671-679.

# FABRICATION OF BETA Ti<sub>29</sub>Nb<sub>13</sub>Ta<sub>4.6</sub>Zr ALLOY THROUGH POWDER METALLURGY ROUTE FOR BIOMEDICAL APPLICATIONS

Harendra Kumar, Rajamallu K, Rameez R. Tamboli and Suhash R. Dey

Department of Materials Science and Metallurgical Engineering, Indian Institute of Technology, Hyderabad, India

**Abstract** - In this era, Ti-based alloys for e.g. Ti<sub>29</sub>Nb<sub>13</sub>Ta<sub>4.6</sub>Zr (in wt.%) alloy, are the best choice for biomedical applications such as joint fixation and bone replacement because of its high biocompatibility, high strength, and excellent corrosion resistance in the biological environment. In this work, nano-crystallite Ti<sub>29</sub>Nb<sub>13</sub>Ta<sub>4.6</sub>Zr alloy powders are prepared through high energy planetary ball mill at different milling time. The reduction of particle size, crystallite size, and evolution of different phases during the milling process are investigated through scanning electron microscopy (SEM) and X-ray diffraction (XRD). The results indicate that elemental powders of Ti, Nb, Ta, and Zr are fractured and cold welded together during the high energy ball milling. It is observed that nano-crystallite BCC (Ti, Nb, Ta, Zr) phase having the average particle size 6  $\mu\text{m}$  with crystallite size 17 nm, and internal strain of 0.3% for 600 min of ball milling. XRD showed that the complete solid solution is formed for 600 min of milling time. Milled powders are consolidated under uniaxial loading to make a pellet and are sintered in a high vacuum furnace at temperature 1200°C with the heating and cooling rates of 10°C/min & 15°C/min, respectively. The  $\beta$  phase is stabilized in Ti<sub>29</sub>Nb<sub>13</sub>Ta<sub>4.6</sub>Zr for the milling of 30 min, 120 min, and 300 min through high vacuum sintering at 1200°C. The relative density of sintered samples is measured using Archimedes principle and is found nearly 70% of the theoretical density.

**Keywords:** High energy ball milling, Powder metallurgy (P/M), Sintering, X-ray diffraction,  $\beta$  Ti alloys.

## Introduction

Titanium alloys have been developing extensively for medical applications because of their unique combination of excellent biocompatibility, high strength-to-weight ratio, acceptable elastic modulus, high corrosion and wear resistance [1]. The proportion of the aged population is continuously increasing worldwide [2] and the development of suitable biomaterials is inevitable. The commercially available metallic biomaterials in orthopedic implant alloys such as Co-Cr alloys (210-253 GPa) and stainless steels (190-210 GPa) have higher elastic modulus when compared to the human bone elastic modulus (10-30 GPa) [3, 4]. The Ti<sub>6</sub>Al<sub>4</sub>V ( $\alpha + \beta$  alloy) is initially developed for aerospace industry and is later used in orthopedics because of its high strength-to-weight ratio. However, it is found that the alloying elements aluminum (Al) metal

ions are associated with Alzheimer's disease and vanadium (V) is considered to be toxic and carcinogenic to the human body [5,7]. Therefore, the selection of biocompatible elements and preventing from contaminations is a priority for biomedical alloys. Moreover, there remains a problem with the Ti<sub>6</sub>Al<sub>4</sub>V implant; 'stress-shielding effect' at the implant-bone interface that results from the higher elastic modulus of Ti<sub>6</sub>Al<sub>4</sub>V (110 GPa) relative to that of cortical bone (30 GPa) [8]. This leads to osteolysis, thigh pain and compromises the long-term stability of the implants. The  $\alpha$  and  $\alpha + \beta$  Ti alloys show relatively lower elastic modulus than the stainless steel and Co-Cr alloys [9]. However, it is still higher than Young's modulus of human bone. Recently, several  $\beta$  titanium alloys have been developed for orthopedic implants such as Ti<sub>29</sub>Nb<sub>13</sub>Ta<sub>4</sub>Mo (50-80 GPa), Ti<sub>29</sub>Nb<sub>13</sub>Ta<sub>6</sub>Sn (65-70 GPa),

# FABRICATION OF BETA Ti<sub>29</sub>Nb<sub>13</sub>Ta<sub>4.6</sub>Zr ALLOY THROUGH POWDER METALLURGY ROUTE FOR BIOMEDICAL APPLICATIONS

Ti<sub>29</sub>Nb<sub>13</sub>Ta<sub>4.6</sub>Sn (55–78 GPa), Ti<sub>29</sub>Nb<sub>13</sub>Ta<sub>2</sub>Sn (45–48 GPa) [10]. The alloying elements Nb and Ta are said to be beta stabilizers [11] whereas Zr and Sn are generally said to be neutralelements [12]. And it is found that the alloying elements such as Al, V, Cr, Fe, Co, Ni, and Zn etc. are toxic [13, 14] whereas Nb, Ta, Zr, Sn are non-toxic [15,16].

In the above context, the core idea is to develop low modulus biocompatible Ti alloys with adequate mechanical strength. Grain refinement enhances the static and dynamic strength of the alloys [17]. It can be achieved by severe plastic deformation (SPD) such as rolling, ECAP, high-energy ball milling etc. In high-energy ball milling process, due to the high-energy impact during milling can provide alloys with good compositional, microstructure homogeneity, and extension of solid solution effect. Titanium alloy Ti<sub>29</sub>Nb<sub>13</sub>Ta<sub>4.6</sub>Zr is developed by Mitsuo Niinomi et al. [18]. The elastic modulus of this alloy is much lower than that of  $\alpha$  and  $\alpha+\beta$  Ti alloys. Moreover, cytotoxicity of Ti<sub>29</sub>Nb<sub>13</sub>Ta<sub>4.6</sub>Zr is nearly similar to that of pure Ti and lower than that of Ti<sub>6</sub>Al<sub>4</sub>V alloy. The present work aims at the fabrication of Ti<sub>29</sub>Nb<sub>13</sub>Ta<sub>4.6</sub>Zr alloy through high energy ball milling and tries to understand the effects of ball milling on the phase evolution, sintering, microstructure, and consequently their mechanical properties.

## Materials and methods

High purity elemental powders of titanium (Ti), niobium (Nb), tantalum (Ta), and zirconium (Zr) are mixed appropriately as shown in Table 1 to generate the desired composition. All the initial work like weight measurement and compaction are carried out in the Glove box (Mbraun) under high purity Argon (Ar) atmosphere in order to prevent the contamination of the powders. The mechanical alloying is carried out using a high energy planetary ball mill (Fritsch) using high-speed steel vial (250 ml) and balls (15 mm diameter & 10 mm diameter). The powders are loaded into a vial in the toluene (50 ml) medium in order to prevent oxidation, cold welding between

the powders, and sticking of the powders on vial inner surface. The ball to powder ratio is kept 10:1 and is carried out at a rotation rate 300rpm. The milling cycle is set as 30 min on-time and 60 min off-time. Higher off-time is set in order to prevent excessive heating during the milling process. The powders are milled at different intervals such as 30 min, 120 min, 300 min, 360 min, 480 min, and 600 min. Milled powder is further analyzed using XRD for phase evolution during the high energy milling process. Milled powders are compacted at the load of 15 kg/cm<sup>2</sup> using 13 mm diameter die size. Green pellets are sintered at 1200 °C for 2 hours using high vacuum (10<sup>-6</sup>-10<sup>-5</sup> mbar) furnace to prevent contaminations such as oxidation at higher temperature (Vacuum Technique Pvt. Ltd., VSB 96). 10°C /min and 15°C /min are used as heating and cooling rates, respectively. Sintered samples are polished with silicon carbide paper with different grit sizes like 180, 600, 1000, 1200, 1500, and 2000. The XRD measurements are carried out for both milled powders and sintered pellets using Bruker (D discover) XRD with Cu K $\alpha$  radiation ( $\lambda = 0.15405$  nm) operated at 50 kV and 20 mA. The powder morphology and microstructure of sintered pellets are investigated by Field Emission Scanning Electron Microscope (FESEM Zeiss-Gemini, Supra 40).

*Table.1: Elemental wt% and at% in compositional alloy*

Elements	Titanium (Ti)	Niobium (Nb)	Tantalum (Ta)	Zirconium (Zr)
Weight %	53.4	29	13	4.6
Atomic %	72	20.2	4.6	3.2

## Results and Discussion

### Pure elemental powder characterization

The SEM images of elemental pure powders are shown in Fig. 1. It is observed that morphology of the all initial powders are in irregular shapes. The particle size of pure elemental powders is calculated by ImageJ software and found the average particle size of 10  $\mu$ m, 8  $\mu$ m, 5  $\mu$ m, and 9  $\mu$ m for Ti, Nb, Ta, and Zr, respectively. The purity

# FABRICATION OF BETA Ti<sub>29</sub>Nb<sub>13</sub>Ta<sub>4.6</sub>Zr ALLOY THROUGH POWDER METALLURGY ROUTE FOR BIOMEDICAL APPLICATIONS

of elemental powders are analyzed by XRD and is shown in Fig. 2. There are no extra peaks and are matched with standard data of all elemental pure powders.

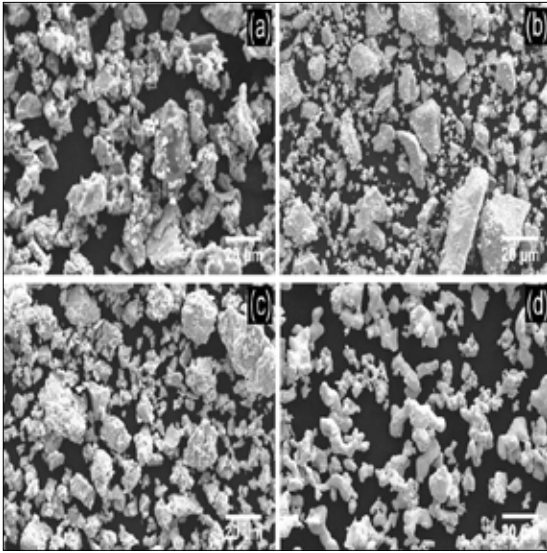


Fig. 1: FESEM images of pure powder (a) Titanium, (b) Niobium, (c) Tantalum, (d) Zirconium

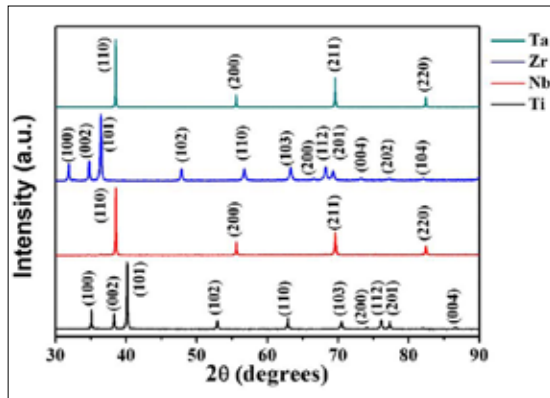


Fig. 2: XRD profiles of pure powder (Ti, Nb, Ta, and Zr)

## Effects of ball milling on Ti<sub>29</sub>Nb<sub>13</sub>Ta<sub>4.6</sub>Zr

The phase change at different milling time during the high energy ball milling are shown in Fig. 3. The figure shows the XRD profiles of

Ti<sub>29</sub>Nb<sub>13</sub>Ta<sub>4.6</sub>Zr powder milled for 30 min, 120 min, 300 min, 480 min, and 600 min. The XRD of 30 min milling show elemental peaks of Ti ( $\alpha$  peaks), Nb ( $\beta$  peaks), Zr ( $\alpha$  peaks), and Ta ( $\beta$  peaks). With increasing milling time, the intensity of  $\alpha$  peaks gradually decreasing whereas the intensity of  $\beta$  peak is continuously increasing. The formation of  $\alpha\beta$  solid solution of Ti (Nb, Ta, Zr) is increased with the increase of milling time. Moreover, low intensity and peak broadening are observed because of crystallite size is continuously reduced during the milling. However, extra peaks are observed (at 43.8 deg. and 44.7 deg.) in the XRD profiles for the milling of 300 min and above. These peaks are undesirable and are identified as contaminations (through erosion) from the vials and balls (represented as (\*) in Fig. 3). The X-ray diffraction of high energy milled powder confirms the formation of solid solution Ti (Nb, Ta, Zr) due to the dissolution of elementals peaks into the  $\beta$  Ti matrix. As can be seen from Fig. 3, the BCC (110) peak shift towards lower angle which can be attributed to either lattice parameter increment (due to solid solution formation) or crystal distortion (due to the difference in atomic sizes of alloying elements). The formation of extensive solid solution through high energy ball milling has been reported by many researchers [19-23].

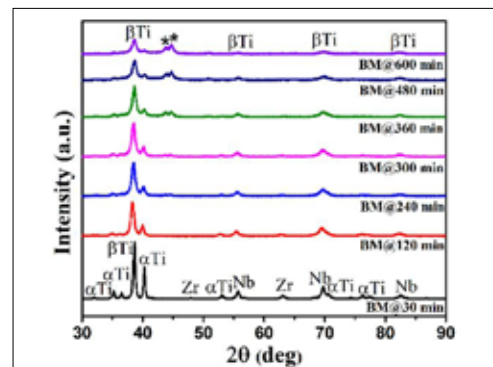


Fig. 3: X-ray diffraction profiles of Ti<sub>29</sub>Nb<sub>13</sub>Ta<sub>4.6</sub>Zr composition for different milling time intervals: 30 min, 120 min, 240 min, 300 min, 360 min, 480 min, and 600 min (\* represents the contaminations from the balls and vials).

## FABRICATION OF BETA Ti29Nb13Ta4.6Zr ALLOY THROUGH POWDER METALLURGY ROUTE FOR BIOMEDICAL APPLICATIONS

Crystallite size is calculated by Williamson-Hall method [24], shown in Fig. 4. Resultant line width ( $B_r$ ) is given by the sum of  $B$  (crystallite) and  $B$  (strain) as below

$$(B_r) = B (\text{crystallite}) + B (\text{strain}).(1)$$

where  $B$  (crystallite) =  $K\lambda / L\cos\theta$  and  $B$  (strain) =  $4\eta\tan\theta$ ; Substituting these values in equation 1 and we get as below

$$B_r \cos\theta - 4\eta\sin\theta + K\lambda/L \quad (2)$$

$$B_r^2 = B^2 - B_i^2 \quad (3)$$

Here  $\lambda$  is the wavelength of X-ray,  $\theta$  is the Bragg angle,  $\eta$  is the strain,  $L$  is the crystallite size,  $K$  is the Scherrer constant ( $K=0.9$ ),  $B_r$  is the resultant full-width half maxima (FWHM),  $B$  is the FWHM of milled powder,  $B_i$  is the instrument broadening (FWHM mixed powder). The crystallite size of BCC (Ti, Nb, Ta, Zr) phase decreases rapidly for 300 min milling time and then a gradual decrement is observed for the milling time of 600 min. The calculated crystallite size is 17 nm for the milling of 600 min. Plastic deformation is the main contributor to the induced micro strain in mechanically alloyed powder, which shown in Fig. 4. The strain increases rapidly at the beginning of milling. The calculated value of strain is 0.3% for 30 min milling and it reaches a maximum value nearly 0.5% for the milling of 120 min. Afterwards, the strain decreases gradually and remain constant at nearly 0.31% for the milling of 480 min and above. Lattice strain can be increased either by increasing volume fraction of grain boundaries or by increasing dislocation density or by the mismatching of atomic sizes of alloying elements. The volume fraction of high grain boundaries is increased because of rapid decrement in grain size till 120 min. Afterwards, the strain relaxation is observed which is associated with the annihilation or rearrangement of generated dislocations. The increase in temperature due to collisions of balls during high energy ball milling may also play an important role in decreasing the induced strain. Similar effects are reported in the literature for different alloy [19].

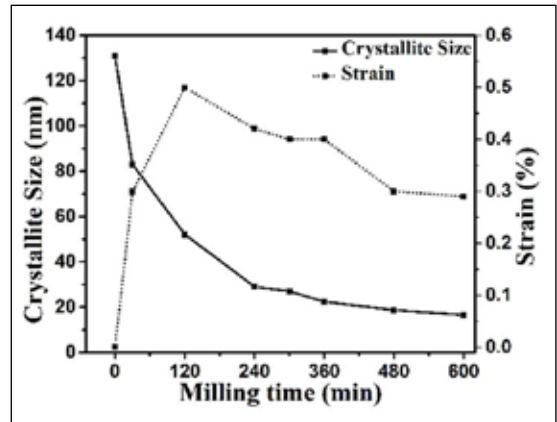


Fig. 4: Calculated crystallite size and internal strain as a function of milling time

It is found that there is not much variation in particle size and shape of pure powders and milled powder. During high energy ball milling, mixed powders are repeatedly cold welded, fractured and rewelded together. The process of cold welding and fracture can be predominant at any stage of milling and depends upon the characteristics of alloying elements. Since the initial powder particles are ductile, there remains a tendency to weld together and form a large particle. The developed particles average size is noticed to be 6  $\mu\text{m}$  at 600 min milling. The rate of cold welding is seen higher than the rate of fracturing. Thus, the ductile particles tend to weld together into large size particles (see Fig. 5).

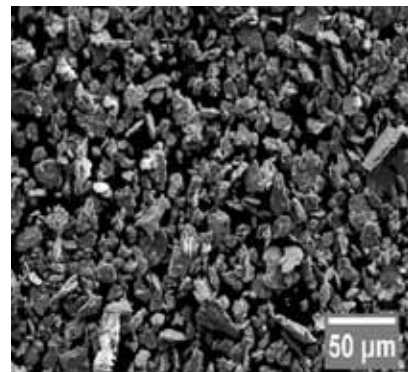


Fig. 5: FESEM image of 600 min milled powder of Ti29Nb13Ta4.6Zr.

# FABRICATION OF BETA Ti<sub>29</sub>Nb<sub>13</sub>Ta<sub>4.6</sub>Zr ALLOY THROUGH POWDER METALLURGY ROUTE FOR BIOMEDICAL APPLICATIONS

## 3.3 Sintering of Ti<sub>29</sub>Nb<sub>13</sub>Ta<sub>4.6</sub>Zr

Sintering is carried out for different time milled powders of Ti<sub>29</sub>Nb<sub>13</sub>Ta<sub>4.6</sub>Zr and is analyzed by X-ray diffraction technique (see Fig. 6). The figure shows XRD profiles of sintered samples at 1200 °C with different milling time intervals such as 30 min, 120 min, and 300 min. It is restricted to a maximum of 300 min milling in order to avoid the contamination of balls and vials for the longer milling time. The XRD of the sintered Ti<sub>29</sub>Nb<sub>13</sub>Ta<sub>4.6</sub>Zr alloy without any ball milling is also included in the figure for comparison purpose. As can be seen from Fig. 6, the  $\beta$  phase is almost stabilized in all sintered Ti<sub>29</sub>Nb<sub>13</sub>Ta<sub>4.6</sub>Zr alloy irrespective of milling time. However, the  $\alpha$  peaks are observed in the sintered samples of without milled and 30 min of milled powder of Ti<sub>29</sub>Nb<sub>13</sub>Ta<sub>4.6</sub>Zr. The  $\alpha''$  peaks are observed at higher milling time such as 120 and 300 min. The volume fraction of  $\beta$  phase is estimated as 95% and the rest of the phase consists of either  $\alpha$  and  $\alpha''$  which depends on the milling time.

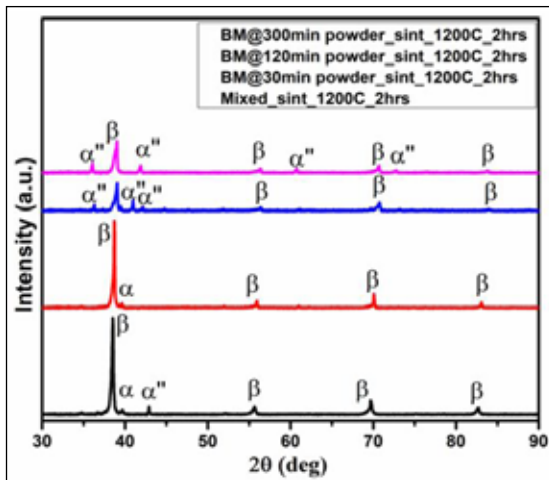


Fig. 6: X-ray analysis of sintered samples at 1200 °C (from lowest: without ball milled, 30 min ball milled, 120 min ball milled, 300 min ball milled).

## 4. Conclusion

The alloy Ti<sub>29</sub>Nb<sub>13</sub>Ta<sub>4.6</sub>Zr is successfully fabricated through the powder metallurgy route using high energy ball milling. The crystallite size

is noticed decreasing continuously and is found to be 17 nm for 600 min milling. The complete  $\beta$  phase is stabilized in the sintered samples of ball milled powder of Ti<sub>29</sub>Nb<sub>13</sub>Ta<sub>4.6</sub>Zr using 1200 °C with 120 min holding time. The alloy Ti<sub>29</sub>Nb<sub>13</sub>Ta<sub>4.6</sub>Zr fabricated through powder metallurgy route can be potentially a good candidate for biomedical applications.

## Acknowledgements

The authors are thankful for the financial support availed from DST-JSPS project (DST/INT/JSPS/P-177/2014).

## References:

- [1] H.J. Rack, J.I. Qazi, Titanium alloys for biomedical applications, Mater. Sci. Eng. C 26 (2006) 1269 - 1277.
- [2] World Health Organization, South-East Asia, Health situation and trend assessment, [http://www.searo.who.int/entity/health\\_situation\\_trends/data/chi/elderly-population/en/](http://www.searo.who.int/entity/health_situation_trends/data/chi/elderly-population/en/)
- [3] M. Geetha, A.K. Singh, R. Asokamani, A.K. Gogia, Ti based biomaterials, the ultimate choice for orthopaedic implants - A review, Prog. Mater. Sci. 54 (2009) 397-425.
- [4] Q. Chen, G. A. Thouas, Metallic implant biomaterials, Mater. Sci. Eng. R 87 (2015) 1-57.
- [5] Silva HM, Schneider SG, Moura Neto, Study of nontoxic aluminum and vanadium-free titanium alloys for biomedical applications, Mater. Sci. Eng. C 24 (2004) 679 - 682.
- [6] Savory J, Ghribi O, Can studies of aluminium toxicity in vivo and in vitro provide relevant information on the pathogenesis and aetiology of Alzheimer's disease?, J. Alzheimer's Disease 11 (2007) 429-430.
- [7] J.L. Domingo, Aluminum and other metals in Alzheimer's disease: a review of potential therapy with chelating agents, J. Alzheimers Dis 10 (2006), 331-341.
- [8] Hallab N J, Vermes C, Messina C, Roebuck K A, Glant T T, Jacobs J J, Concentration- and composition-dependent effects of metal ions on human MG-63 osteoblasts, J. Biomed. Res. 60 (2002) 420-33.

## FABRICATION OF BETA Ti<sub>29</sub>Nb<sub>13</sub>Ta<sub>4.6</sub>Zr ALLOY THROUGH POWDER METALLURGY ROUTE FOR BIOMEDICAL APPLICATIONS

---

- [9] Kuroda D, Niinomi M, Morinaga M, Kato Y, Yashiro T, Design and mechanical properties of new  $\beta$  type titanium alloys for implant materials, *Mater. Sci. Eng. A* 243 (1998) 244-249.
- [10] Long M, Rack HJ, Titanium alloys in total joint replacement, *J. Mater. Sci. Biomater.* 19 (1998) 1621-1639.
- [11] Ikeda M, Komatsu S, Nakamura Y, Effects of Sn and Zr additions on phase constitution and aging behavior of Ti-50 mass%Ta alloys quenched from  $\beta$  single phase region, *Mater. Trans.* 45 (2004) 1106-1102.
- [12] Zhentao Yu, Lian Zhou<sup>2</sup>, Lijuan Luo, Maohong Fan, Yanyan Fu, Investigation on mechanical compatibility matching for biomedical titanium alloys, *Key Eng. Mater.* 288-289 (2005) 595-598.
- [13] Takahashi E, Sakurai T, Watanabe S, Masahashi N, Hanada S, Effect of Heat Treatment and Sn Content on Superelasticity in Biocompatible TiNbSn Alloys, *Mater. Trans.* 43 (2002) 2978-2983.
- [14] Wang K, The use of titanium for medical applications in the USA, *Mater. Sci. Eng. A* 213 (1996) 134-137.
- [15] Niinomi M, Recent research and development in metallic materials for biomedical, dental and healthcare products, *Mater. Sci. Forum* 539-543 (2007) 193-200.
- [16] Wataria F, Yokoyama A, Omorib M, Hiraic T, Kondo H, Uoa M, Kawasakia T, Biocompatibility of materials and development to functionally graded implant for biomedical application. *Compos. Sci. Technol.* 64 (2004) 893-908.
- [17] Akhtar S. Khan, Babak Farrokh, Laszlo Takacs, Effect of grain refinement on mechanical properties of ball-milled bulk aluminum, *Mater. Sci. Eng. A* 489 (2008) 77-84.
- [18] Niinomi M, Fatigue performance and cyto-toxicity of low rigidity titanium alloy, Ti-29Nb-13Ta-4.6Zr, *Biomater.* 24 (2003) 2673-2683.
- [19] Gheisari Kh, Shahriari Sh, Javadpour S, Structural evolution and magnetic properties of nanocrystalline 50 Permalloy powders prepared by mechanical alloying, *J. Alloys Compd.* 574 (2013) 71-82.
- [20] Yanping S, Huey Hoon H, Joo Tien O, Synthesis and characterization of high-energy ball milled Ni-15%Fe-5%Mo, *J. Alloys Compd.* 379 (2004) 266-271.
- [21] Suryanarayana C, Guo-Hao Chen, Abdulbaset F, Froes FH, Structural evolution of mechanically alloyed Ti-Al alloys, *Mater. Sci. Eng. A* 158 (1992) 93-101.
- [22] Botcharovaa E, Heilmaiera M, Freudenbergera J, Drewa G, Kudashowb D, Martinb U, Schultz L, Supersaturated solid solution of niobium in copper by mechanical alloying, *J. Alloys Compd.* 351 (2003) 119-125.
- [23] Arzt E, Schultz A, New materials by mechanical alloying techniques, *Mater. Process. Manuf. Sci.* 6(4) (1991) 733-736.
- [24] Klug HP, Alexander LE, X-ray diffraction procedures for polycrystalline and amorphous materials, John Wiley & Sons, New York, 79 (1974) 553.

# A STUDY ON SINTERING CHARACTERISTICS AND ELECTRICAL CONDUCTIVITY OF Yttria STABILIZED ZIRCONIA CERAMICS SYNTHESIZED BY CO-PRECIPIATION ROUTE

Amruta Vairagade, Kaustubh Kambale\*, Umesh Kedar, Sandeep Butee

Department of Metallurgy and Materials Science, College of Engineering Pune (An Autonomous Institute of Government of Maharashtra), Wellesley Road, Shivaji Nagar, Pune - 411005

**Abstract** - Yttria stabilized zirconia (YSZ) is a popular solid electrolyte for solid oxide fuel cells (SOFCs). It has been a popular belief that in order to employ YSZ as a solid electrolyte in SOFCs, full densification of YSZ is required. However, a recent study shows that even if a porous YSZ is used as an electrolyte, the output of an SOFC reduces by merely 0.1 V. Taking this fact into the consideration, YSZ ceramics with yttria content varying from 10-30 wt% were synthesized by co-precipitation route and sintered at 1350 °C so as to achieve partial densification of the ceramics. The electrical conductivity of such ceramics was studied using impedance spectroscopy and has been discussed in detail in the paper. YSZ powders were prepared by co-precipitation route using zirconium oxychloride octahydrate and yttria dissolved in water using concentrated nitric acid. Calcination temperature for the dried precipitates was decided using TG/DTA study. The calcination was carried out in the temperature range 750 - 800°C resulting in formation of single phase cubic powder which was confirmed using X-ray diffraction (XRD) study. The calcined powders were cold compacted using polyvinyl alcohol (PVA) as a binder. Pressureless sintering of the pellets was carried out at 1350°C for 4 hours. It was observed that density of the sintered pellets went on decreasing with increasing yttria content. SEM study of the sintered pellets also clearly revealed the presence of porosity in the samples. Electrical conductivity of the pellets was measured in the temperature range of 100 - 800°C at an interval of 20°C in the frequency range of 1 Hz to 1 MHz. The dc conductivity of the pellets was found out from the Jonscher plots. It was observed that total ionic conductivity of the pellets containing 20 and more wt% yttria was significantly lower than those containing lower concentration of yttria. However, it is worth noting that the YSZ ceramics with 10 and 15 wt% yttria still exhibited conductivity of the order of  $1 \times 10^{-3}$  S/cm despite being the porous ceramics. However, in order to use these ceramics for actual SOFC applications would still require evaluation and analysis of the mechanical and thermal properties apart from the knowledge of the desired level of electrical conductivity for a given SOFC.

**Keywords:** Co-precipitation, YSZ, Electrical Conductivity, SOFC

## Introduction

Zirconium dioxide is one of the most studied ceramics.  $ZrO_2$  adopts a monoclinic crystal structure at room temperature and transitions to tetragonal and cubic at higher temperatures. The volume expansion caused by the cubic to tetragonal to monoclinic transformation induces large stresses, and these stresses cause  $ZrO_2$  to crack upon cooling from high temperatures. When the Zirconia is blended with some other oxides,

the tetragonal and/or cubic phases are stabilized. Effective dopants include magnesium oxide (MgO), yttrium oxide ( $Y_2O_3$ , yttria), calcium oxide (CaO), and cerium(III) oxide ( $Ce_2O_3$ ). Zirconium dioxide belongs to refractory, chemically resistant material and has wide application in the commercial production of technical ceramics [1]. The introduction of Solid Oxide Fuel Cells (SOFC) as an alternative electricity and heat generation system is contingent on the

# A STUDY ON SINTERING CHARACTERISTICS AND ELECTRICAL CONDUCTIVITY OF Yttria STABILIZED ZIRCONIA CERAMICS SYNTHESIZED BY CO-PRECIPITATION ROUTE

ability of the fuel cell material to consistently withstand the stresses of normal operating conditions. These include the thermal cycling that a fuel cell may undergo as well as the high temperature and high humidity that is associated with their operation. As with all engineering developments, the availability of appropriate material at the right cost and in the right quantity is an important consideration in developing viable manufacturing processes for delivering end user products. Zirconia based materials are good candidates for SOFC applications due to their ionic conductivity, stability in oxidizing and reducing atmospheres and low cost [1]. Zirconia-Yttria compositions have the ability to meet the necessary structural requirements with the potential of be mass-produced with the required quality. The processing techniques for materials of these compositions are already used to manufacture oxygen ion conducting parts and are well understood [2].

Yttria stabilized zirconia (YSZ) has been a popular choice as an electrolyte in SOFC and research articles available in the literature discuss the various methods of synthesis of YSZ powders via various routes and subsequently sintering these powders by different sintering techniques. Often these articles also correlate the electrical properties of sintered YSZ ceramics to the microstructure obtained as a result of powder processing. However, it has been a commonly observed phenomenon across the literature that the research community across the globe has always strived to obtain fully dense YSZ ceramics in order to use them as an electrolyte in SOFC[3]. However, Suzuki et al. demonstrated that even if a porous YSZ ( $23 \pm 3$  vol% open porosity) is used as an electrolyte in SOFC, the cell generated an open-circuit voltage of about 0.78 V which was only about 0.1 V lower than that observed with dense electrolyte specimens. Even though Suzuki et al. characterized the SOFC characteristics with a great detail, their research article is silent on the electrical characterization of YSZ ceramics incorporated in SOFC. Moreover, the article has

provided a little insight on the microstructural aspects of an electrolyte. However, they claimed that an SOFC designed with a porous electrolyte would open up the opportunities to design thermally and mechanically robust stacks by utilizing hydrocarbon fuels and would also allow the processing of cells at lower temperature using conventional techniques like screen printing since densification of the electrolyte would not be required. Despite being the novel idea, it has not been pursued in the scientific community for about a decade and thus, authors have fabricated porous YSZ ceramics using YSZ powders synthesized by co-precipitation route and studied the electrical properties of the porous YSZ ceramics [4]. Since, it is a well-known phenomenon for YSZ ceramics that with the increase in  $Y_2O_3$  content in  $ZrO_2$ , the porosity of the ceramics increases; the  $Y_2O_3$  content was increased from 10 to 30 mol% and the effect of it was studied on the electrical conductivity of YSZ ceramics. To the best of knowledge of authors, the study presented in this paper regarding the fabrication of porous YSZ ceramics and studying their electrical properties is quite unique and no such study has been reported earlier.

## Experiment

Zirconium oxychloride octahydrate ( $ZrOCl_2 \cdot 8H_2O$ ; Sigma Aldrich) and yttria ( $Y_2O_3$ ; Indian Rare Earths) were used as raw materials for the synthesis of YSZ powders. As discussed earlier the mol% of  $Y_2O_3$  was varied from 10 mol% and 30 mol%. Nomenclature of the compositions is shown in Table 1. Fig. 1 shows the flow chart for the synthesis of YSZ powders by co - precipitation route. In order to decide the calcination temperature of the dried precipitate, simultaneous thermogravimetric analysis - differential thermal analysis was carried out. Fig. 2 shows the TGA curves for the various YSZ precipitates. It can be seen from the Fig. 2 that for each composition change in wt% of the precipitate became constant at around 700°C indicating complete removal of all the residual/volatile species from the precipitate. A sharp

# A STUDY ON SINTERING CHARACTERISTICS AND ELECTRICAL CONDUCTIVITY OF Yttria STABILIZED ZIRCONIA CERAMICS SYNTHESIZED BY CO-PRECIPITATION ROUTE

change in wt% in each of the precipitates around 250°C is attributed to removal of NH<sub>3</sub> gas from the precipitate which was experienced by the authors at these temperatures due to characteristic pungent odor associated with NH<sub>3</sub>. Fig. 3 shows the DTA curves for the YSZ precipitates. It can be seen that for all the compositions DTA signals showed a characteristic hump at around 750°C which indicated the formation of a stable phase in the system. The TGA - DTA study formed the basis for deciding the calcination temperature of the YSZ precipitates which were calcined in a muffle furnace in the temperature range 750 - 800°C for 4 hours.

**Table 1 Nomenclature of YSZ powders synthesized by co - precipitation route**

Mol% Y <sub>2</sub> O <sub>3</sub>	Nomenclature
10	10 YSZ
15	15 YSZ
20	20 YSZ
25	25 YSZ
30	30 YSZ

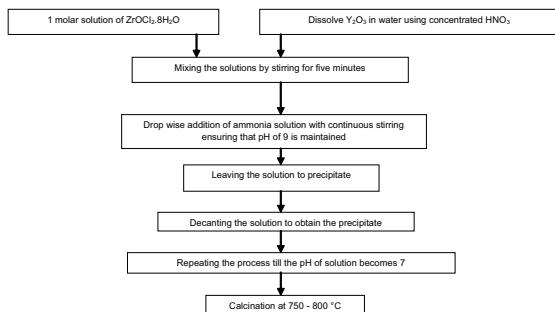


**Fig. 1 Flow chart illustrating the synthesis of YSZ powders by co - precipitation route**

The calcined powder was weighted & mixed with few drops of 3% Poly-Vinyl Alcohol (PVA) in an agate mortar. Then green pellet was formed, with a diameter of 14 mm and about 2 mm thick, by uniaxial die compaction at a pressure of 3tons with dwell time 120secs to ensure relative uniform green density. The pellets were then sintered in

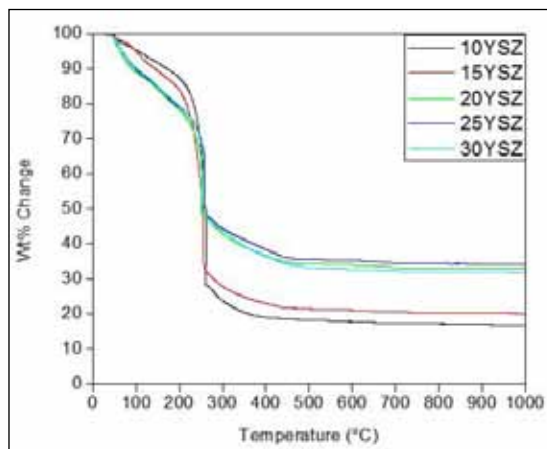


**Fig. 2 TGA curves for YSZ precipitates**

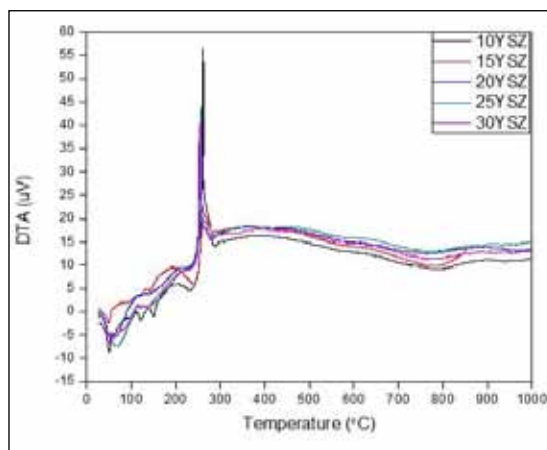


**Fig. 3 DTA curves for YSZ precipitates**

a muffle furnace at temperatures 1250 - 1350 °C for 4 hours. To identify the phase formed in the calcined powder, X- Ray Diffraction was carried out using X-Ray Diffractometer (PANalytical X-Ray Diffractometer) in the 2θ range of 10- 90°. X-ray source was Cu- Kα with the wavelength of 1.54 angstrom. Generator voltage and tube current were 40 kV and 40 mA respectively. Room temperature XRD data was collected with a step size of 0.099 and 176.25 second time per step. X- Ray Diffraction data was also

# A STUDY ON SINTERING CHARACTERISTICS AND ELECTRICAL CONDUCTIVITY OF Yttria STABILIZED ZIRCONIA CERAMICS SYNTHESIZED BY CO-PRECIPITATION ROUTE

collected for sintered pellets to confirm that cubic phase is present in sintered pellets also. The bulk density of the sintered pellets was measured using Archimedes' principle. The microstructure of the sintered pellets was studied using Scanning electron microscopy (SEM: Carl Zeiss, Sigma model) and the local elemental composition was studied using energy dispersive spectroscopy (EDS) attachment with SEM (Bruker detector). The electrical properties of the sintered pellets were studied using impedance spectroscopy (Novocontrol Alpha Dielectric Analyzer) in the frequency range of 1 Hz to 1 MHz and in the temperature range of 100 to 800°C at an interval of 20°C. The samples were electroded using Pt paste before they were they were put in the impedance spectroscopy.

## Results and Discussion

Structural identification was carried out using X - Ray diffraction study. It was observed that for all the YSZ composition calcination in the temperature range 750 - 800°C resulted in the formation of cubic zirconia which was the desired phase from the electrical application point of view. Fig. 4 shows the XRD patterns of 10 YSZ powders calcined in the temperature range of 500 - 750°C for 4 hours. Cubic phase got formed in the powder which was recalined at 750°C. Similar XRD study was carried out on the remaining samples. Table 2 shows the comparison of lattice parameters of synthesized YSZ powders with those of the theoretical lattice parameters. It can be seen that the lattice parameters of the synthesized powders were in good agreement with those of the theoretical lattice parameters. However, it is worth noting that for the compositions 20 - 30 YSZ, there was a lattice mismatch of about 2 -3 % in terms of lattice volume. The theoretical lattice parameters of various YSZ compositions were calculated as per the method devised by Ingel et al., who correlated the lattice parameter of YSZ to the mol%  $Y_2O_3$  in unit cell. Following equation was used to calculate the lattice parameters [5].

$$a = 0.2394 \frac{(0.221+0.018M)}{100+M} \dots \text{Equation 1}$$

Where, M represents mol fraction of  $Y_2O_3$  and lattice parameter is in micro meter.

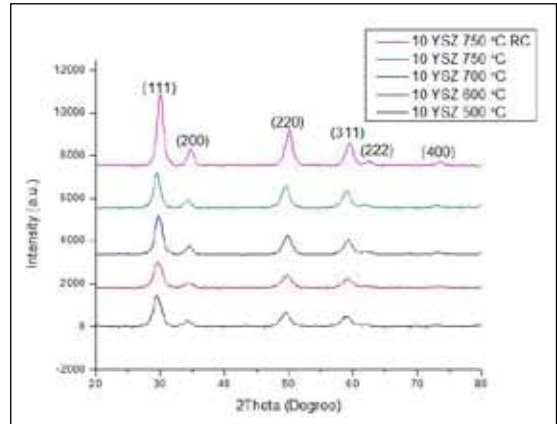


Fig. 4 XRD patterns for 10 YSZ powders calcined at different temperatures

Table 2 Comparison of lattice parameters of calcined YSZ powder with standard values of lattice parameters of YSZ powders

Composition	Standard	Actual	% Change
10YSZ	a = 5.1402 Å	5.1059 Å	0.66
	b = 5.1402 Å	5.1059 Å	0.66
	c = 5.1402 Å	5.1059 Å	0.66
	$\alpha = \beta = \gamma = 90^\circ$	89.364 °	0.70
	V = 135.8126 Å	133.1119 Å	1.98
15YSZ	a = 5.1584 Å	5.1748 Å	0.31
	b = 5.1584 Å	5.1748 Å	0.31
	c = 5.1584 Å	5.1748 Å	0.31
	$\alpha = \beta = \gamma = 90^\circ$	89.798°	0.22
	V = 137.2603 Å	138.5736 Å	0.95
20YSZ	a = 5.1766 Å	5.1290 Å	0.91
	b = 5.1766 Å	5.1290 Å	0.91
	c = 5.1766 Å	5.1290 Å	0.91
	$\alpha = \beta = \gamma = 90^\circ$	89.401 °	0.66
	V = 138.7183Å	134.9267 Å	2.73
25YSZ	a = 5.1947 Å	5.1467 Å	0.92
	b = 5.1947 Å	5.1467 Å	0.92
	c = 5.1947 Å	5.1467 Å	0.92
	$\alpha = \beta = \gamma = 90^\circ$	92.047°	2.27
	V = 140.1785 Å	136.3284 Å	2.74
30YSZ	a = 5.2128 Å	5.1665 Å	0.88
	b = 5.2128 Å	5.1665 Å	0.88
	c = 5.2128 Å	5.1665 Å	0.88
	$\alpha = \beta = \gamma = 90^\circ$	89.567°	0.48
	V = 141.6488 Å	137.9079 Å	2.64

## A STUDY ON SINTERING CHARACTERISTICS AND ELECTRICAL CONDUCTIVITY OF Yttria STABILIZED ZIRCONIA CERAMICS SYNTHESIZED BY CO-PRECIPITATION ROUTE

Relative density of the pellets was measured using Archimedes' principle. In order to calculate the theoretical density of the pellet, following formula devised by Ingel et al. was used.

$$\rho = (818.435 - \frac{137.023M}{100+M}) \left(\frac{1}{a^3}\right) \dots \dots \text{Equation 2}$$

Where, a is a lattice parameter and M is the mole fraction of  $Y_2O_3$ .

Fig. 5 shows the graph of relative density of YSZ ceramics sintered at 1350 °C as a function of  $Y_2O_3$  content. It can be seen that the relative density of the pellets decreased as a function of  $Y_2O_3$  content. Such kind of dependence of relative density on  $Y_2O_3$  would be expected since with increase in  $Y_2O_3$  concentration there is an increase in vacancy concentration owing to difference in the valence states between  $Zr^{4+}$  and  $Y^{3+}$  ions and would cause change in the packing of ions as proposed by Aleksandrov et al [6]. Since, Suzuki et al. had maintained the porosity of the order of  $23 \pm 3$  vol% in the solid electrolytes in their experiment it was attempted to maintain the porosity in the similar range in our experiment as well especially in case of 20, 25 and 30 YSZ ceramics. In order to improve the densification of these ceramics they were sintered at 1350°C for 6 hours which resulted in increase in their relative density to 74.30, 73.61 and 71.27 % respectively bringing them in the comparable densification limit mentioned by Suzuki et al.

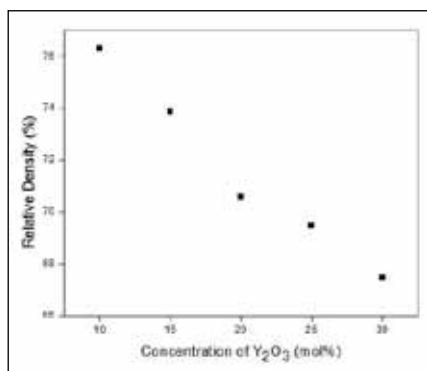


Fig. 5 Relative density of sintered YSZ ceramics as a function of  $Y_2O_3$  concentration

Fig. 6 (a) – (e) shows SEM images of fractured surfaces of YSZ ceramics sintered at 1350°C for 4 hours. Porosity is clearly visible in all the pellets indicating partial sintering of these pellets. In order to study the local elemental composition of sintered YSZ ceramics, energy dispersive spectroscopy was carried out using EDS attachment as mentioned earlier. . A typical energy dispersion spectrum is shown in Fig. 7 depicting the elemental spectrum for 10 YSZ composition. Table 3 shows observed elemental composition of sintered YSZ ceramics. This table also shows the theoretical elemental composition of each ceramic deduced from the formula unit. It can be seen that the theoretical mol percentage and observed mol percentage of different elements of YSZ pellets are nearly same. This can be attributed to co-precipitation method which is most suitable method for obtaining the homogeneity in composition which cannot be obtained by any other method easily.

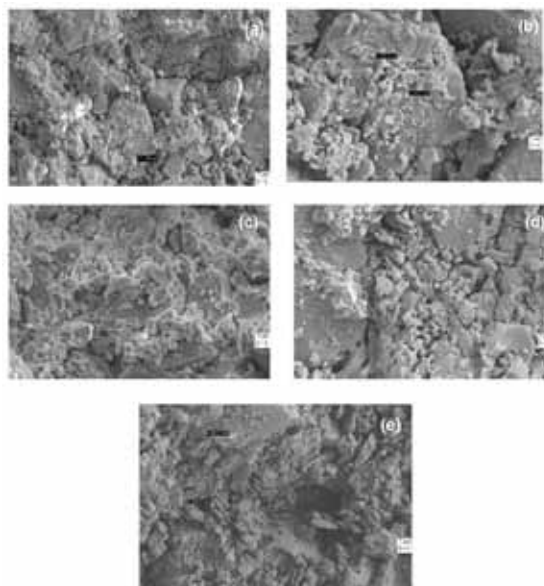


Fig. 6 SEM images of fractured surfaces of (a) 10 YSZ (b) 15 YSZ (c) 20 YSZ (d) 25 YSZ (e) 30 YSZ sintered at 1350 °C for 4 hours

# A STUDY ON SINTERING CHARACTERISTICS AND ELECTRICAL CONDUCTIVITY OF Yttria STABILIZED ZIRCONIA CERAMICS SYNTHESIZED BY CO-PRECIPITATION ROUTE

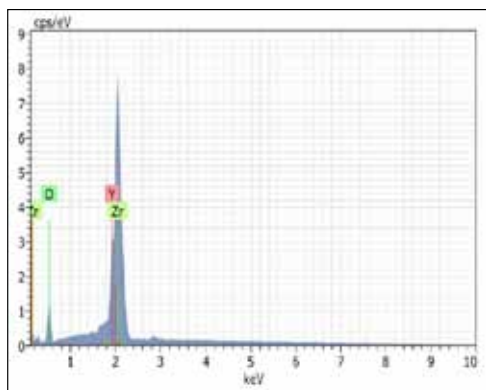


Fig. 7 A typical energy dispersion spectrum for 10 YSZ ceramic

Table 3 Comparison of elemental composition of 10 - 30 YSZ ceramics detected through EDS study

Sr. No.	Composition	Atom%	Element		
			Zr	Y	O
1	10YSZ	Theoretical	28.13	6.25	65.25
		Observed	29.69	6.29	64.02
2	15YSZ	Theoretical	25.75	9.9	65.15
		Observed	26.19	13.28	60.53
3	20YSZ	Theoretical	23.53	11.77	64.70
		Observed	23.83	9.84	66.33
4	25YSZ	Theoretical	21.43	21.43	57.14
		Observed	23.15	15.77	61.07
5	30YSZ	Theoretical	19.49	16.67	63.84
		Observed	18.41	15.55	66.04

The electrical conductivity of sintered YSZ ceramics was obtained by carrying out impedance spectroscopy analysis. Fig. 8 shows the electrical conductivity (ionic conductivity) of 10 YSZ ceramics as a function of temperature at various frequencies. It is very clear that at all frequencies the ionic conductivity increased as a function of temperature which can be attributed to formation of more oxygen vacancies with increase in temperature. In order to use the material as a solid electrolyte it is indeed needed to understand the dc conductivity of it. In order to obtain the dc conductivity of 10 YSZ ceramics, ac electrical conductivity was plotted as a function of frequency at different temperatures. The conductivity was fitted using Jonscher's universal power law given as follows.

$$\sigma = \sigma_0 + A\omega^n \dots \text{Equation 3}$$

Here,  $\sigma_0$  represents the dc electrical conductivity,  $\omega$  represents the angular frequency of the electric field,  $A$  is pre-exponential constant and  $n$  is the power law exponent. In this way, dc electrical conductivity at various temperatures was obtained. A representative curve of electrical conductivity as a function of frequency at 400°C is shown in Fig. 9. It can be seen that up to the frequency of about 103 Hz the electrical conductivity is almost independent of the frequency of the applied electric field which represents the dc part of the conduction whereas beyond the frequency of 103 Hz electrical conductivity increased as a function of frequency due to hopping of ions. Table 4 shows the values of dc conductivity calculated in the manner explained above over a temperature range of 300 - 800 °C.

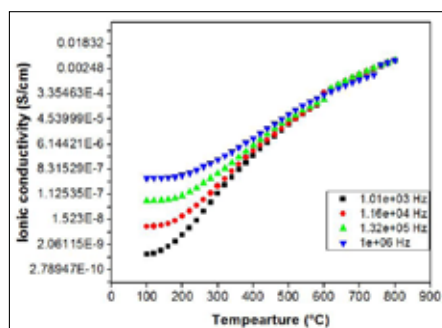


Fig. 8 Electrical (ionic) conductivity of 10 YSZ ceramics as a function of temperature at various frequencies

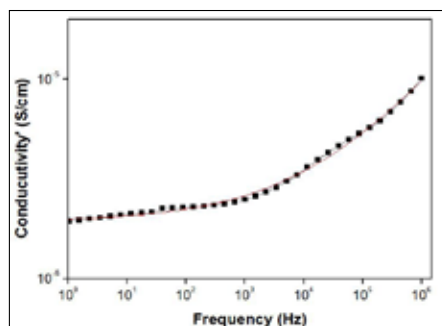


Fig. 9 Electrical (Ionic) Conductivity of 10 YSZ ceramics as a function of frequency fitted using Jonscher's universal power law

# A STUDY ON SINTERING CHARACTERISTICS AND ELECTRICAL CONDUCTIVITY OF Yttria STABILIZED ZIRCONIA CERAMICS SYNTHESIZED BY CO-PRECIPITATION ROUTE

**Table 4 DC conductivity and parameters needed for calculation of activation energy of 10 YSZ ceramics**

Temperature (°C)	Temperature (K)	DC conductivity (S/cm)	$\sigma T$ (Scm <sup>-1</sup> k)	ln ( $\sigma T$ )	1000/T (1/K)
300	573	7.40380E-08	4.24238E-05	-10.067	1.745201
360	623	5.80522E-07	0.000361665	-7.924	1.605136
400	673	1.93425E-06	0.00130175	-6.644	1.485884
460	723	1.01647E-05	0.007349078	-4.913	1.383126
500	773	2.60891E-05	0.020166874	-3.903	1.293661
560	823	7.78733E-05	0.064089726	-2.747	1.215067
600	873	3.10574E-04	0.271131102	-1.305	1.145475
650	923	4.57E-04	0.421811	-0.863	1.083424
700	973	7.13E-04	0.693749	-0.365	1.027749
750	1023	9.17E-04	0.938091	-0.0639	0.977517
800	1073	1.12E-03	1.20176	0.183	0.931966

It can be seen from the above table that various parameters like  $\sigma T$ ,  $\ln(\sigma T)$  and  $1000/T$  have been listed. These parameters were useful in determining the activation energy for conduction in YSZ ceramics by Arrhenius equation as given below.

$$\sigma = (\sigma_0/T) \exp(-E_a/k_b T) \dots\dots \text{Equation 4}$$

Where,  $\sigma$  = Conductivity (S/cm)

T = Temperature (K)

$E_a$  = Activation energy (ev)

$k_b$  = Boltzmann constant

Fig. 10 shows Arrhenius plot for determining the activation energy of conduction of 10 YSZ ceramics. The slope of the plot was calculated using Origin Pro8 software and then using the equation 4, the slope =  $(E_a/0.0862)$ . This calculation yielded the activation energy of 1.26 ev for 10 YSZ ceramics. Similar exercise was repeated for 15 YSZ ceramic resulting in the activation energy of 1.22 eV. However, for the remaining compositions, Arrhenius equation could not be fitted owing to large divergence in dc conductivity values over a range of temperature. This can be attributed to the formation of  $(Y'_{Zr} V_{O'})$  and  $(2Y'_{Zr} V_{O'})_x$  species with increase in  $Y_2O_3$  concentration which act as the trapping centres for oxygen vacancies resulting in a fraction of oxygen species contributing to overall conduction process [5].

Fig. 11 shows the dc conductivity of YSZ ceramics at 800°C, the temperature at which typically SOFCs are operated, as a function of  $Y_2O_3$  concentration. It was observed that 10 and 15 YSZ ceramics exhibited the electrical conductivity values of the order of  $1.2 \times 10^{-3}$  S/cm. However, further increase in  $Y_2O_3$  concentration resulted in decrease in the dc conductivity which again can be attributed to formation of  $(Y'_{Zr} V_{O'})$  and  $(2Y'_{Zr} V_{O'})_x$  [5].

While comparing the electrical conductivity values obtained in this research with the values reported in the literature it was observed that the electrical conductivity values reported even for 10 and 15 YSZ ceramics were lesser than those reported in the literature which can be attributed to lesser extent of densification of YSZ ceramics in this research [7-11]. However, it was also observed that in many research articles found out in the literature the electrical conductivity has been measured over a limited range of temperature, generally less than 500°C and thus, electrical conductivity values could not be compared meaningfully [12-14].

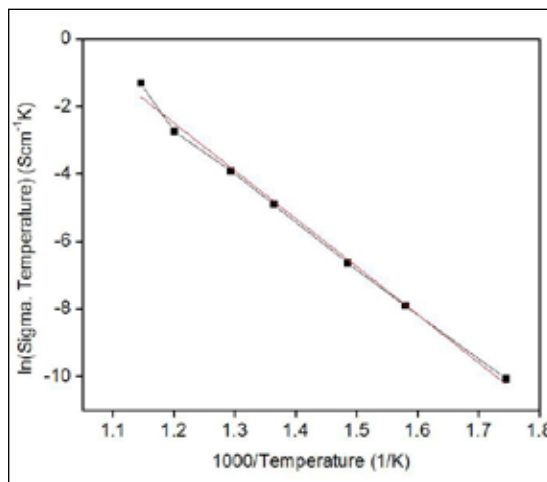


**Fig. 10 Arrhenius plot for determining the activation energy of conduction of 10 YSZ ceramics**

## A STUDY ON SINTERING CHARACTERISTICS AND ELECTRICAL CONDUCTIVITY OF Yttria STABILIZED ZIRCONIA CERAMICS SYNTHESIZED BY CO-PRECIIPITATION ROUTE

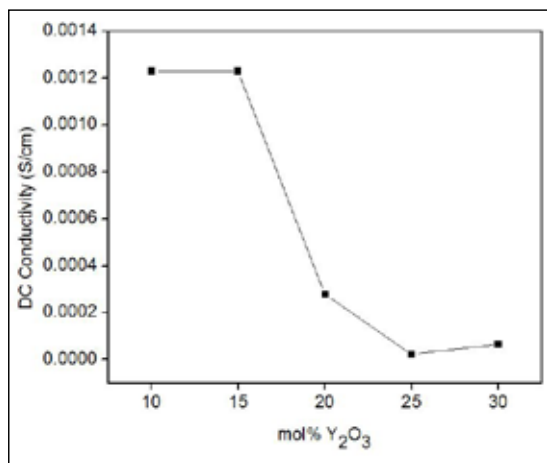


Fig. 11 DC conductivity of YSZ ceramics at 800°C as a function of  $Y_2O_3$  concentration

### Conclusions

This work was inspired by the work of Suzuki et al. reported in the literature wherein they had reported that the open circuit voltage of SOFC employing partially sintered YSZ electrolytes was just 0.1 V lesser than that observed with fully dense electrolytes. Since, the idea of fabricating partially sintered electrolytes has not been well researched, partially sintered YSZ ceramics with mol% of  $Y_2O_3$  varying between 10 to 30 were fabricated and their electrical conductivity was studied. YSZ powders were prepared using co-precipitation route using zirconium oxychloride octahydrate ( $ZrOCl_2 \cdot 8H_2O$ ) and yttria as starting materials. The calcination of the precipitates was carried out in between 750 - 800°C based on extensive TGA and DTA study which resulted in formation of cubic phase in each of the compositions. Since, sintering was carried out at 1350°C for 4 - 6 hours, only 73 - 76% of densification could be achieved which was almost matching the densification level maintained by Suzuki et al. in their work. Scanning electron microscopy confirmed the presence of significant porosity in the sintered ceramics. EDS attachment on SEM was used to detect the local elemental composition of YSZ ceramics which was in good

agreement with the theoretical concentration of each of the elements in YSZ compositions which can be attributed to a good atomic control achievable through co-precipitation route. The dc electrical conductivity of YSZ ceramics was found from impedance spectroscopy data wherein the electrical conductivity was plotted as a function of frequency at different temperatures using Jonscher's universal power law. It was observed that 10 and 15 YSZ ceramics exhibited the electrical conductivity values of the order of  $1.2 \times 10^{-3}$  S/cm. However, further increase in  $Y_2O_3$  concentration resulted in decrease in the dc conductivity which again can be attributed to formation of  $(Y'_{Zr}V_{\delta})$  and  $(2Y'_{Zr}V_{\delta})^{\times}$  concentration which act as the trapping centres for oxygen vacancies resulting in a fraction of oxygen species contributing to overall conduction process. Since, 10 and 15 YSZ ceramics exhibited the conductivity of the order of  $1.2 \times 10^{-3}$  S/cm at 800°C, they still can be considered as ionic conductors with lower than the normal density. It is claimed that an SOFC designed with a porous electrolyte would open up the opportunities to design thermally and mechanically robust stacks by utilizing hydrocarbon fuels and would also allow the processing of cells at lower temperature using conventional techniques like screen printing since densification of the electrolyte would not be required. However, it is required to be understood that whether the sintering techniques like slip casting, extrusion, dry pressing, gel casting etc. which can also be used for fabricating partially sintered ceramics would be useful in making these solid electrolytes. Moreover, the effect of porous structure of solid electrolytes on the thermal, mechanical and more importantly on the overall cell characteristics need to be understood thoroughly before such porous solid electrolytes are put into the application.

### Acknowledgement

Authors acknowledge Prof. A.R. Kulkarni, Department of Metallurgical Engineering and

# A STUDY ON SINTERING CHARACTERISTICS AND ELECTRICAL CONDUCTIVITY OF Yttria STABILIZED ZIRCONIA CERAMICS SYNTHESIZED BY CO-PRECIPITATION ROUTE

Materials Science, Indian Institute of Technology Bombay for providing the impedance spectroscopy facility.

## References:

1. G.R. Karagedov, E.G. Avvakumov; *Low temperature synthesis of ZrO<sub>2</sub>-8 mol.% Y<sub>2</sub>O<sub>3</sub> nanopellet with high sinterability*; Science of Sintering (2010); vol.42; pp.239-245.
2. A.G. Mawson, G.A. Carter, R.D. Hart, N.M. Kirby, A.C. Nachmann; *Mechanical properties of 8 mole% yttria stabilized zirconia for solid oxide fuel cells*; Materials Forum (2006); vol.30.
3. H. G. Scott; *Phase relationships in the zirconia-yttria system*; Journal of Material Science (1975); vol.10; pp.1527-1535.
4. Toshio Suzuki, Piotr Jasinski, Vladimir Petrovsky, Harlan U. Anderson, Fatih Dogan; *Performance of a Porous Electrolyte in Single-Chamber SOFCs*; Journal of The Electrochemical Society (2005), pp.527-531
5. R.P. Ingel, D. Lewis III; *Lattice Parameters and Density for Y2O3- Stabilized ZrO2*; J. Am. Cerarn. Soc. (1986), 69 [4] pp. 325-32.
6. I.V. I. Aleksandrov, V. F. Kitaeva, V. V. Osiko, N. N. Sobolev, V. M. Tatrintsev, and I. L. Chisty, "Dependence of the Properties of a Single Crystal of the Solid Solution ZrO<sub>2</sub>-Y<sub>2</sub>O<sub>3</sub>, on the Y<sub>2</sub>O<sub>3</sub> Concentration," *Kratk. Soobsh. Fiz.*(1975), [3] pp 21-27.
7. Jianghong Gong, Ying Li, Zilong Tang, Yusheng Xie, Zhongtai Zhang; *Temperature-dependence of the lattice conductivity of mixed calcia/yttria-stabilized zirconia*; Materials Chemistry and Physics 76 (2002), pp. 212–216.
8. Fang Zhao, Ying Li, Jianghong Gong, Mingshuai Liu, Yunfa Chen; *Effect of CaF<sub>2</sub> on the electrical properties of yttria-stabilized zirconia*; Materials Letters 58 (2004), pp. 394– 396.
9. Zhengang L, Ruisong Guo, Pei Yao, Fengying Da; *Effects of Al<sub>2</sub>O<sub>3</sub> and/or CaO on properties of yttria stabilized zirconia electrolyte doped with multi-elements*; Materials and Design 28 (2007), pp. 1399–1403.
10. Ya-Zhe Xing, Cheng-Xin Li, Chang-Jiu Li, Hui-Guo Long, Ying-Xin Xie; *Microstructure development of plasma-sprayed yttria-stabilized zirconia and its effect on electrical conductivity*; Solid State Ionics 179 (2008), pp. 1483–1485.
11. Prasanta K. Ojha, S.K. Rath, T.K. Chongdar, A.R. Kulkarni; *Nanocrystalline yttria stabilized zirconia by metal-PVA complexation*; Ceramics International 36 (2010), pp. 561–566.
12. X.J. Chen, K.A. Khor, S.H. Chan, L.G. Yu; *Influence of microstructure on the ionic conductivity of yttria-stabilized zirconia electrolyte*; Materials Science and Engineering (2002); pp. 246–252.
13. Vladimir V. Srdic, Radovan P. Omorjan; *Electrical conductivity of sol-gel derived yttria-stabilized zirconia*; Ceramics International 27 (2001); pp. 859–863.
14. J. Khare, M.P.Joshi, S.Satapathy, H.Srivastava, L.M.Kukreja; *Impedance spectroscopy of pellets made from yttria stabilized zirconia nanoparticles generated via CW and pulsed mode of laser vaporization method*; Ceramics International; Article in Press (DOI:

# LIMITED RESOURCES AT UNLIMITED CAPABILITIES -NEW IDEAS, PROCESSES & MATERIALS WILL ALLOW A GOOD AND CAN PROVIDE A BRILLIANT FUTURE-

T. Zoz<sup>1</sup>, H. Zoz<sup>1-3</sup>

<sup>1</sup>Zoz GmbH, D-57482 Wenden, Germany

<sup>2</sup>CIITEC-IPN, Instituto Politecnico Nacional, Mexico City, C.P. 02250 México, D.F

<sup>3</sup>Ritsumeikan University, Kusatsu, Shiga 525-8577, Japan

**Abstract** - Any modern society considers sustainability, saving resources and increasing performance every day and our all future will be ruled by materials as never before. Based on general materials limitation, goal (a) is “making more with less” and since materials consumption contradicts with such limited resources, goal (b) is recycling. Along with the clear understanding, that there is no waste on this planet but material, both induce to advanced materials processing with the utilization of larger surface and finer structures leading to nanostructures. High kinetic processing has been proven as a major route for reducing materials’ grain size in large volume at economic manufacturing and cost capability as well as the “nanostructure-making-equipment”, the Simoloyer® is well-known including technology and key advantages. Zentallium®, the super-light-weight material at half titanium cost approaching pressing and sintering after hot extruded semi-finished material is on the market. Zentallium® represents grain size stabilized aluminum utilizing carbon nanotubes. The globally first public bridge by Zoz/Dyckerhoff high performance cement at high strength, virtually endless durability and enormous CO<sub>2</sub>-emission savings has been set up in Germany in November 2012. Second demonstrator has followed in June 2013 (heritage balustrade at ZCS Siegen - 12 tons) and the first product from the shelf came up early 2015. Other materials manufacturing results are Nanostructured Ferritic Alloys (next gen. ODS, Zoz/GE), Hydrolium®/H2Tank2Go® including vehicles (Zoz ZEV-fleet & H2-OnAir+ - Zoz/HZG/Airbus et al.), advanced Zn-flake coatings (anti-corrosive material, Zoz, RFS) and even battery cathodes (phosphate systems Mn and Fe, ZoLiBat®) as well as a novel processing route of generating high quality rubber from the roots of dandelion plant (Zoz, Fraunhofer & Continental).

**Keywords** - Simoloyer®, High Kinetic Processing, Zentallium®, FuturZement, Hydrogen-storage

## 1 Introduction

Today and for the future, mankind is obliged to think about what will happen if there is not enough material and if there are not enough resources anymore. Therefore the importance of ultimate and utmost complete recycling and recovery does also include wastes of the past as well as the corresponding suitability of any new product before launched in the market.

The only other possibility of generating more (resources) is increasing performance of all processing, application and materials.

Recycling & Performance are the key issues for achieving sustainability.

Looking at materials, advanced performance can be achieved by increasing the materials function that describes the relation of invested material vs. achievable utilization over volume and time. Since the materials function is mostly depending on materials surface, increasing effective surface is the goal to be achieved by decreasing the unit-size/scale.

Nanomaterials are materials which are produced and applied on a small scale and show enhanced and unique properties compared to comparable

**LIMITED RESOURCES AT UNLIMITED CAPABILITIES  
-NEW IDEAS, PROCESSES & MATERIALS WILL ALLOW A GOOD AND CAN PROVIDE  
A BRILLIANT FUTURE-**

---

materials which are not nanosized [1]. They offer lots of opportunities. Nanostructured materials are modified on the atomic scale. This results in a change of the material's surface-near solid state properties [2].

Nanostructured materials provide a grain size <100nm resulting in a large surface of grain boundaries, virtually a large inner surface. Nanostructures can also represent e. g. a micron-scale matrix with nano-scale phases for generating enhanced properties or other combinations.

Nanostructures can be manufactured in large volume at economic level and insofar contribute significantly to the overall goal of "making more with less".

One of the most practicable and insofar economic routes to obtain useful nanostructures is the High Kinetic Processing technique (HKP) performed by Simoloyer®.

**2 High Kinetic Processing in the Simoloyer®**

HKP is a synonym for well known processes Mechanical Alloying (MA), High Energy Milling (HEM) and Reactive Milling (RM) at higher energetic level.

MA has been described by repeated deformation, fracture and cold welding of powder particles by highly energetic collisions of grinding media [3,4]. Such process can allow the synthesis of novel materials with enhanced or even new properties that cannot be synthesized by conventional techniques due to chemical, physical or thermodynamic barriers.

HEM and RM follow the same principle with a focus on creating reactive surfaces and enabling chemical and physical reactions [3,4]. They differ in the target of processing and in energy that is transferred into the material.

Compared to the well-known/conventional "milling" devices, HKP in the Simoloyer® provides a significantly higher kinetic energy impact and energy impact efficiency [3,4].

Simoloyer® is basically representing a high energy horizontal rotary ball mill where the

definition "mill" does not perfectly but nearest meets the proper definition [5].

Milling/grinding is understood as a process to reduce the particle size of solids such as granules or powders. HKP is understood as a process to primarily reduce the grain size of solids e. g. granules or powders. Reduction of particle size at HKP can be a primary goal e. g. for materials with a very high hardness. On the contrary, also a growth in particle size can be the target e. g. manufacturing ductile metal flakes (DMF) from fine powder dust.

The kinetic impact can be described by the maximum relative velocity (MRV) of (grinding) media. HKP in the Simoloyer® today can reach 18 m/s compared to <6m/s in conventional (milling) processes at high (energetic) efficiency >50% compared to <5% [6] at conventional ball-rod- or shaker-milling insofar confirming the simple understanding of kinetic energy equation (Eq. 1).

$$E_2 = \frac{1}{2} mv^2 \quad (1)$$

Since HKP describes a process based on collision rather than of shear and friction interaction of (grinding)media, consequently HKP also allows a process at a low level of contamination caused by the processing (milling) tools. This is also favored by shorter processing times resulting in a higher energetic impact level.

Table 1 compares the Simoloyer with other devices in use for MA, HEM and RM with respect to capacity, impact and provided energy.

*Table 1: Devices in use for MA, HEM and RM [3,4]*

device	Simoloyer®	Shaker Mill	Planetary ball mill	Attritor™	Drum(ball)mill
max. diameter [m]	0.9	0.08	0.2	1	3
max. total volume [l]	900	0.2	8	1,000	20,000
MRV [m/s]	16/18	4-5 (4.2)	5	4.5-5.1	< 5
specific energy [kWh/l]	1.1(-3)	-	-	0.1-(0.75)	0.01-0.03
scaling up	yes	no	no	yes	yes

Simoloyer® is a brand of Zox GmbH, Germany, Attritor™ is a brand of Union Process, USA

**LIMITED RESOURCES AT UNLIMITED CAPABILITIES**  
**-NEW IDEAS, PROCESSES & MATERIALS WILL ALLOW A GOOD AND CAN PROVIDE**  
**A BRILLIANT FUTURE-**

---

### 3 The Simoloyer®

The Simoloyer® is the HKP device, patent-protected and responsible for numerous inventions in materials and processing [7].

Advanced process control is provided by the Maltoz®-control software allowing patented Cycle Operation particularly for ductile materials composites exhibiting critical milling behavior (CMB) countering agglomeration tendency.

Advanced processing is provided by patented air-lock systems including dead-zone free processing, charging and discharging under vacuum/inert gas at elevated as well as undercooled temperature. The Simoloyer® is technically scalable from lab-scale to industrial in batch, semi-continuous and auto-batch operation mode (carrier gas). Processing tools are available in stainless steel/Stellite®, WC-Co and Si<sub>3</sub>N<sub>4</sub>.



*Fig. 1. Simoloyer® CM01-21m laboratory scale with air-lock (a); Simoloyer® CM081m (back) and CM201m in front (b); CM201m-s1, semi-continuous operation mode (c) and Simoloyer® CM100-s2, auto-batch operation mode.*

The Simoloyer® is the commercial device for synthesizing advanced/new materials e.g. far away from thermal equilibrium or at conventional immiscibility of components. By structural design, important materials' properties can be influenced, grain size tremendously reduced and also chemical reactions can be performed under solvent-free clean condition by solid state synthesis and at 100% yield. Up to 900 tonnes p. a. and per unit can be manufactured.

### 4 Applications in Highlights

#### 4.1 Super-light-weight: Zentallium®

Zentallium® is the Al-CNT composite which is lighter than aluminum and as strong as steel. At

a tensile strength of 700MPa, the specific strength is exceeding that from Ti-6-4 at about half of the materials cost and significantly higher than that of stainless steel (Fig. 5).

Basically, the Al 5083 is grain-refined to nanoscale utilizing the Simoloyer® at strictly closed condition and ultimate cycle operation processing. In situ and air-locked, the carbon nanotube (CNT) sponges are dissolved and alloyed into the Al-matrix on nanoscale.



*Fig. 2. Passivation of Zentallium® powder after Simoloyer®-processing and hot extrusion at ZTC*

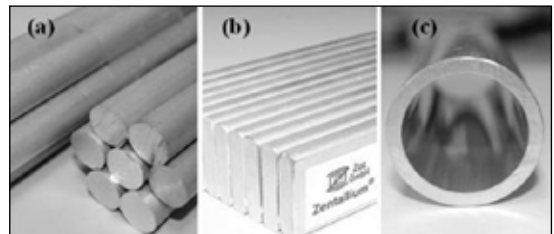


*Fig. 3. Hot-extruded bars D15mm, rods 20/5mm, tube 30x3mm (semi-finished)*

After a passivation step (Fig. 2a) of the highly reactive composite powder, Zentallium® is consolidated by hot extrusion (Fig. 2b) into different semi finished products (Fig. 3a-c). The CNTs during this manufacturing step are hindering the structural re-growth after severe grain-refinement. Zentallium®-powder can also be pressed and sintered, however, so far only hot-extruded semi-finished products bars D15, rods 20/5 (Fig. 3a-b) are available at Zoz from which finished products (Fig. 4b-c) are processed

**LIMITED RESOURCES AT UNLIMITED CAPABILITIES  
-NEW IDEAS, PROCESSES & MATERIALS WILL ALLOW A GOOD AND CAN PROVIDE  
A BRILLIANT FUTURE-**

by common machining at weight-saving rates >60% compared to steel.

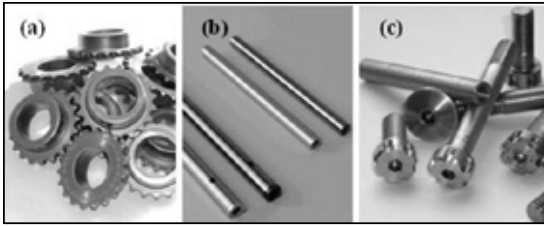


*Fig. 4. Zentallium® finished gear parts (pressed & sintered), helicopter shafts & bicycle screws (made from Zentallium® bars)*

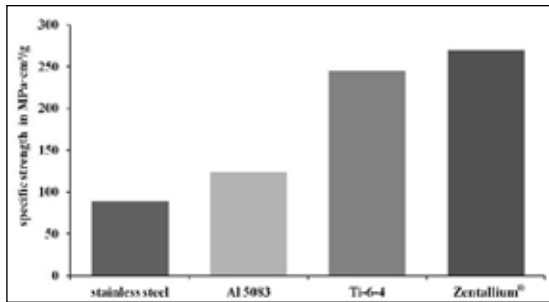


*Fig. 5. Specific strength of stainless steel, Al- and Ti-alloys and Zentallium®*

Zentallium® obtains its high strength according to nano-scale crystallites following the Hall-Petch-relation [8-10]. Zoz received the Materialica Award 2010/Germany for some structural parts by Zentallium®.

**4.2 High Performance Cement/Concrete:  
FuturZement | FuturBeton**

FuturZement and the resulting FuturBeton represent nanostructured cement res. concrete at outstanding performance, economics and environmental friendly impact. FuturBeton is 3-4 times stronger (~140MPa) than ordinary concrete (OPCC) exhibiting very high early strength (~45MPa after 1 day) at superior durability and substantial CO<sub>2</sub>-emission saving (20%). The total absorption costs (TAC, Germany 2012)

based on a single Simoloyer® CM900, leading to about 43,000 tons FuturBeton p. a. is resulting into additional cost of 10 USD per ton of super-concrete.

The Simoloyer® is utilized in a semi-continuous processing mode (Fig. 1c) to super-activate ground granulated blast furnace slag (GGBS). HKP does increase the basically very low hydraulicity of GGBS to a level, where HKP-GGBS can react without any further activators and is replacing 30% of Ordinary Portland Cement (OPC). Due to the continuous processing, the super-activation on nanoscale takes a few seconds at a significantly increased processing kinetic level [11-14].

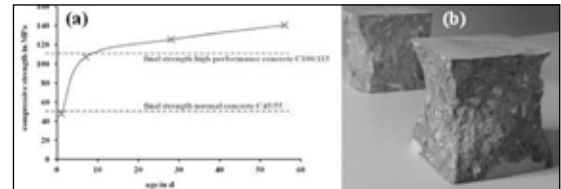


*Fig. 6. Compressive strength of FuturBeton vs. ordinary concrete (OPCC) and high performance concrete (HPC) and “used” ASTM test-cubes (b)*



*Fig. 7. Bridge Rosenthal at Olpe/Germany*

HKP-GGBS is then mixed with 70% OPC at high intensity resulting into FuturZement that is further processed to FuturBeton at practically conventional conditions. The resulting advanced construction material provides a significantly denser packing and fined porosity which means that water / moisture virtually cannot penetrate

## LIMITED RESOURCES AT UNLIMITED CAPABILITIES -NEW IDEAS, PROCESSES & MATERIALS WILL ALLOW A GOOD AND CAN PROVIDE A BRILLIANT FUTURE-

any longer or at least far less resulting in a significant improvement of durability against diffusion of aggressive media that can destroy concrete.

The CO<sub>2</sub> emission saving of 20% is achieved by substitution of clinker/OPC. Additional CO<sub>2</sub>-savings can be claimed due to the high durability and high strength because of less materials consumption and less maintenance or replacing of corroded parts. Thus FuturZement and FuturBeton are highly economic and ecologic.

With FuturBeton, construction-industry can build more faster, sleeker, higher, cost-effective, durable and more environmentally friendly with better surface and less steel.

### 4.3 Energy Storage: H<sub>2</sub> solid state absorber, H<sub>2</sub>Tank2Go®, IronBird, P2G2F®, B4S-SM

H<sub>2</sub>Tank2Go® represents the “click’n-go” Hydrogen-tank cartridge system containing rechargeable nanostructured RT-MH Hydrolium® powder (Fig. 08a) that is developed for a clean, reliable, fast, mass-capable and cost-effective solid state hydrogen storage future utilizing given infrastructures such as vending machines (Fig. 8b), home-depot and home delivery. The H<sub>2</sub>-capacity of 2-4 wt-% of the <1l tanks is >50g operating at <10bar at a lifetime >20years.



Fig. 8. H<sub>2</sub>Tank2Go® loaded with Hydrolium® (dark powder) (a), H<sub>2</sub>Tank2Go® at a tank vending machine (b), IronBird/Stromkoffer in the trunk of a ZEV vehicle (c) and solar-aircraft Icare II (IFB) shall learn to fly on H<sub>2</sub> (d)

The IronBird/Stromkoffer (IronBird is the Airbus definition of the Zoz-Stromkoffer to be translated as power-box) represents the light-weight, cost-effective on-board energy platform carrying 6 H<sub>2</sub>Tank2Go® and 2 small PEMFC (fuel

cells) focusing on both, H<sub>2</sub>-repowering of battery ZEVs in ground transportation (Fig. 8c) as well as range extending the Icare II solar glider (IFB, H<sub>2</sub>-OnAir) in aviation (Fig. 8d).

The systematic of Power-to-Gas-to Fuel (P2G2F®) was nominated for the German Environmental Award 2013 and describes Hydrogen generation from renewable energies, solid state storage, vending-like distribution and consumption in transportation - rethinking mobility for tomorrow's world.



Fig. 9. H<sub>2</sub>-tank system B4S-SM complex metal hydrides (a) and HZG@ZTC (b).

B4S-SM is the world-wide first semi-commercial borohydride solid-state storage tank based on complex metal hydride (LiBH<sub>4</sub> & MgH<sub>2</sub>) and has just been introduced in June 2016 by Zoz and Helmholtz-Centre Geesthacht (HZG) in Germany (Fig. 9). Resulting from the EU-project BOR4STORE [15], the reactive hydride composite material (RHC) is synthesized under extremely closed & clean condition in a Simoloyer® CM100 in auto-batch processing at the HZG-Hydrogen Technology Centre at ZTC in Olpe.

B4S achieves a gravimetric H<sub>2</sub>-density of almost 10 wt-% !! fully reversible in the H<sub>2</sub>-storage powder where the theoretical value is even higher at 18.3 wt-%.

In this respect, novel and advanced in-tank-storage and absorber materials are the objective of the ongoing HySCORE-project [16]. The availability of low cost PEM electrodes is the goal of the ongoing project LOCOPEM [17] and in case of success will be essential for the economics of the IronBird.

### 4.4 Anti-corrosion: Ductile Metal Flakes & ZFP Coating

HKP/Simoloyer® can be utilized for the rapid manufacturing of all kind of ductile metal flakes

## LIMITED RESOURCES AT UNLIMITED CAPABILITIES -NEW IDEAS, PROCESSES & MATERIALS WILL ALLOW A GOOD AND CAN PROVIDE A BRILLIANT FUTURE-

powder [18,19]. Virtually by means of the “HEM-effect” at high kinetic energy impact, processing can be up to 1.000 times faster [20] than in the conventional route (classic ball milling or stamping). By the “MA-effect”, a whole range of alloys can be in situ synthesized e. g. a zinc flake becomes brighter if a small fraction of Al-powder is added into the process.

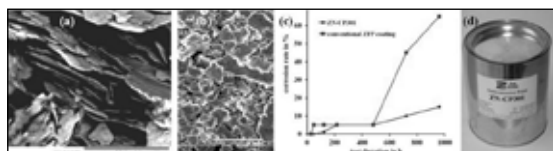


*Fig. 10. HKP-ZFP (Zinc-Flake by Simoloyer®), SEM (a), corresponding Zn-lamellar layer (b) corrosion rate of ZN-CP301 vs. conventional ZFP coating at salt spray test (c) and a product can of anticorrosive paint ZN-CP301 (d).*

Zoz in this field is focusing on ZFP coatings (ZFP = zinc-flake pigments) where the advanced flake manufacturing leads to both, outstanding cost-efficiency and far higher corrosion protection than conventional flake-based products. Since by HKP the flake is processed not in solvents but under dry condition with small fractions of polymer process controlling and dispersing agents, the result is highly flexible and highly economic and also environmentally friendly at a remarkable saving of volatile organic compounds (VOC). Processing times are ranging in minutes rather in hours and days [21] resulting in a high manufacturing capability of up to 1.000 tons p. a. ZFP in a single Simoloyer® CM900 unit.

In order to bringing this HKP-ZFP to the market, appropriate binder systems have been developed for manufacturing ZFP-lacquer systems resulting in the resin based ZN-CP301 anticorrosive coating (Fig. 10d). Figure 10a shows the Zn-flake after rapid manufacturing by HKP/Simoloyer®, Figure 10b a corresponding Zn-lamellar layer and Figure 10c the corrosion rate of ZN-CP301 in comparison to a conventional ZFP coating at outstanding and far superior performance with respect to long term stability in salt spray

according to ISO 7253. E. g. after 950h, the corrosion rate of the ZN-CP301 product is >4 times lower!

After this technical-economic success, the ongoing development of HKP-ZFP to stable water-dispersible pigments is expected to lead to an innovation at highest economical and ecological importance. Previous results are promising and shall break a path to a future with water-based efficient high performance stir-in ZFP-lacquers for industrial, trade and Do-It-Yourself utilization.

### 4.5 ODS/NFA-manufacturing

One of the most exclusive application fields of the Simoloyer® is represented by Oxide Dispersion Strengthened alloys (ODS) and lately also by Nanostructured Ferritic Alloys (NFA) that may be described as a next gen. ODS at further advanced dispersoids by quality, scale, density and by their location in the matrix.

Common ODS alloys (e. g. Plansee PM2000 [22,23]) provide advanced mechanical and/or structural properties such as high tensile and creep strength at elevated temperatures mainly in Al-, Fe- and Ni-based materials in power generation, aerospace and automotive. NFAs, exhibiting a dense dispersion of finer oxides (NFs sub 10nm) are developed for particular demands in nuclear fission and fusion technology such as advanced irradiation damage- and/or corrosion-resistance and high accident tolerance [24].



*Fig. 11. Turbine blade from ODS steel (picture taken from Zoz-ARCI Center, India) and BSE SEM image of 14 YWT [18].*

## LIMITED RESOURCES AT UNLIMITED CAPABILITIES -NEW IDEAS, PROCESSES & MATERIALS WILL ALLOW A GOOD AND CAN PROVIDE A BRILLIANT FUTURE-

The most determining parameters, dispersion and refining are achieved by HKP. The virtually forced solubility of the dispersoid in the metal matrix requires an ultimate high energy transfer into the powder material leading to full dissolution of the starting oxide material creating homogenous network dispersion after consolidation. Same ultimate is a consequent clean handling particularly a clean atmosphere and low contamination during loading, processing and unloading at a full materials yield.

As of the above, the Simoloyer® is practically the globally exclusively applied device / technique. When it comes to semi-industrial or industrial manufacturing, the Simoloyer® represents the only known processing solution where the manufacturing of hundreds of kilos under such conditions has been proven since 2014 [25]. This also included 50 kg of a 14YWT Nanostructured Ferritic Alloy FCRD NFA-1 [26] with an oxide scale of 1-4 nm at defined crystal lattice position with a high dislocation density, a superior irradiation damage resistance and a remarkable thermal stability of the dispersed oxides even after 19.000 hours (792 days) at 1.000°C ending with the summary question/ proposal: “do NFA`s represent the “omega” nuclear structural material ?!” [26].

### 4.6 Extending limited resources: Taraxagum™

Taraxagum™ is a brand of the Continental Tires Germany GmbH representing auto-tires made with natural rubber from dandelion. To date the conventional cultivation of natural rubber is utilizing the rubber tree (*Hevea brasiliensis*) mainly in the so-called “rubber belt” up to 30 degrees north and south of the equator. The continuously increasing demand of rubber processing industries as well as the fact, that newly planted rubber trees only after 7-10 years are bringing up a first return along with a global environmental understanding is challenging to finding alternative sources preferably to grow outside the “rubber belt”.



Fig. 12. Continental-Expo with Taraxagum™ auto-tire at the OZ-16 Nanostructure Symposium at Wenden/Germany (left) and ZTC at Olpe/Germany, location of the rubber extraction facility, plant-photo not allowed.

For Zoz and Zoz- processing technology expertise, the dandelion-rubber as a promising alternative became a goal several years back. Starting with a top-secret cooperation with the Fraunhofer Institute for Molecular Biology and Applied Ecology - IME at Münster/Germany this resulted in the Fraunhofer-IME Dandelion Rubber Extraction Facility under the roof of ZTC at Olpe. The semi-industrial manufacturing unit started processing container-loads in 2016. These Fraunhofer-activities are practically funded by Continental, technical details are confidential.

### 4.7 Energy Storage: Li-Ion-3rd generation cathodes and battery ZoLiBat®

ZoLiBat® is representing advanced cathode material for 3rd gen. Li-Ion batteries and a battery series itself. In this field Zoz is a) equipment supplier (LithiumFerroPhosphate = LFP) and materials co-developer and equipment supplier (LithiumManganesePhosphate = LMP) for the phosphate systems that are doped by HKP on nanoscale. On the anode side so far only preliminary work on a nanostructured Si-matrix is done. The ZoLiBat® as a battery answers the political demand of availability of a domestic high performance state of the art electrochemical energy storage system.



Fig. 13. Pouch-cell ZoLiBat® (LMP) and ZoLiBat®-battery pack (14 cells).

**LIMITED RESOURCES AT UNLIMITED CAPABILITIES  
-NEW IDEAS, PROCESSES & MATERIALS WILL ALLOW A GOOD AND CAN PROVIDE  
A BRILLIANT FUTURE-**



Fig. 14. isigo®1.0-ZLB with 1 and longo®1.0-ZLB for 4 ZoLiBat®-battery packs.



Fig. 15. LMP-cathode material made with Zoz-Simoloyer®, HPL>DOW-Kokam.

The ZoLiBat® cathode material/technology provides a high efficient nanostructured LFP- and LMP-electrode material offering a high structural stability due to the strong P-O-bonding. High C-rates allow fast charging and the nanophosphates result at a low inner resistance  $R_i$  staying low over the entire lifetime, high currents can be achieved. Low toxicity and good thermal and electrical cycle-stability are very important benefits. The absence of cobalt offers a significant cost-advantage at high scaling effects. Scaling is not intended to be done at Zoz, likewise all advanced materials manufactured are basically/originally demonstrators for the advanced HKP technology.

## 5 References

- [1] European Chemicals Agency: <https://echa.europa.eu/>
- [2] Spektrum der Wissenschaft: <http://www.spektrum.de/>
- [3] H. Zoz et al., in *Proceedings of the 3rd International*

*Symposium of the School of Chemical Engineering, University of Mexico City, Mexico City, 1998.*

- [4] H. Zoz, Ph.D. dissertation, Instituto Politécnico Nacional, Centro de Investigación e Innovación Tecnológica, Mexico City, Mexico, 2008.
- [5] H. Zoz, D. Ernst, H. Weiss, M. Magini, C. Powell, C. Suryanarayana, and F.H. Froes, *Mater. Sci. Forum*, vol. 235-238, no. 10, 1996, pp. 59-66.
- [6] H. Zoz, R. Reichardt and H. Ren, in *Proceedings of the 6th annual international conference on Composites engineering (ICCE/6)*; International Community for Composites Engineering and College of Engineering, Orlando, FL, USA, 1999, p. 697.
- [7] Zoz Group, Simoloyer®: <http://www.zoz.de>
- [8] W. F. Smith and J. Hashemi, *Foundations of Materials Science and Engineering*, 4th ed., McGraw-Hill, 2006.
- [9] E.O. Hall, *Proc. Phys. Soc. London*, vol. 64, 1951, pp. 747-753.
- [10] N.J. Petch, *J. Iron Steel Inst. London*, vol. 173, 1953, pp. 25-28.
- [11] H. Zoz, H. U. Benz, G. Schäfer, M. Dannehl, J. Krüll, F. Kaup, H. Ren and R. Reichardt, in: *Proceedings International Symposium on Metastable, Mechanically Alloyed and Nanocrystalline Materials*, Ann Arbor, MI, USA, 2001.
- [12] H. Zoz, H. U. Benz, G. Schäfer, M. Dannehl, J. Krüll, F. Kaup, H. Ren and D. Jaramillo V., *InterCeram: International Ceramic Review*, vol. 50, 2001, pp. 388-395.
- [13] H. Zoz, H. U. Benz, G. Schäfer, M. Dannehl, J. Krüll, F. Kaup, H. Ren and D. Jaramillo V., *InterCeram: International Ceramic Review*, 50, 2001, pp. 470-477.
- [14] Z. H. Zoz, H. U. Benz, G. Schäfer, M. Dannehl, J. Krüll, F. Kaup, H. Ren and D. Jaramillo V., in *Proceedings PM2TEC 2002, 2002 World Congress on Powder Metallurgy & Particulate Materials*, Orlando, FL, USA, 2002.
- [15] BOR4STORE: Fast, reliable and cost effective boron hydride based high capacity solid state hydrogen storage materials, EU-Project, FCH-JU Grant No 303428: <http://bor4store.hzg.de/>
- [16] HySCORE: Efficient  $H_2$ -storage by novel hierarchically porous core-shell structures with embedded light metal hydrides, project funded

**LIMITED RESOURCES AT UNLIMITED CAPABILITIES  
-NEW IDEAS, PROCESSES & MATERIALS WILL ALLOW A GOOD AND CAN PROVIDE  
A BRILLIANT FUTURE-**

---

by the Federal Ministry of Education and Research of Germany, no. 03SF0532D: <https://www.enargus.de/>

- [17] LOCOPEM: Development of low cost gas diffusion electrodes based on CNTs/CNFs for application in PEM fuel cell systems, project funded by the EU within the operational programme "Investing in our Future" from the European Regional Development Fund and the Ministry of Economic Affairs, Energy, Industry, Small and Medium-Sized Enterprises and Craft of North Rhine-Westphalia, no. NW-1w1w006a / EFRE-0800147: <https://www.w-hs.de/>
- [18] H. Zoz et al., *Metal powder report*, vol. 55, no. 10, 2000, pp. 47-48
- [19] H. Zoz, H. Ren, R. Reichardt, H. U. Benz, A. Nadkarni, *Adv. Powder Metall. Part. Mater.*, vol. 1, 1999, pp. 93-107.
- [20] H. Zoz, D. Ernst, R. Reichardt, T. Mizutani, M. Nishida and H. Okouchi, *Mater. Manuf. Process*, vol. 14, no. 6, 1999, pp. 861-874
- [21] H. Zoz, D. Ernst, T. Mizutani and H. Okouchi, *Metall*, vol. 51, no. 10, 1997, pp. 568-572.
- [22] R. L. Klueh, J. Shingledecker, R. W. Swindemann, and D. T. Hoelzer, *J. Nucl. Mater.*, vol. 341, no. 2-3, 2005, pp. 103-114
- [23] Metallwerk Plansee GmbH, *Material Data Sheet ODS-Superalloy PM 2000*, 1993.
- [24] A. Kimura, W. Han, H. Je, Y. Ha, R. Kasada, K. Yabuuchi, A. Möslang, R. Lindau, and J. Hoffmann, in: *Proceedings OZ-16, 9th International | 9th German-Japanese Symposium on Nanostructures*, Olpe-Wenden, Germany, 2016.
- [25] R. DiDomizio, S. Huang, L. Dial, J. Ilavsky and M. Larsen, *Metall. Mater. Trans. A*, vol. 45, no. 12, 2014, pp. 5409-5418.
- [26] G. R. Odette, in *Proceedings 2nd OZ-Workshop*, University of California at Berkeley (UCB), Berkeley, CA, USA, 2015.
- [27] H. Zoz, H. U. Benz, G. Schäfer, M. Dannehl, J. Krüll, F. Kaup, H. Ren, and D. Jaramillo V., in: *Proceedings PM<sup>2</sup>TEC 2002, 2002 World Congress on Powder Metallurgy & Particulate Materials*, Orlando, FL, USA, 2002.